Mathematics & Statistics Theses & Dissertations   Mathematics & Statistics

Spring 2007

Three Methods for Solving the Low Energy Neutron Boltzmann Equation

Tony Charles Slaba
Old Dominion University

Follow this and additional works at: https://digitalcommons.odu.edu/mathstat_etds

Part of the Ordinary Differential Equations and Applied Dynamics Commons

THREE METHODS FOR SOLVING THE LOW ENERGY

NEUTRON BOLTZMANN EQUATION

by

Tony Charles Slaba
B.S. May 2003, Old Dominion University

A Dissertation Submitted to the Faculty of
Old Dominion University in Partial Fulfillment of the
Requirement for the Degree of

DOCTOR OF PHILOSOPHY

COMPUTATOINAL AND APPLIED MATHEMATICS

OLD DOMINION UNIVERSITY
May 2007

Approved by:

John Tweed (Director)

John H. Heinbockel (Member)

Gordon Melrose (Member)

Francis Badavy (Member)

Steve Blattnig (Member)

ABSTRACT

THREE METHODS FOR SOLVING THE LOW ENERGY
NEUTRON BOLTZMANN EQUATION

Tony Charles Slaba
Old Dominion University, 2007
Director: Dr. John Tweed

The solution to the neutron Boltzmann equation is separated into a straight-ahead component dominating at high energies and an isotropic component dominating at low energies. The high-energy solution is calculated using HZETRN-05, and the low-energy isotropic component is modeled by two non-coupled integro-differential equations describing both forward and backward neutron propagation. Three different solution methods are then used to solve the equations. The collocation method employs linear B-splines to transform each equation into a system of ODEs; the resulting system is then solved exactly and evaluated using numerical integration techniques. Wilson's method uses a perturbational approach in which a fundamental solution is obtained by solving a simple ODE, a new source term is generated by the fundamental solution, and the collocation method is then used to solve the remaining equation. The fixed-point series method extends Wilson's method by continuing the perturbational procedure until desired convergence criteria are met. In all three cases, the total neutron flux is found by adding the forward and backward components. Comparisons are made between the three methods in one, two and three layer configurations in various space environments and compared to Monte Carlo data where available.

This thesis is dedicated to my family.

ACKNOWLEDGMENTS

TABLE OF CONTENTS

LIST OF TABLES

LIST OF FIGURES

Figure   Page

Figure   Page

CHAPTER I

INTRODUCTION

Speaking at NASA headquarters in Washington D.C. on January 14, 2004, President Bush announced a new plan to explore space and extend human presence across our solar system [1]. Though the ill effects of ionizing radiation to humans and materials has been well documented over the past century, radiation shielding research will be of the utmost importance if the President's plan is to be realized. Shielding design is an incredibly complex topic, but it begins with an understanding of how radiation interacts with the atomic and nuclear structure of a shielding material. In particular, when solar particles and cosmic rays bombard a material in space, neutrons can be produced via nuclear processes. The secondary neutrons are typically of lower energy than that of the projectile and the production tends to be highly isotropic at the lowest energies [2,3]. This thesis is concerned with the modeling of the isotropic low energy neutron transport.

SUMMARY OF RADIATION RESEARCH PRIOR TO 1949

Between 1911 and 1913 Victor Hess conducted ten balloon experiments in which he concluded the existence of an extremely penetrating radiation entering the earth's atmosphere from outside [4]. Though his conclusions did not receive general acceptance at the time – and World War I would interrupt further research - Hess's

---

The model journal used was Nuclear Instruments and Methods in Physics Research B: Beam Interactions with Materials and Atoms.

"penetrating radiation" would be generally accepted by 1925 and renamed "cosmic rays" by Milikan [4]. Coincidentally, the health hazards of radiation were also becoming an issue of concern at approximately this same time, but for entirely different reasons.

In 1895, the German physicist Wilhelm Roentgen discovered x-rays, and it would be only a few years before they were used extensively in medicine, physics and biology research. Over the next 20 years, x-rays and sources of natural radioactivity like radium, uranium, and polonium were studied and used for everything from advanced medical research to cures for common ailments. As the uses for radioactive materials and radiation grew, so to did the cases of sickness and death due to over exposure. As early as 1925 the Journal of the American Medical Association published articles concluding the ill effects of radioactive materials and radiation exposure on the human body, as well as their seemingly irreversible effects, and by 1929 the American Medical Association condemned the use of x-rays for cosmetic purposes, and removed radium from its list of approved medicines for internal administration [5]. Though radiation exposure guidelines would eventually be created and continually improved, it would be sometime before the health risks of Hess's cosmic rays would be acknowledged as a radiation risk even for the high altitude aircraft of the time.

SPACE RADIATION RESEARCH

In 1949, C.F. Gell suggested at the panel meeting on "Aero Medical Problems of Space Travel" that space radiation might be life threatening. Though previous studies contradicted Gell's assertion, he supported his claims by pointing out that the

earth's geomagnetic field deflects a portion of the cosmic radiation and hence would not be detected in stratospheric flight measurements; it was also suggested that the deflected particles may be of great importance to radiation protection considerations and should therefore be investigated further. Over the next several years, scientists such as Schaefer, Krebs and Tobias would echo Gell's sentiments for increased research into high-altitude radiation exposure [6], and though all of their arguments were lucid and compelling, widespread interest and support in such research would only be obtained indirectly as a result of the political and sociological landscape of the 1950s.

In 1957 the Soviet Union successfully launched two satellites into orbit – Sputnik I, an unmanned lightweight artificial satellite and Sputnik II, a heavier satellite carrying a live dog. The successful launches prompted quick response from the United States as well as heightened paranoia that the Soviets were now able to fire long-range ballistics from Europe to North America. In early 1958, the United States launched the satellite Explorer I carrying a small scientific payload. At the time, the launch was probably considered a success because it showed the United States long-range ballistic capabilities, but its most important assets would turn out to be the discovery of the Van Allen radiation belts and the birth of space exploration [7]. The so-called Van Allen radiation belts were named after the principal investigator on the Explorer I project; they are belts of energetic charged particles in the upper atmosphere held in place by the earth's magnetic field [8].

Now that space exploration had the attention of both the public and the White House, it was inevitable that radiation risk due to galactic cosmic radiation and solar

flares would receive heightened interest. In June 1960 the NASA Office of Life Science Programs held a conference on radiation problems in manned space flight. Though discussions were weighted on solar flare considerations (primarily due to the February 1956 event), attempts were made to establish acceptable radiation risk guidelines for space exploration. In fact, it was J.E. Pickering who suggested that radiation risk should receive the same consideration as other mission risks. The issue of risk analysis would be continually studied and discussed throughout the 1960s, but it was Pickering's initial response that would become the dominant theme in NASA's exposure guidelines [6].

Over the next few years, researchers both inside and outside of NASA continued to study the effects of radiation exposure. Computational technologies had also developed sufficiently to allow numerical simulations in lieu of the more costly experimental studies. The first High-Energy Transport Code (HETC) was presented by Kinney, Coveyou and Zerby in 1962 at the first Symposium on the Protection Against Radiation Hazards in Space, and the code immediately commanded the attention of all disciplines interested in radiation transport. The high demand coupled with the complexity of the Monte Carlo based HETC and the inadequate computational tools of the time prompted NASA to fund its own internal computational transport program at Langley Research Center [6].

Early code development at Langley resulted in the code PROPER-C (1968) for highly specific transport conditions. The code was later extended to a more general realm of applicability by making use of the Bertini nuclear reaction data (1967) as well as high-energy extrapolation resulting in the code PROPER-3C. Though the

Langley code was considerably faster that its predecessor, the computational cost was still enormous even by 1968 standards. Hence, in the early 1970s NASA released funding for a theoretical nuclear physics program. The program yielded new results in multiple scattering theory, a fundamental theory of heavy ion reactions, and the first Langley-developed database for heavy ion cross-sections (cross-sections are discussed in chapter II) [6]. Eventually, as the limitations, extreme complexity and computational cost of Monte Carlo based codes like HETC were realized; the need for deterministic codes became evident. In particular, a series of deterministic codes were developed from 1979 to present day resulting in the current High Charge and Energy Transport Code 2005 (HZETRN-05) [6,9-15].

HZETRN COMPUTER CODE

The deterministic code HZETRN-05 developed by John Wilson et.al. at NASA Langley Research Center solves the Boltzmann transport equation for charged and neutral particles by using the straight-ahead and continuous slowing down approximations; it has the capability to transport up to 59 ions for energies from $.01 MeV$ to $50,000 MeV$, and it can perform the transport in a variety of material configurations. Further, it can also operate under several different environments – galactic cosmic rays (GCR), trapped radiation (TRP) and solar particle events (SPE).

There are many advantages of HZETRN-05, but it is by no means the purpose or place of this thesis to undermine the use and applicability of Monte Carlo methods. In fact, such methods are still used as a benchmark for verification and validation of many other codes; the importance of Monte Carlo methods to radiation transport research cannot be understated. However, the need for deterministic methods to

quickly obtain results to within reasonable accuracy is becoming increasingly important as researchers in biology, medicine, engineering and physics continue to study radiation risk and require fast results in different environments and systems.

The term "reasonable accuracy" is used quite often when comparing simulation and experimental results, and though HZETRN-05 has been verified to be reasonably accurate for heavy ions at high energies, it displays deviations from theory and experiment for light ions at low energies. In particular, the neutron transport portion of HZETRN-05 is well documented for underestimating the neutron flux due to galactic cosmic rays, trapped radiation or solar particle events, regardless of the material. The underestimate is primarily a function of the straight-ahead approximation used in HZETRN-05 stating that all particles – both primary and secondary – propagate in one general direction [16]. Primary particles are those incident on the material and secondary particles are those produced through elastic, reactive or atomic reactions. For example, when galactic cosmic rays bombard a shielding material, it is well known that several new particles are produced as a result of the primary beam [17].

The tendency of HZETRN-05 to underestimate the neutron spectrum is an issue that needs to be addressed for many reasons; this is perhaps most evident when considering dose quantities in the human body. When radiation interacts with the human body, it deposits energy in discrete increments. The amount of energy absorbed per unit mass of tissue is called the absorbed dose and is expressed in units of Gray (Gy). A one gray dose is equivalent to one joule of radiation energy absorbed per kilogram of tissue. Absorbed dose can also be expressed in terms of the unit rad

with $1\,Gy = 100\,rads$. Equal doses of specific types of radiation are not equally harmful though, and in order to account for this, the absorbed dose is often multiplied by a radiation-weighting factor. The resulting quantity accounts for the relative biological effect of the type of radiation being measured and is referred to as the equivalent dose or dose equivalent [18].

It has been observed that the neutron contribution to total dose equivalent can range anywhere from ten to sixty percent. The wide range in contribution depends on shielding, environment and exposure time [19,20]. It is important to note though that under the right set of circumstances, exposure due to neutron radiation can account for over half of the radiation. Hence, underestimation of neutron fluxes can have a dramatic impact on risk determination due to radiation exposure.

OBJECTIVE OF THIS DISSERATION

This thesis is concerned with modeling the isotropic low energy neutron flux. The full Boltzmann equation describing the flux of charged and neutral particles is given in chapter II, and the steady state form is then deduced. Noting the applicability of HZETRN-05 for charged particles and high-energy neutrons, the neutron flux is split into a straight-ahead component dominating at high-energies and an isotropic component dominating at low energies. The isotropic component is then further split into forward and backward propagating components, and the model equations describing them are derived.

Three different but related solution methods for solving the resulting system of equations are introduced, and the physical interpretation of each is discussed. Since the current version of HZETRN-05 is setup for forward transport, a discussion of how

to implement the bi-directional methods into the code is given for multi-layer configurations. The three methods are then compared in terms of efficiency and accuracy, and results are given for various environments and shielding configurations.

CHAPTER II

THEORY

Consider a beam of ionized particles incident on a target material of some

arbitrary depth and configuration as illustrated in fig. 1 below. For future reference,

let β denote the number of distinct atomic species in the target material.
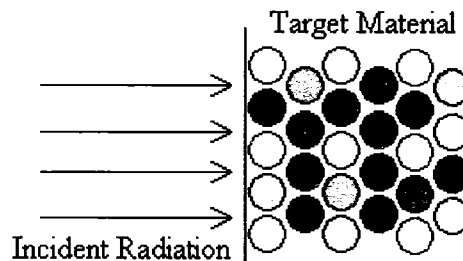
Fig. 1. Radiation incident on target material $(\beta = 6)$.

Select one particle out of the incident beam and suppose it has a kinetic energy E

(MeV) associated with it. As the particle strikes the target face and begins to interact

with the target material, it will transfer some of its energy to the individual atoms in

the material; this energy transfer is the source of radiation damage [17]. Of particular

interest to low-earth orbit and deep-space missions is the radiation damage to humans

and electronic instrumentation exposed to galactic cosmic rays and solar particles

emitted by the sun. In order to quantify such damage at a single point in the material,

one would need an estimate of the number, types, and energies of the particles passing

through the point over some time frame. Such an estimate requires knowledge of

particle transport, and should depend on the characteristics of the incident radiation

and target material.

CROSS-SECTIONS

Consider a single particle of energy E normally incident on a target made up of

a single atomic specie as illustrated in fig 2.
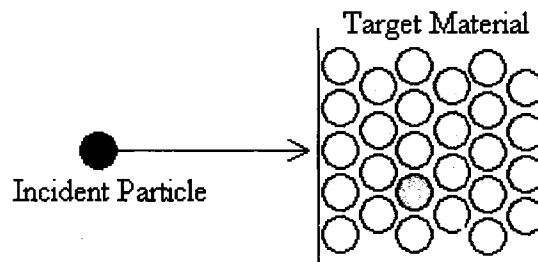
Fig. 2. Single particle incident on target material $(\beta = 1)$.

As stated above, the incident particle will interact with the target atoms and ultimately

transfer or lose some of its energy. Though there are many processes by which this

energy transfer occurs, the three dominant interactions are atomic processes, nuclear

elastic processes, and nuclear reactive processes [6].

Atomic processes are those related to the coulomb interaction experienced by a

positively charged projectile ion while passing near the negatively charged electron

cloud of a target atom as suggested by the fig 3.

Projectile Ion
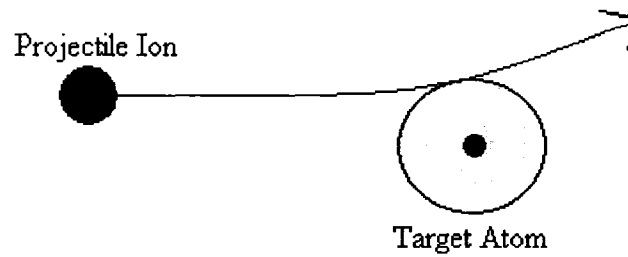
Target Atom

Fig. 3. Atomic interaction.

The charge difference between the projectile ion and electron cloud of the target atom will result in the ionization of the target atom in one of two ways. Either the projectile ion will cause the ejection of a weakly bound electron, or it will excite the target atom by pushing an electron up to a higher energy shell [21]. In either case, the energy of the projectile ion is attenuated by the structure of the target atom. Note that since neutrons carry no charge, they will pass through the electron clouds without significant energy loss, and so atomic interactions do not apply to neutron projectiles.

Nuclear elastic processes are those related to the direct collision between a projectile particle (not necessarily charged) and target atom as depicted in fig. 4; note that neither the projectile nor the target are fragmented in this type of interaction.

Projectile Particle

Target Atom
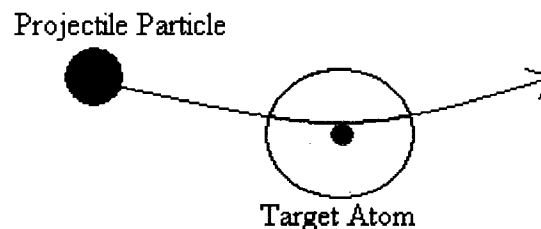
Fig. 4. Nuclear elastic interaction.

Nuclear elastic processes attenuate the energy of the projectile in one of two ways.

The direct collision may cause the projectile to lose energy and leave the target

nucleus unchanged, or it may cause the projectile to transfer some of its energy to the

target nucleus leaving it in an excited state [21].

Nuclear reactive processes are those in which a projectile particle (not

necessarily charged) strikes a target nucleus resulting in projectile and/or target

fragmentation; an example of such a process is given in fig. 5.
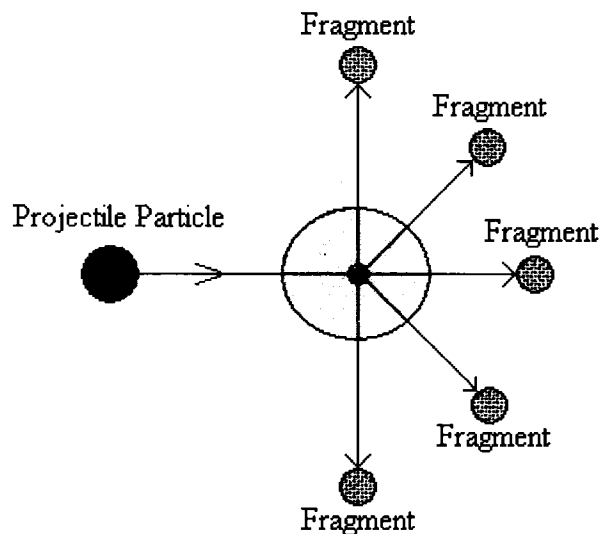
Fig. 5. Nuclear reactive interaction.

Many new types of particles may be produced in this type of process, which typically

involve much greater energy transfers than those described above [21]. It is also

important to note that many atomic collisions $(\sim 10^6)$ occur per cm depth, whereas

fewer $(\sim 10^3)$ nuclear elastic collisions occur per cm depth, and even fewer nuclear

reactive collisions occur $(\sim 10^0)$. Nuclear reactive processes are still important

though, due to the relatively large energy transfers involved and the secondary

particles produced [6].

In order to examine in more detail the likelihood of these processes occurring,

the concept of cross-sections must now be introduced. Consider the more general case

of a stream of type k particles normally incident on a thin plate consisting of a single

atomic specie $(\beta = 1)$. For example, this could correspond to a target material of pure

aluminum (one atomic specie). In reference to fig. 6, let ψ_k be the rate at which the

projectile particles strike the target in units of $[projectiles / cm^2 - sec]$, n_β be the

target particle volume density in units of $[\beta \; type \; atoms / cm^3]$ and Δl be the thickness

of the target in units of $[cm]$.
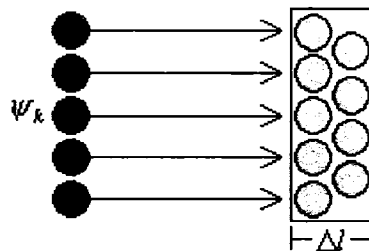
Fig. 6. Homogenous beam normally incident on a thin plate.

The rate, R_β, at which projectile particles interact with the target nuclei must be

directly proportional to both ψ_k and the areal density of target nuclei - $n_\beta \cdot \Delta l$. That is,

$$R_\beta = \left(n_\beta \tilde{\sigma}_\beta\right) \psi_k \, \Delta l \tag{2.1}$$

The constant of proportionality $\tilde{\sigma}_\beta$ is referred to as the microscopic cross-section in

units of $[cm^2]$. If one considers a stream of single point particles incident upon a

particle in the shape of a sphere, $\tilde{\sigma}_\beta$ would simply be the cross-sectional area of the

target particle. In reality, one would need quantum-mechanical laws to fully describe

particle interactions, but it is still useful to think of $\tilde{\sigma}_\beta$ as the effective area that a

target particle presents to the incident beam [22].

For a material consisting of several different atomic species the total rate R at

which projectile particles interact with target atoms will be

$$R = \sum_\beta R_\beta \tag{2.2}$$

where the sum over β is taken to account for the distinct atomic species in the

material. For example, aluminum 2219 – an alloy used in spacecraft construction -

has six atomic species: aluminum, titanium, vanadium, manganese, copper, and

zirconium [23]; therefore, the sum in equation (2.2) would be taken from $\beta = 1$ to

$\beta = 6$. Let n denote the total number of target atoms per unit volume so that

$$n = \sum_\beta n_\beta \tag{2.3}$$

then equation (2.2) can be further expanded and written as

$$R = \sum_\beta R_\beta = \sum_\beta \left(n_\beta \tilde{\sigma}_\beta\right)\psi_k \, \Delta l = \left(n\tilde{\sigma}\right)\psi_k \, \Delta l \tag{2.4}$$

Define the scaled depth $\Delta x = \rho_0 \, \Delta l$, where ρ_0 is the target density in units of

$[g/cm^3]$, and let

$$\rho_\beta = n_\beta / \rho_0 \tag{2.5}$$

be the target particle mass density in units of $[\beta \; type \; atoms / g]$. Then the total mass

density of target atoms in the material is

$$\rho = \sum_{\beta} \rho_{\beta} = \sum_{\beta} \frac{n_{\beta}}{\rho_0} = \frac{n}{\rho_0} \qquad (2.6)$$

The rate at which projectile particles interact with the target can now be expressed as

$$R = \sum_{\beta} R_{\beta} = \sum_{\beta} \left(\rho_{\beta} \tilde{\sigma}_{\beta} \right) \psi_k \, \Delta x = \left(\rho \tilde{\sigma} \right) \psi_k \, \Delta x \qquad (2.7)$$

so that the total macroscopic cross-section can now be defined

$$\sigma = \rho \tilde{\sigma} = \sum_{\beta} \rho_{\beta} \tilde{\sigma}_{\beta} \equiv \sum_{\beta} \sigma_{\beta} \qquad (2.8)$$

in units of $[cm^2 / g]$.

The above formulation did not specify the type of projectile, the projectile energy or the types of processes being considered. In order to make these dependencies explicit, note that the microscopic cross-section can be decomposed according to elastic, reactive and atomic processes as

$$\tilde{\sigma}_{k,\beta}(E) = \tilde{\sigma}^{el}_{k,\beta}(E) + \tilde{\sigma}^{re}_{k,\beta}(E) + \tilde{\sigma}^{at}_{k,\beta}(E) \qquad (2.9)$$

where $\tilde{\sigma}^{el}_{k,\beta}(E), \tilde{\sigma}^{re}_{k,\beta}(E)$ and $\tilde{\sigma}^{at}_{k,\beta}(E)$ are the microscopic elastic, reactive and atomic cross-sections for a type k particle with energy E incident on a type β particle [6]. Equations (2.8) and (2.9) suggest that the total macroscopic cross-section can also be decomposed according to separate processes as

$$\begin{aligned} \sigma_k(E) &= \sigma^{el}_k E) + \sigma^{re}_k(E) + \sigma^{at}_k(E) \\ &= \sum_{\beta} \left[\sigma^{el}_{k,\beta}(E) + \sigma^{re}_{k,\beta}(E) + \sigma^{at}_{k,\beta}(E) \right] \end{aligned} \qquad (2.10)$$

where $\sigma^{el}_{k,\beta}(E), \sigma^{re}_{k,\beta}(E)$ and $\sigma^{at}_{k,\beta}(E)$ are the macroscopic elastic, reactive and atomic cross-sections for a type k particle with energy E incident on a type β particle.

The particle interactions described above will attenuate the projectile energy, and possibly alter the direction of its path. Further, secondary particles may be produced in many directions with energy less than that of the projectile. In order to account for the directional dependence of secondary particle production, a brief discussion of solid angles is necessary.

The solid angle subtended at the center of a sphere of radius r by its surface is 4π steradians (sr). For a small circular surface element of the sphere dS, the solid angle $d\Omega$ subtended by it is $d\Omega = r^{-2}dS$. Let $\boldsymbol{\Omega}$ be the unit vector perpendicular to dS as shown in fig 7.
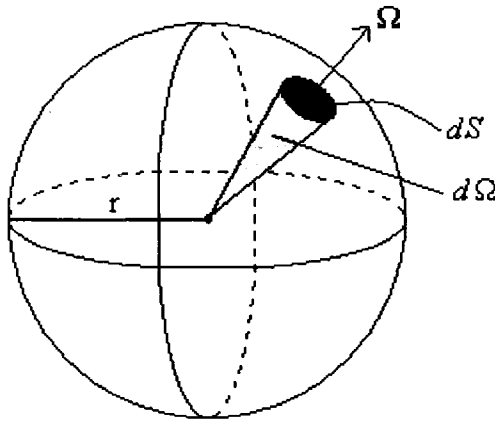
Fig. 7. Surface element dS and unit vector $\boldsymbol{\Omega}$ on a sphere of radius r.

The vector element of area $d\mathbf{S}$ is given by

$$d\mathbf{S} = \boldsymbol{\Omega}\,dS = \boldsymbol{\Omega}\,r^{2}d\Omega = r^{2}d\boldsymbol{\Omega} \qquad (2.11)$$

and $d\boldsymbol{\Omega} = \boldsymbol{\Omega}\,d\Omega$ is the solid angle $d\Omega$, in steradians (sr) about the direction $\boldsymbol{\Omega}$ [24].

Now that the solid angle has been introduced, the macroscopic production

cross section for a type k particle with energy in $(E', E'+dE')$ and direction $d\Omega'$ incident upon a type β atomic specie in which a type j particle with energy in $(E, E+dE)$ and direction $d\Omega$ is produced, can be defined as

$$\hat{\sigma}_{jk,\beta}(E, E', \Omega, \Omega') = \sigma_{k,\beta}(E')\nu_{jk,\beta}(E')\hat{f}_{jk,\beta}(E, E', \Omega, \Omega') \tag{2.12}$$

in units of $[cm^2 / g - MeV - sr]$, where $\sigma_{k,\beta}(E')$ has been defined. The quantity $\nu_{jk,\beta}(E')$ is the average number of type j particles produced by a type k particle with energy E' incident on a type β target atom, and is often referred to as a multiplicity. The quantity $\hat{f}_{jk,\beta}(E, E', \Omega, \Omega')$ is the probability density distribution for production of type j particles with energy E into the direction of Ω from a type k particle of energy E' and direction Ω' incident on a type β target atom; it has the units of $[(sr - MeV)^{-1}]$ [6]. The $\wedge$ notation will be used hereafter to denote angular dependence (Ω or Ω').

As with the microscopic and macroscopic cross-sections defined previously, the macroscopic production cross-section can be decomposed for different processes and summed to account for materials with multiple atomic species. The total macroscopic production cross-section is

$$\hat{\sigma}_{jk}(E, E', \Omega, \Omega') = \sum_{\beta} \left[\sigma_{k,\beta}^{el}(E')\nu_{jk,\beta}(E')\,\hat{f}_{jk,\beta}^{el}(E, E', \Omega, \Omega') \right.$$
$$\left. + \sigma_{k,\beta}^{re}(E')\nu_{jk,\beta}(E')\,\hat{f}_{jk,\beta}^{re}(E, E', \Omega, \Omega') \right] \tag{2.13}$$
$$+ \hat{\sigma}_{jk}^{at}(E, E', \Omega, \Omega')$$

where $\hat{f}_{jk,\beta}^{el}$, $\hat{f}_{jk,\beta}^{re}$ are the probability density distributions associated with elastic and atomic processes respectively. The production cross-section associated with atomic

processes, $\hat{\sigma}_{jk}^{at}(E,E',\Omega,\Omega')$ will be examined in detail later. Equation (2.13) suggests

that the total macroscopic production cross-sections can now be expressed as

$$\hat{\sigma}_{jk}(E,E',\Omega,\Omega') = \hat{\sigma}_{jk}^{el}(E,E',\Omega,\Omega')$$
$$+\hat{\sigma}_{jk}^{re}(E,E',\Omega,\Omega') \qquad (2.14)$$
$$+\hat{\sigma}_{jk}^{at}(E,E',\Omega,\Omega')$$

where again $\hat{\sigma}_{jk}^{el}$, $\hat{\sigma}_{jk}^{re}$, $\hat{\sigma}_{jk}^{at}$ are the total macroscopic production cross-sections

associated with elastic, reactive and atomic processes respectively. Note that

$\hat{\sigma}_{jk}(E,E',\Omega,\Omega')d\Omega\,dE\,dx$ is the probability that a type k particle with energy in

$(E',E'+dE')$ and direction $d\Omega'$ in moving a distance dx induces a reaction

producing a type j particle with energy in $(E, E + dE)$ and direction $d\Omega$. As before,

the quantity dx is a scaled depth in units of $[g/cm^2]$.

One last quantity that will be helpful for the next section is the stopping power.

Recall that a charged particle loses energy due to ionization as it passes through a

medium; the energy loss is certainly a discrete quantity, as it will only occur as it

interacts with individual particles. Since the distance between ionizing events is small

compared with the average path length, and the energy loss per event is also small, it

can be modeled as a continuous function. For a type j particle with energy E the

stopping power is given as [25]

$$S_j(E) = -\frac{dE}{dl} \qquad (2.15)$$

If l is measured in cm then the stopping power will be in units of $[MeV/cm]$; however

if the scaled depth x is used then

$$S_j(E) = -\frac{dE}{dx} \qquad (2.16)$$

will be in units of $[MeV / g / cm^2]$. From reference [6], the stopping power can also be expressed in terms of the macroscopic cross-section associated with atomic interactions as

$$S_j(E) = \sum_n \sigma_{jn}^{at}(E)\varepsilon_n \qquad (2.17)$$

where the subscript n denotes an excitation level, ε_n is an excitation energy, and $\sigma_{jn}^{at}(E)$ is the macroscopic atomic cross-section associated with the nth excitation level. The form of the stopping power given by equation (2.17) will be useful in representations of Boltzmann's equation given below.

THE BOLTZMANN TRANSPORT EQUATION

The history of the Boltzmann equation stretches back to the late 1800s when Boltzmann himself was defending his theories against attacks made by the so-called "school of energetics." Credited for inventing statistical mechanics as well as many other subjects in physics and mathematics, it was not until after his death that many of his theories were accepted. More recently, the Boltzmann equation has transformed from simply a mathematical oddity with limited interest, to a complete methodology covering a vast array of disciplines. For example, Boltzmann's equation or slight variations of it are now used in such fields as laser scattering, solid-state physics, nuclear transport, cell proliferation and traffic flow [26]. The derivation of the Boltzmann equation will of course depend on the field of application, but in all cases it can be described – possibly in a over simplified way – as a balance between

observable gains and losses within the physical system of interest. Appendix A offers

a derivation of the time dependent Boltzmann transport equation used here.

Recall that the kinetic energy of an object is related to its mass and velocity;

hence, the velocity can be found if it's kinetic energy is known. Further, let

$N_j(\mathbf{r}, E, \mathbf{\Omega}, t)$ be the total number of type j particles at position $\mathbf{r} = x\mathbf{e}_1 + y\mathbf{e}_2 + z\mathbf{e}_3$

with energy E moving in the direction of $\mathbf{\Omega} = \Omega_1\mathbf{e}_1 + \Omega_2\mathbf{e}_2 + \Omega_3\mathbf{e}_3$ at time t in units of

$[particles / cm^3 - MeV - sr]$. The vectors $\mathbf{e}_1$, $\mathbf{e}_2$, $\mathbf{e}_3$ are the usual basis vectors. Fig.

8 depicts the position vector $\mathbf{r}$ and direction vector $\mathbf{\Omega}$ below.
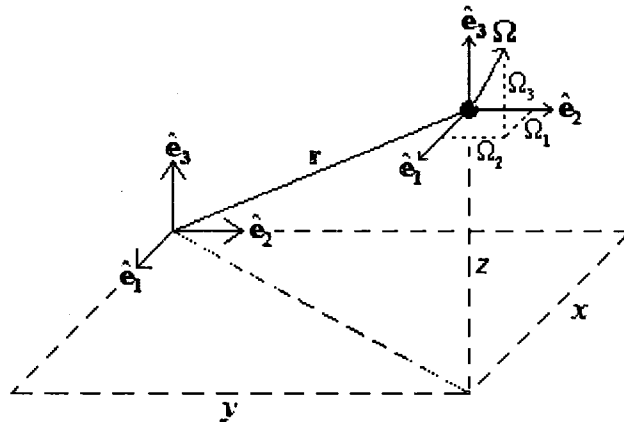
Fig. 8. The position vector $\mathbf{r}$ and direction vector $\mathbf{\Omega}$.

The flux of type j particles at position $\mathbf{r}$ with energy E moving in the direction

of $\mathbf{\Omega}$ at time t is given by [27]

$$\hat{\phi}_j^*(\mathbf{r}, E, \mathbf{\Omega}, t) = v \cdot N_j(\mathbf{r}, E, \mathbf{\Omega}, t) \qquad (2.18)$$

where v is the velocity of the particle. A dimensional analysis of equation (2.18)

implies that flux $\hat{\phi}_j^*$ will have the units $[particles/cm^2 - MeV - sr - \sec]$; the

superscript $*$ is used to denote time dependence. The time dependent Boltzmann

equation is given by

$$
\frac{1}{v}\frac{\partial}{\partial t}\hat{\phi}_j^*(\mathbf{r},E,\mathbf{\Omega},t) + \mathbf{\Omega}\cdot\nabla\hat{\phi}_j^*(\mathbf{r},E,\mathbf{\Omega},t) =
$$
$$
+ \sum_{k\geq j}\int_E\int_{\Omega}\hat{\sigma}_{jk}(E,E',\mathbf{\Omega},\mathbf{\Omega}')\hat{\phi}_k^*(\mathbf{r},E',\mathbf{\Omega}',t)\,d\mathbf{\Omega}'\,dE' \tag{2.19}
$$
$$
- \sigma_j(E)\hat{\phi}_j^*(\mathbf{r},E,\mathbf{\Omega},t)
$$

where the ∇ symbol is the gradient operator with respect to position. Recall from

equations (2.10) and (2.14) that the macroscopic cross-sections can be decomposed

into elastic, reactive and atomic interactions. The atomic production cross-section has

the approximate form

$$
\hat{\sigma}_{jk}^{at}(E,E',\mathbf{\Omega},\mathbf{\Omega}') = \sum_n\sigma_{kn}^{at}(E')\delta(\mathbf{\Omega}\cdot\mathbf{\Omega}'-1)\delta_{jk}\,\delta(E+\varepsilon_n-E') \tag{2.20}
$$

where δ_{jk} is the Kronecker delta, $\delta(\mathbf{\Omega}\cdot\mathbf{\Omega}'-1)$ and $\delta(E+\varepsilon_n-E')$ are the Dirac delta

functions, the subscript n denotes the electronic excitation levels, ε_n is a small

excitation energy, and σ_{kn}^{at} is the total macroscopic atomic cross-section associated

with the nth excitation level [6]. The terms on the right hand side of equation (2.19)

related to atomic interactions may then be written as

$$
\sum_{k\geq j}\int_E\int_{\Omega}\hat{\sigma}_{jk}^{at}(E,E',\mathbf{\Omega},\mathbf{\Omega}')\hat{\phi}_k^*(\mathbf{r},E',\mathbf{\Omega}',t)\,d\mathbf{\Omega}'\,dE' - \sigma_j^{at}(E)\hat{\phi}_j^*(\mathbf{r},E,\mathbf{\Omega},t)
$$
$$
= \sum_n\sigma_{jn}^{at}(E+\varepsilon_n)\hat{\phi}_j^*(\mathbf{r},E+\varepsilon_n,\mathbf{\Omega},t) - \sigma_j^{at}(E)\hat{\phi}_j^*(\mathbf{r},E,\mathbf{\Omega},t) \tag{2.21}
$$

The right hand side of equation (2.21) can be further expanded as a Taylor series about

the excitation energy ε_n. Neglecting terms of $O(\varepsilon_n^2)$ and higher, it is clear that

$$\sum_n \sigma_{jn}^{at}(E+\varepsilon_n)\,\hat{\phi}_j^*(\mathbf{r},E+\varepsilon_n,\mathbf{\Omega},t) - \sigma_j^{at}(E)\,\hat{\phi}_j^*(\mathbf{r},E,\mathbf{\Omega},t)$$

$$\approx \sum_n \left[\sigma_{jn}^{at}(E)\,\hat{\phi}_j^*(\mathbf{r},E,\mathbf{\Omega},t) + \varepsilon_n \frac{\partial}{\partial E}\Big(\sigma_{jn}^{at}(E)\,\hat{\phi}_j^*(\mathbf{r},E,\mathbf{\Omega},t)\Big) \right] \qquad (2.22)$$

$$- \sigma_j^{at}(E)\,\hat{\phi}_j^*(\mathbf{r},E,\mathbf{\Omega},t)$$

Note that the total macroscopic cross-section for atomic interactions can be expressed as

$$\sigma_j^{at}(E) = \sum_n \sigma_{jn}^{at}(E) \qquad (2.23)$$

so that the right hand side of equation (2.22) reduces to

$$\sum_n \varepsilon_n \frac{\partial}{\partial E}\Big(\hat{\sigma}_{jn}^{at}(E)\,\hat{\phi}_j^*(\mathbf{r},E,\mathbf{\Omega},t)\Big) \qquad (2.24)$$

Noting the form of the stopping power $S_j(E)$ given in equation (2.17) allows one to write the expression (2.24) in the compact form

$$\frac{\partial}{\partial E}\Big[S_j(E)\,\hat{\phi}_j^*(\mathbf{x},E,\mathbf{\Omega},t) \Big] \qquad (2.25)$$

The equation (2.19) is now expressed in the usual continuous slowing down approximation as

$$\frac{1}{v}\frac{\partial}{\partial t}\hat{\phi}_j^*(\mathbf{r},E,\mathbf{\Omega},t) + \mathbf{\Omega}\cdot\nabla\hat{\phi}_j^*(\mathbf{r},E,\mathbf{\Omega},t) - \frac{\partial}{\partial E}\Big[S_j(E)\,\hat{\phi}_j^*(\mathbf{r},E,\mathbf{\Omega},t) \Big]$$

$$+ \sigma_j(E)\hat{\phi}_j^*(\mathbf{r},E,\mathbf{\Omega},t) \qquad (2.26)$$

$$= \sum_{k\geq j}\int_E \int_{\mathbf{\Omega}} \hat{\sigma}_{jk}(E,E',\mathbf{\Omega},\mathbf{\Omega}')\,\hat{\phi}_k^*(\mathbf{r},E',\mathbf{\Omega}',t)\,d\mathbf{\Omega}'\,dE'$$

where the cross-sections now contain only the reactive and elastic contributions [6].

If a steady state distribution is assumed for $\hat{\phi}_j^*(\mathbf{r},E,\mathbf{\Omega},t)$, then

$$\lim_{t \to \infty} \hat{\phi}_j^*(\mathbf{r}, E, \mathbf{\Omega}, t) = \hat{\phi}_j(\mathbf{r}, E, \mathbf{\Omega}) \tag{2.27}$$

and

$$\lim_{t \to \infty} \frac{\partial}{\partial t} \hat{\phi}_j^*(\mathbf{r}, E, \mathbf{\Omega}, t) = 0 \tag{2.28}$$

Take the limit as $t \to \infty$ of equation (2.26), note equations (2.27) and (2.28) to obtain

$$\mathbf{\Omega} \cdot \nabla \hat{\phi}_j(\mathbf{r}, E, \mathbf{\Omega}) - \frac{\partial}{\partial E} \left[S_j(E) \, \hat{\phi}_j(\mathbf{r}, E, \mathbf{\Omega}) \right] + \sigma_j(E) \hat{\phi}_j(\mathbf{r}, E, \mathbf{\Omega})$$

$$= \sum_{k \geq j} \int_E \int_\mathbf{\Omega} \hat{\sigma}_{jk}(E, E', \mathbf{\Omega}, \mathbf{\Omega}') \hat{\phi}_k(\mathbf{r}, E', \mathbf{\Omega}') \, d\mathbf{\Omega}' \, dE' \tag{2.29}$$

Equation (2.29) is the time-independent Boltzmann equation, it will be used later when the neutron transport model is discussed in detail. For brevity, it is common to define the linear differential operator $B[\phi]$ as

$$B\left[\phi_j\right] \equiv \left[\mathbf{\Omega} \cdot \nabla - \frac{\partial}{\partial E} S_j(E) + \sigma_j(E) \right] \phi_j \tag{2.30}$$

so that the steady-state Boltzmann equation (2.29) can be expressed as

$$B\left[\hat{\phi}_j(\mathbf{r}, E, \mathbf{\Omega})\right] = \sum_{k \geq j} \int_E \int_\mathbf{\Omega} \hat{\sigma}_{jk}(E, E', \mathbf{\Omega}, \mathbf{\Omega}') \hat{\phi}_k(\mathbf{r}, E', \mathbf{\Omega}') \, d\mathbf{\Omega}' \, dE' \tag{2.31}$$

BI-DIRECTIONAL NEUTRON TRANSPORT MODEL

For heavier ions at relatively high energies the approximation can be made that all secondary particles produced move in the same direction as the primaries, resulting in a stream of particles propagating in one general direction; this is referred to as the straight-ahead approximation. These heavy ions are more likely to withstand direct collisions and atomic interactions without appreciably affecting their direction; hence the approximation is made that $\mathbf{\Omega} \cdot \mathbf{\Omega}' \approx 1$, ultimately leading to simplifications in equation (2.29). For lighter particles at low energies, collisions and atomic

interactions are more likely to result in angularly dependent scattering and hence the

Ω dependence needs more consideration [6,27-29].

In order to distinguish between propagation and interaction of high-energy

heavy ions and low-energy light ions, the reactive production cross-section appearing

in equation (2.14) needs to be examined, and special attention will be given for

neutron and proton ($j = 1, 2$) interactions. The probability density distribution for

reactive processes involving a proton projectile and neutron fragment or neutron

projectile and neutron fragment can be expressed in terms of the Ranft factor [30,31]

$$g\left(A_\beta, E, \theta\right) = \begin{cases} N \cdot e^{-\theta^2/\lambda} & , 0 < \theta < \pi/2 \\ N \cdot e^{-\pi^2/4\lambda} & , otherwise \end{cases}$$

(2.32)

as

$$\hat{f}_{jk,\beta}^{re}(E, E', \Omega, \Omega') = g(A_\beta, E, \theta) f_{jk,\beta}^{re}(E, E')$$

(2.33)

with $\lambda = (120 + 0.36 \cdot A_\beta)/E$, E the secondary particle energy in MeV, A_β the atomic

weight of the struck nucleus, θ the production angle, $f_{jk,\beta}^{re}(E, E')$ the angularly

independent probability density distribution in units of $[MeV^{-1}]$ and N a

normalization constant such that

$$2\pi \int_0^\pi g(A_\beta, E, \theta) d(\cos(\theta)) = 1$$

(2.34)

Fig. 9 depicts the angle θ in terms of the coordinate axes defined in fig. 8.
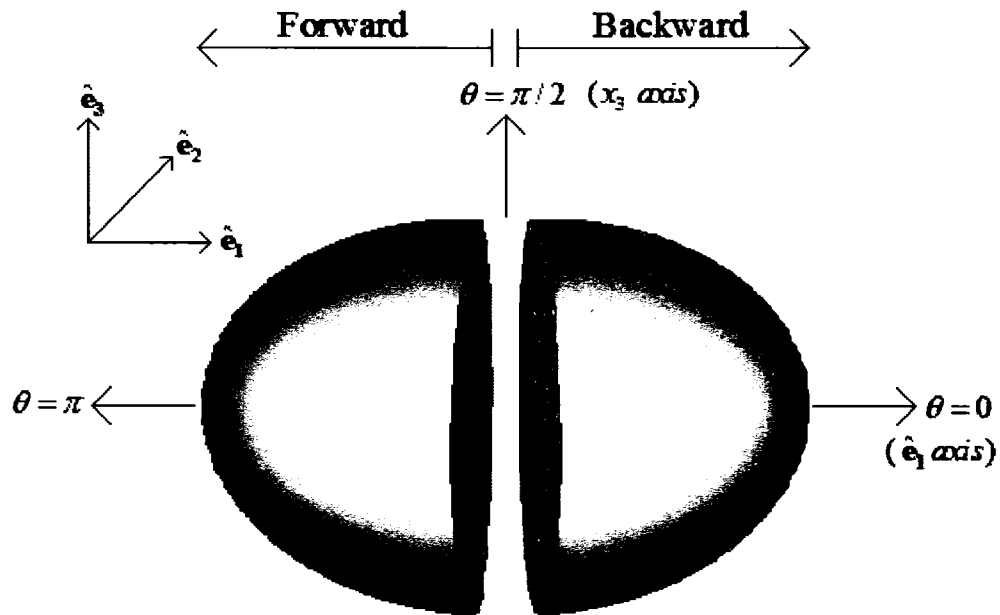
Fig. 9. Forward and backward hemispheres for isotropic scattering.

The production angle θ is defined in terms of the projectile and fragment directions of propagation as $\cos(\theta) = \Omega \cdot \Omega'$. For future reference, the right hemisphere for which $\theta \in [0, \pi/2]$ will be referred to as the forward direction $(\Delta\Omega^f)$, and the left hemisphere for which $\theta \in [\pi/2, \pi]$ will be referred to as the backward direction $(\Delta\Omega^b)$. The ray $\theta = 0$ exiting out the right hemisphere in the direction of the vector $\hat{e}_1$ will be referred to as the straight-ahead direction (Ω^{HZETRN}) and the small solid angle about the straight-ahead direction is $\Delta\Omega^{HZETRN}$.

From equation (2.32) and fig. 9 it is clear that the fraction of neutrons or protons produced in the forward direction is [30]

$$F_{for} = 2\pi \int_0^{\pi/2} g(A_\beta, E, \theta)\, d(\cos(\theta)) \tag{2.35}$$

Hence, the corresponding fraction produced in the backward direction is [30]

$$F_{back} = 1 - F_{for} \qquad (2.36)$$

Fig. 10 depicts the forward and backward components of the integrated Ranft model
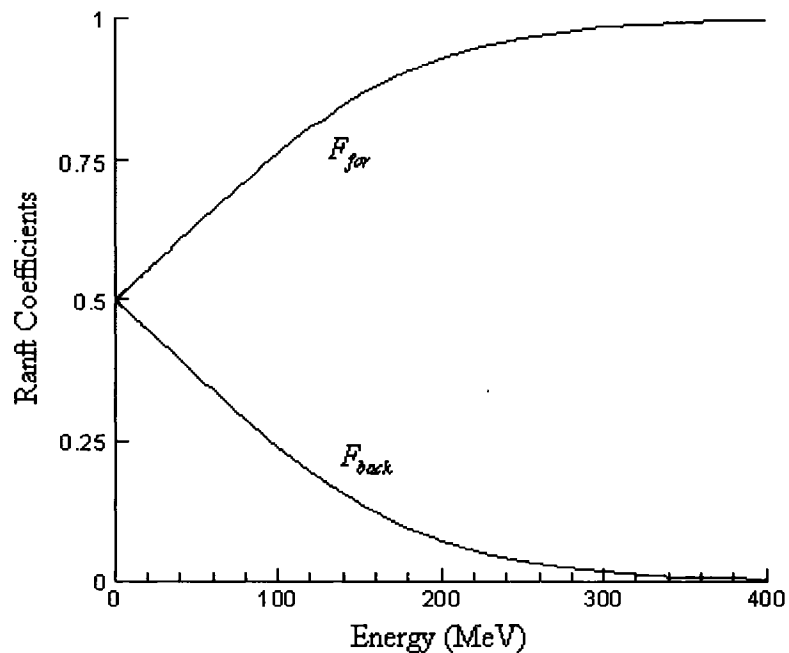
Fig. 10. Forward and backward integrated Ranft coefficients for aluminum target.

Since $F_{back} \ll 1$ at high fragment energies, the fraction of neutrons or protons

produced isotropically can be approximated by [30]

$$F_{iso} = 2 \cdot F_{back} \qquad (2.37)$$

so that the portion remaining the straight-ahead direction will be given by [30]

$$F_{HZETRN} = 1 - F_{iso} \qquad (2.38)$$

Fig. 11 depicts the isotropic and HZETRN components of the integrated Ranft model
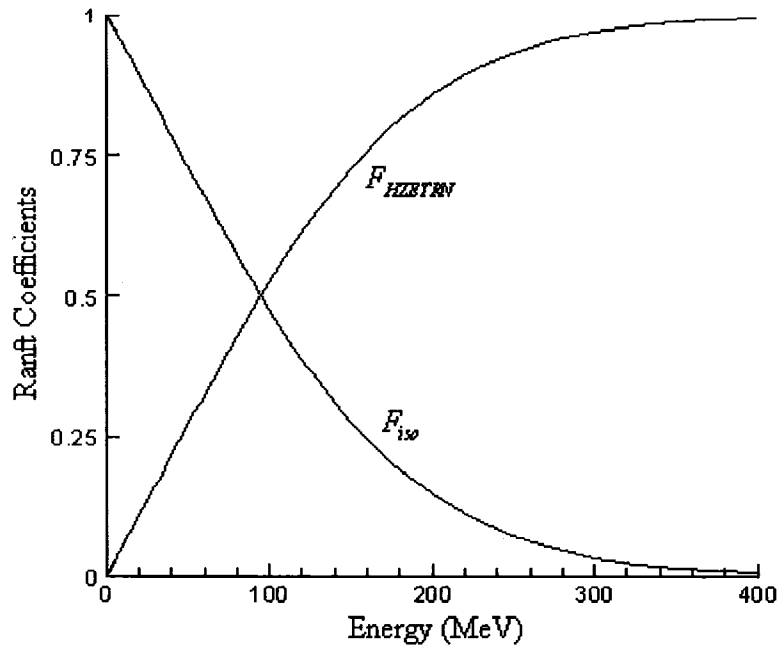
Fig. 11. Isotropic and HZETRN integrated Ranft coefficients for aluminum target

The coefficients F_{HZETRN} and F_{iso} can now be used to separate the reactive production

cross-section into a high-energy straight-ahead component and a low-energy isotropic

component. Let Ω_0 be an arbitrary unit direction vector, then

$$\sigma^{re}_{jk,\beta}(E,E') = \int_\Omega \hat{\sigma}^{re}_{jk,\beta}(E,E',\Omega_0,\Omega')d\Omega'$$

$$= \sigma^{re}_{k,\beta}(E')v_{jk,\beta}(E')f^{re}_{jk,\beta}(E,E')\int_\Omega g(A_\beta,E,\theta)d\Omega'$$

$$= \sigma^{re}_{k,\beta}(E')v_{jk,\beta}(E')f^{re}_{jk,\beta}(E,E')\int_{\Omega':\Omega_0\cdot\Omega'\approx1} g(A_\beta,E,\theta)d\Omega'$$

$$+\sigma^{re}_{k,\beta}(E')v_{jk,\beta}(E')f^{re}_{jk,\beta}(E,E')\int_{\Omega':\Omega_0\cdot\Omega'\neq1} g(A_\beta,E,\theta)d\Omega' \quad (2.39)$$

$$\approx \sigma^{re}_{k,\beta}(E')v_{jk,\beta}(E')f^{re}_{jk,\beta}(E,E')F_{HZETRN}$$

$$+\sigma^{re}_{k,\beta}(E')v_{jk,\beta}(E')f^{re}_{jk,\beta}(E,E')F_{iso}$$

$$\equiv \sigma^{HZETRN}_{jk,\beta}(E,E')+\sigma^{iso}_{jk,\beta}(E,E')$$

The quantity

$$\sigma^{re}_{jk,\beta}(E,E') = \sigma^{iso}_{jk,\beta}(E,E') + \sigma^{HZETRN}_{jk,\beta}(E,E') \tag{2.40}$$

is the angularly independent production cross-section in units of $[cm^2 / g - MeV]$.

Equation (2.39) suggests that one can also define the quantities

$$\sigma^{iso}_{jk,\beta}(E,E') = \sigma^{re}_{k,\beta}(E')v_{jk,\beta}(E')f^{iso}_{jk,\beta}(E,E') \tag{2.41}$$

$$\sigma^{HZETRN}_{jk,\beta}(E,E') = \sigma^{re}_{k,\beta}(E')v_{jk,\beta}(E')f^{HZETRN}_{jk,\beta}(E,E') \tag{2.42}$$

where $f^{iso}_{jk,\beta} = F_{iso} \cdot f^{re}_{jk,\beta}$ and $f^{HZETRN}_{jk,\beta} = F_{HZETRN} \cdot f^{re}_{jk,\beta}$. Fig. 12 depicts the isotropic and

HZETRN components of the probability density distribution for a $500\,MeV$ proton

projectile, aluminum target and neutron fragment.
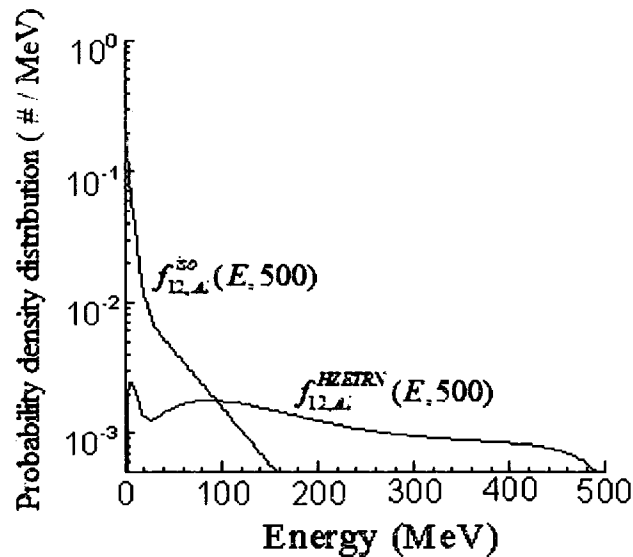
Fig. 12. Isotropic and HZETRN components of probability density distribution for $500\,MeV$ proton projectile, aluminum target and neutron fragment.

The isotropic cross-section, σ_{jk}^{iso}, is the dominant term in equation (2.40) for all

energies beneath a certain critical value, and σ_{jk}^{HZETRN} is the dominant term for all

energies above a certain critical value. This critical value will be material dependent,

but is usually in an energy regime near $100\ MeV$ [27]. The angularly independent

forms will be used later, but are given here to illustrate the separation of low energy

target fragments assumed to be produced isotropically and high-energy fragments

produced in the same general direction as the projectile.

We now proceed to decompose the angularly dependent production cross-

section and flux into isotropic and straight-ahead components. Define

$$\hat{f}_{jk,\beta}^{HZETRN}(E,E',\boldsymbol{\Omega},\boldsymbol{\Omega'}) = \begin{cases} \hat{f}_{jk,\beta}^{re}(E,E',\boldsymbol{\Omega},\boldsymbol{\Omega'}) & if\ \boldsymbol{\Omega},\boldsymbol{\Omega'} \in \Delta\boldsymbol{\Omega}^{HZETRN} \\ 0 & otherwise \end{cases} \tag{2.43}$$

and

$$\hat{f}_{jk,\beta}^{iso}(E,E',\boldsymbol{\Omega},\boldsymbol{\Omega'}) = \begin{cases} 0 & if\ \boldsymbol{\Omega},\boldsymbol{\Omega'} \in \Delta\boldsymbol{\Omega}^{HZETRN} \\ \hat{f}_{jk,\beta}^{re}(E,E',\boldsymbol{\Omega},\boldsymbol{\Omega'}) & otherwise \end{cases} \tag{2.44}$$

so that the reactive production cross-section can be expressed in the compact form

$$\hat{\sigma}_{jk,\beta}^{re}(E,E',\boldsymbol{\Omega},\boldsymbol{\Omega'}) = \hat{\sigma}_{jk,\beta}^{iso}(E,E',\boldsymbol{\Omega},\boldsymbol{\Omega'}) + \hat{\sigma}_{jk,\beta}^{HZETRN}(E,E',\boldsymbol{\Omega},\boldsymbol{\Omega'}) \tag{2.45}$$

The "*iso*" superscript is a bit deceiving here, but is introduced to denote all those

particles not produced in the same general direction as the projectile. As shown

above, the angular dependence can be integrated out ultimately leaving an

approximation to the isotropic production cross-section. Note also that the

directionally dependent production cross-section is now fully decomposed as

$$\hat{\sigma}_{jk} = \hat{\sigma}_{jk}^{el} + \left(\hat{\sigma}_{jk}^{HZETRN} + \hat{\sigma}_{jk}^{iso}\right) \tag{2.46}$$

The differential flux can also be decomposed into a high-energy straight ahead component and low-energy isotropic component as

$$\hat{\phi}_j(\mathbf{r},E,\mathbf{\Omega}) = \hat{\phi}_j^{HZETRN}(\mathbf{r},E,\mathbf{\Omega}) + \hat{\phi}_j^{iso}(\mathbf{r},E,\mathbf{\Omega}) \tag{2.47}$$

for $j = 1,2$ - neutrons and protons. The case $j > 2$ will be accounted for shortly. Following references [16,25,27,30], substitute equations (2.46) and (2.47) into equation (2.31) and obtain

$$\begin{aligned} B\left[\hat{\phi}_j^{HZETRN}\right] &+ B\left[\hat{\phi}_j^{iso}\right] \\ &= \sum_{k \geq j} \int_E \int_\Omega \left[\hat{\sigma}_{jk}^{el} + \left(\hat{\sigma}_{jk}^{HZETRN} + \hat{\sigma}_{jk}^{iso}\right)\right]\left[\hat{\phi}_k^{HZETRN} + \hat{\phi}_k^{iso}\right]d\mathbf{\Omega'}\,dE' \end{aligned} \tag{2.48}$$

Define the following integrals

$$\hat{I}_k^{el}\left[\hat{\phi}_k\right] = \int_E \int_\Omega \hat{\sigma}_{kk}^{el}(E,E',\mathbf{\Omega},\mathbf{\Omega'})\,\hat{\phi}_k(\mathbf{r},E,\mathbf{\Omega'})\,d\mathbf{\Omega'}\,dE' \tag{2.49}$$

$$\hat{I}_j^{HZETRN}\left[\phi_k\right] = \sum_{k \geq j} \int_E \int_\Omega \hat{\sigma}_{jk}^{HZETRN}(E,E',\mathbf{\Omega},\mathbf{\Omega'})\,\hat{\phi}_k(\mathbf{r},E,\mathbf{\Omega'})\,d\mathbf{\Omega'}\,dE' \tag{2.50}$$

$$\hat{I}_j^{iso}\left[\phi_k\right] = \sum_{k \geq j} \int_E \int_\Omega \hat{\sigma}_{jk}^{iso}(E,E',\mathbf{\Omega},\mathbf{\Omega'})\,\hat{\phi}_k(\mathbf{r},E,\mathbf{\Omega'})\,d\mathbf{\Omega'}\,dE' \tag{2.51}$$

so that equation (2.48) can be re-written as

$$\begin{aligned} B\left[\hat{\phi}_j^{HZETRN}\right] + B\left[\hat{\phi}_j^{iso}\right] &= \hat{I}_j^{el}\left[\hat{\phi}_j^{HZETRN}\right] + \hat{I}_j^{el}\left[\hat{\phi}_j^{iso}\right] \\ &+ \hat{I}_j^{HZETRN}\left[\hat{\phi}_k^{HZETRN}\right] + \hat{I}_j^{HZETRN}\left[\hat{\phi}_k^{iso}\right] \\ &+ \hat{I}_j^{iso}\left[\hat{\phi}_k^{HZETRN}\right] + \hat{I}_j^{iso}\left[\hat{\phi}_k^{iso}\right] \end{aligned} \tag{2.52}$$

Note that the sum over particle type has been dropped in the definition of $\hat{I}_k^{el}$ since $\hat{\sigma}_{jk}^{el} = 0$ for $j \neq k$. For example, neutrons cannot produce protons through elastic processes. Since we are interested in the neutron flux, equation (2.52) for the case $j=1$ becomes

$$B\left[\hat{\phi}_1^{HZETRN}\right] + B\left[\hat{\phi}_1^{iso}\right] = \hat{I}_1^{el}\left[\hat{\phi}_1^{HZETRN}\right] + \hat{I}_1^{el}\left[\hat{\phi}_1^{iso}\right]$$

$$+ \hat{I}_1^{HZETRN}\left[\hat{\phi}_k^{HZETRN}\right] + \hat{I}_1^{HZETRN}\left[\hat{\phi}_k^{iso}\right] \tag{2.53}$$

$$+ \hat{I}_1^{iso}\left[\hat{\phi}_k^{HZETRN}\right] + \hat{I}_1^{iso}\left[\hat{\phi}_k^{iso}\right]$$

Equation (2.53) can be further regrouped as

$$B\left[\hat{\phi}_1^{iso}\right] + B\left[\hat{\phi}_1^{HZETRN}\right] = \left\{\hat{I}_1^{el}\left[\hat{\phi}_1^{HZETRN}\right] + \hat{I}_1^{HZETRN}\left[\hat{\phi}_k^{HZETRN}\right]\right\}$$

$$+ \hat{I}_1^{el}\left[\hat{\phi}_1^{iso}\right] + \hat{I}_1^{HZETRN}\left[\hat{\phi}_k^{iso}\right] + \hat{I}_1^{iso}\left[\hat{\phi}_k^{iso}\right] \tag{2.54}$$

$$+ \hat{I}_1^{iso}\left[\hat{\phi}_k^{HZETRN}\right]$$

The program HZETRN-05 developed by John Wilson et. al. at NASA LaRC [6,9-15] is used to solve the equation

$$B\left[\hat{\phi}_1^{HZETRN}\right] = \hat{I}_1^{el}\left[\hat{\phi}_1^{HZETRN}\right] + \hat{I}_1^{HZETRN}\left[\hat{\phi}_k^{HZETRN}\right] \tag{2.55}$$

For the case $j = 2$, the equation to be solved is exactly the same in form as equation (2.54); hence, HZETRN-05 is used to solve

$$B\left[\hat{\phi}_2^{HZETRN}\right] = \hat{I}_2^{el}\left[\hat{\phi}_2^{HZETRN}\right] + \hat{I}_2^{HZETRN}\left[\hat{\phi}_k^{HZETRN}\right] \tag{2.56}$$

and to solve equation (2.31) for the case $j > 2$. Upon examination of equation (2.54), it is clear that we are left to solve for the isotropic component of the neutron flux satisfying the equation

$$B\left[\hat{\phi}_1^{iso}\right] = \hat{I}_1^{el}\left[\hat{\phi}_1^{iso}\right] + \hat{I}_1^{HZETRN}\left[\hat{\phi}_k^{iso}\right] + \hat{I}_1^{iso}\left[\hat{\phi}_k^{iso}\right] + \hat{I}_1^{iso}\left[\hat{\phi}_k^{HZETRN}\right] \tag{2.57}$$

Define the source term $\hat{Q}(\mathbf{r}, E, \Omega)$ as

$$\hat{Q}(\mathbf{r}, E, \Omega) = \hat{I}_1^{iso}\left[\hat{\phi}_k^{HZETRN}\right]$$

$$= \sum_{k \geq 1} \int_E^\infty \int_\Omega \hat{\sigma}_{jk}^{iso} \hat{\phi}_k^{HZETRN} d\Omega' dE' \tag{2.58}$$

so that equation (2.57) can be re-written as

$$B\left[\hat{\phi}_1^{iso}\right] = \hat{I}_1^{el}\left[\hat{\phi}_1^{iso}\right] + \hat{I}_1^{HZETRN}\left[\hat{\phi}_k^{iso}\right] + \hat{I}_1^{iso}\left[\hat{\phi}_k^{iso}\right] + \hat{Q}(\mathbf{r}, E, \mathbf{\Omega}) \qquad (2.59)$$

The quantity $\hat{Q}(\mathbf{r}, E, \mathbf{\Omega})$ represents the source of isotropic secondary neutrons produced from a high-energy straight-ahead primary stream of particles.

Henceforth, we will be dealing with only the low-energy isotropic neutron flux and so the *iso* superscript and particle subscript notation will be dropped. (i.e. $\hat{\phi}$ will represent the low-energy isotropic neutron flux). Also note that since we are dealing with low-energy charged projectiles, there will be very little fragmentation [6] and so the sum over particle type can be dropped yielding

$$\mathbf{\Omega} \cdot \nabla \hat{\phi} + \sigma_1(E)\hat{\phi} = \int_E \int_\Omega \left(\hat{\sigma}_{11}^{re} + \hat{\sigma}_{11}^{el}\right)\hat{\phi}_k \, d\mathbf{\Omega}' dE' + \hat{Q}(\mathbf{r}, E, \mathbf{\Omega}) \qquad (2.60)$$

To further simplify equation (2.59), examine the elastic and reactive production cross-sections, $\hat{\sigma}_{11}^{el}$ and $\hat{\sigma}_{11}^{re}$.

First note that all of the projectile neutrons considered here will have relatively low energy; therefore the secondary particles produced – if any – will be produced in an isotropic manner. Note the integrated Ranft coefficients defined in equations (2.35) and (2.36), and let $\mathbf{\Omega}_0^f \in \Delta\mathbf{\Omega}^f$ be an arbitrary unit vector. Then

$$\sigma_{11,\beta}^{re}(E,E') = \int_{\Omega} \hat{\sigma}_{11,\beta}^{re}(E,E',\Omega_0^f,\Omega')\,d\Omega'$$

$$= \sigma_{1,\beta}^{re}(E')v_{11,\beta}(E')f_{11,\beta}^{re}(E,E')\int_{\Omega} g(A_\beta,E,\theta)\,d\Omega'$$

$$= \sigma_{1,\beta}^{re}(E')v_{11,\beta}(E')f_{11,\beta}^{re}(E,E')\int_{\Omega'\in\Delta\Omega^f} g(A_\beta,E,\theta)\,d\Omega'$$

$$+\sigma_{1,\beta}^{re}(E')v_{11,\beta}(E')f_{11,\beta}^{re}(E,E')\int_{\Omega'\in\Delta\Omega^b} g(A_\beta,E,\theta)\,d\Omega' \qquad (2.61)$$

$$\approx \sigma_{1,\beta}^{re}(E')v_{11,\beta}(E')f_{11,\beta}^{re}(E,E')F_{for}$$

$$+\sigma_{1,\beta}^{re}(E')v_{11,\beta}(E')f_{11,\beta}^{re}(E,E')F_{back}$$

$$\equiv \sigma_{11,\beta}^{re(+)}(E,E')+\sigma_{11,\beta}^{re(-)}(E,E')$$

where $\sigma_{11,\beta}^{re(+)}(E,E')$ denotes a scattering angle between $\theta = 0$ and $\theta = \pi/2$, and

$\sigma_{11,\beta}^{re(-)}(E,E')$ denotes a scattering angle between $\theta = \pi/2$ and $\theta = \pi$. Similarly, if we

let $\Omega_0^b \in \Delta\Omega^b$ be an arbitrary unit vector, then

$$\sigma_{11,\beta}^{re}(E,E') = \int_{\Omega} \hat{\sigma}_{11,\beta}^{re}(E,E',\Omega_0^b,\Omega')\,d\Omega'$$

$$= \sigma_{1,\beta}^{re}(E')v_{11,\beta}(E')f_{11,\beta}^{re}(E,E')\int_{\Omega} g(A_\beta,E,\theta)\,d\Omega'$$

$$= \sigma_{1,\beta}^{re}(E')v_{11,\beta}(E')f_{11,\beta}^{re}(E,E')\int_{\Omega'\in\Delta\Omega^f} g(A_\beta,E,\theta)\,d\Omega'$$

$$+\sigma_{1,\beta}^{re}(E')v_{11,\beta}(E')f_{11,\beta}^{re}(E,E')\int_{\Omega'\in\Delta\Omega^b} g(A_\beta,E,\theta)\,d\Omega' \qquad (2.62)$$

$$\approx \sigma_{1,\beta}^{re}(E')v_{11,\beta}(E')f_{11,\beta}^{re}(E,E')F_{back}$$

$$+\sigma_{1,\beta}^{re}(E')v_{11,\beta}(E')f_{11,\beta}^{re}(E,E')F_{for}$$

$$\equiv \sigma_{11,\beta}^{re(-)}(E,E')+\sigma_{11,\beta}^{re(+)}(E,E')$$

Equations (2.61) and (2.62) suggest that the angularly independent cross-section can

be expressed as

$$\sigma_{jk,\beta}^{re}(E,E') = \sigma_{jk,\beta}^{re(+)}(E,E')+\sigma_{jk,\beta}^{re(-)}(E,E') \qquad (2.63)$$

This analysis has shown that the reactive production cross-section can be decomposed

into two parts: one part for the projectile and fragment propagating in the same

hemisphere and one part for the projectile and fragment propagating in opposite hemispheres.

The forward and backward components of the elastic production cross-section are modeled by considering the neutron energy before and after an elastic collision. The neutron energy E after an elastic collision with a nucleus of mass number A_β is given by

$$E = E'\left[\frac{A_\beta + 2A_\beta\cos\theta + 1}{(A_\beta + 1)^2}\right] \qquad (2.64)$$

where θ is the angle depicted in fig. 9 [16,25,27,30]. For scattering angles between $\theta = 0$ and $\theta = \pi/2$ the projectile energy E' must be contained in the interval $[E, E/\alpha_\beta^*]$ where

$$\alpha_\beta^* = \frac{A_\beta^2 + 1}{(A_\beta + 1)^2} \qquad (2.65)$$

and for scattering angles between $\theta = \pi/2$ and $\theta = \pi$ the projectile energy E' must be contained in the interval $[E/\alpha_\beta^*, E/\alpha_\beta]$ where

$$\alpha_\beta = \left(\frac{A_\beta - 1}{A_\beta + 1}\right)^2 \qquad (2.66)$$

Following the procedure outlined in equations (2.61) and (2.62), let $\Omega_0^f \in \Delta\Omega^f$ be an arbitrary unit vector so that

$$\sigma_{11,\beta}^{el}(E,E') = \int_{\Omega} \hat{\sigma}_{11,\beta}^{el}(E,E',\Omega_0^f,\Omega')\, d\Omega'$$

$$= \sigma_{1,\beta}^{el}(E')v_{11,\beta}(E') \int_{\Omega'\in\Delta\Omega^f} \hat{f}_{11,\beta}^{el}(E,E',\Omega_0^f,\Omega')\, d\Omega'$$

$$+\sigma_{1,\beta}^{el}(E')v_{11,\beta}(E') \int_{\Omega'\in\Delta\Omega^b} \hat{f}_{11,\beta}^{el}(E,E',\Omega_0^f,\Omega')\, d\Omega' \qquad (2.67)$$

$$\equiv \sigma_{1,\beta}^{el}(E')v_{11,\beta}(E')f_{11,\beta}^{el(+)}(E,E')$$

$$+\sigma_{1,\beta}^{el}(E')v_{11,\beta}(E')f_{11,\beta}^{el(-)}(E,E')$$

$$\equiv \sigma_{11,\beta}^{el(+)}(E,E') + \sigma_{11,\beta}^{el(-)}(E,E')$$

where $\sigma_{11,\beta}^{el(+)}(E,E')$ refers to scattering angles between $\theta = 0$ and $\theta = \pi/2$ and is non-zero for $E' \in [E, E/\alpha_\beta^*]$, while $\sigma_{11,\beta}^{el(-)}(E,E')$ refers to scattering angles between

$\theta = \pi/2$ and $\theta = \pi$ and is non-zero for $E' \in [E/\alpha_\beta^*, E/\alpha_\beta]$. Similarly, let $\Omega_0^b \in \Delta\Omega^b$

be an arbitrary unit vector so that

$$\sigma_{11,\beta}^{el}(E,E') = \int_{\Omega} \hat{\sigma}_{11,\beta}^{el}(E,E',\Omega_0^b,\Omega')\, d\Omega'$$

$$= \sigma_{1,\beta}^{el}(E')v_{11,\beta}(E') \int_{\Omega'\in\Delta\Omega^f} \hat{f}_{11,\beta}^{el}(E,E',\Omega_0^b,\Omega')\, d\Omega'$$

$$+\sigma_{1,\beta}^{el}(E')v_{11,\beta}(E') \int_{\Omega'\in\Delta\Omega^b} \hat{f}_{11,\beta}^{el}(E,E',\Omega_0^b,\Omega')\, d\Omega' \qquad (2.68)$$

$$\equiv \sigma_{1,\beta}^{el}(E')v_{11,\beta}(E')f_{11,\beta}^{el(-)}(E,E')$$

$$+\sigma_{1,\beta}^{el}(E')v_{11,\beta}(E')f_{11,\beta}^{el(+)}(E,E')$$

$$\equiv \sigma_{11,\beta}^{el(-)}(E,E') + \sigma_{11,\beta}^{el(+)}(E,E')$$

As before, it has now been shown that the elastic production cross-section can be

decomposed into two parts: one part for the projectile and fragment propagating in the

same hemisphere and one part for the projectile and fragment propagating in opposite

hemispheres.

The source term $\hat{Q}(\mathbf{r},E,\Omega)$ must be now be decomposed as well; recall that it

was generated by computing the integral

$$\hat{Q}(\mathbf{r},E,\Omega) = \sum_{k\geq 1} \int_E \int_\Omega \hat{\sigma}_{1k}^{iso}(E,E',\Omega,\Omega')\hat{\phi}_k^{HZETRN}(\mathbf{r},E',\Omega')\, d\Omega'\, dE'. \qquad (2.69)$$

The solution $\hat{\phi}_k^{HZETRN}$ represents a flux of type k particles sharply peaked in the forward direction. Further, the reactive cross-section in equation (2.69) is assumed to be spherically symmetric, which implies that $\hat{Q}$ should be independent of the fragment direction Ω. Therefore, the portion produced in the forward direction can be approximated by

$$\hat{\eta}^f(x,E,\Omega) = \frac{1}{2}Q(x,E,\Omega^f) \tag{2.70}$$

and the portion produced in the backward direction is approximated by taking

$$\hat{\eta}^b(x,E,\Omega) = \frac{1}{2}Q(x,E,\Omega^b) \tag{2.71}$$

where $\Omega^f \in \Delta\Omega^f$, $\Omega^b \in \Delta\Omega^b$ are arbitrary vectors and x is the depth into the material measured along the positive x_1 axis. The forward and backward components are assumed to be constant with respect to angle in their respective hemispheres; therefore, one can define

$$\begin{aligned}
\eta^f(x,E) &= \int_{\Delta\Omega^f} \hat{\eta}^f(x,E,\Omega)\,d\Omega \\
&= \Delta\Omega^f \hat{\eta}^f(x,E,\Omega^f)
\end{aligned} \tag{2.72}$$

$$\begin{aligned}
\eta^b(x,E) &= \int_{\Delta\Omega^b} \hat{\eta}^b(x,E,\Omega)\,d\Omega \\
&= \Delta\Omega^b \hat{\eta}^b(x,E,\Omega^b)
\end{aligned} \tag{2.73}$$

where $\Omega^f \in \Delta\Omega^f$, $\Omega^b \in \Delta\Omega^b$ are arbitrary vectors.

Finally, the isotropic component of the neutron flux needs to broken up into forward and backward components. The portion of particles propagating in the forward direction is given as

$$\int_{\Delta\Omega^f} \hat{\phi}(\mathbf{x},E,\mathbf{\Omega'})\,d\mathbf{\Omega'} \approx \Delta\Omega^f\,\hat{\phi}(\mathbf{x},E,\mathbf{\Omega^f})$$

$$\equiv \phi^f(x,E)$$

(2.74)

and the portion propagating in the backward direction is given by

$$\int_{\Delta\Omega^b} \hat{\phi}(\mathbf{x},E,\mathbf{\Omega'})\,d\mathbf{\Omega'} \approx \Delta\Omega^b\,\hat{\phi}(\mathbf{x},E,\mathbf{\Omega^b})$$

$$\equiv \phi^b(x,E)$$

(2.75)

where $\mathbf{\Omega^f} \in \Delta\Omega^f$ and $\mathbf{\Omega^b} \in \Delta\Omega^b$ are arbitrary vectors.

Now return to equation (2.60) and evaluate it at $\mathbf{\Omega^f} = <1,0,0>$. The left hand

side becomes

$$\mathbf{\Omega^f} \cdot \nabla\hat{\phi} + \sigma_1(E)\hat{\phi} = \frac{\partial}{\partial x}\hat{\phi}(x,E,\mathbf{\Omega^f}) + \sigma_1(E)\hat{\phi}(x,E,\mathbf{\Omega^f})$$

(2.76)

and the integral source term on the right hand side becomes

$$I = \int_E \int_\Omega \left(\hat{\sigma}_{11}^{re} + \hat{\sigma}_{11}^{el}\right)\hat{\phi}\,d\mathbf{\Omega'}\,dE'$$

$$= \int_E \left[\left(\int_\Omega \hat{\sigma}_{11}^{re}\,\hat{\phi}\,d\mathbf{\Omega'}\right) + \left(\int_\Omega \hat{\sigma}_{11}^{el}\,\hat{\phi}\,d\mathbf{\Omega'}\right)\right]dE'$$

(2.77)

The reactive and elastic production cross-sections have been decomposed into forward

and backward components, and so I can be written in the more useful form

$$I = \int_E \left[\int_{\Delta\Omega^f} \hat{\sigma}_{11}^{re}\,\hat{\phi}\,d\mathbf{\Omega'} + \int_{\Delta\Omega^b} \hat{\sigma}_{11}^{re}\,\hat{\phi}\,d\mathbf{\Omega'}\right.$$

$$\left. + \int_{\Delta\Omega^f} \hat{\sigma}_{11}^{el}\,\hat{\phi}\,d\mathbf{\Omega'} + \int_{\Delta\Omega^b} \hat{\sigma}_{11}^{el}\,\hat{\phi}\,d\mathbf{\Omega'}\right]dE'$$

(2.78)

Noting that $\hat{\phi}$ is approximately constant with respect to angle in the forward and

backward hemispheres implies that equation (2.78) can be rewritten as

$$I = \int_E \begin{bmatrix} \hat{\phi}(x,E,\Omega_0^f) \int_{\Delta\Omega^f} \hat{\sigma}_{11}^{re}(E,E',\Omega^f,\Omega')d\Omega' \\ +\hat{\phi}(x,E,\Omega_0^f) \int_{\Delta\Omega^f} \hat{\sigma}_{11}^{el}(E,E',\Omega^f,\Omega')d\Omega' \\ +\hat{\phi}(x,E,\Omega_0^b) \int_{\Delta\Omega^b} \hat{\sigma}_{11}^{re}(E,E',\Omega^f,\Omega')d\Omega' \\ +\hat{\phi}(x,E,\Omega_0^b) \int_{\Delta\Omega^b} \hat{\sigma}_{11}^{el}(E,E',\Omega^f,\Omega')d\Omega' \end{bmatrix} dE' \qquad (2.79)$$

where $\Omega_0^f \in \Delta\Omega^f$ and $\Omega_0^b \in \Delta\Omega^b$ are arbitrary vectors. Finally, equations (2.61) and

(2.67) imply

$$I = \int_E \begin{bmatrix} \hat{\sigma}_{11}^{re(+)}(E,E')\hat{\phi}(x,E',\Omega_0^f) \\ +\hat{\sigma}_{11}^{re(-)}(E,E')\hat{\phi}(x,E',\Omega_0^b) \\ +\hat{\sigma}_{11}^{el(+)}(E,E')\hat{\phi}(x,E',\Omega_0^f) \\ +\hat{\sigma}_{11}^{el(-)}(E,E')\hat{\phi}(x,E',\Omega_0^b) \end{bmatrix} dE' \qquad (2.80)$$

Therefore, equation (2.60) for the case $\Omega^f = <1,0,0>$ is given as

$$\frac{\partial}{\partial x}\hat{\phi}(x,E,\Omega^f) + \sigma_1(E)\hat{\phi}(x,E,\Omega^f) = \int_E^\infty \hat{\sigma}_{11}^{re(+)}(E,E')\hat{\phi}(x,E',\Omega_0^f)dE'$$

$$+ \int_E^\infty \hat{\sigma}_{11}^{re(-)}(E,E')\hat{\phi}(x,E',\Omega_0^b)dE'$$

$$+ \int_E \hat{\sigma}_{11}^{el(+)}(E,E')\hat{\phi}(x,E',\Omega_0^f)dE' \qquad (2.81)$$

$$+ \int_E \hat{\sigma}_{11}^{el(-)}(E,E')\hat{\phi}(x,E',\Omega_0^b)dE'$$

$$+ \hat{\eta}^f(x,E,\Omega^f)$$

Equation (2.81) describes the neutron flux propagating in the direction of the positive

x_1 axis. Note that the vector $\Omega^f = <1,0,0>$ was chosen in order to simplify the form

of the left hand side, but since the forward flux is assumed to be independent of

direction in the right hemisphere, one can integrate equation (2.81) over all forward

directions to obtain the total neutron flux propagating in the forward direction. Note

equation (2.74) and the left hand side of equation (2.81) becomes

39

$$\frac{\partial}{\partial x}\phi^f(x,E)+\sigma_1(E)\phi^f(x,E) \tag{2.82}$$

Similarly, the right hand side becomes

$$
\begin{aligned}
I = &\int_E^\infty \sigma_{11}^{re(+)}(E,E')\phi^f(x,E')dE' \\
&+\int_E^\infty \sigma_{11}^{re(-)}(E,E')\phi^b(x,E')dE' \\
&+\int_E \sigma_{11}^{el(+)}(E,E')\phi^f(x,E')dE' \\
&+\int_E \sigma_{11}^{el(-)}(E,E')\phi^b(x,E')dE \\
&+\eta^f(x,E)
\end{aligned} \tag{2.83}
$$

Therefore, the equation for the forward component of the neutron flux is

$$
\begin{aligned}
\frac{\partial}{\partial x}&\phi^f(x,E)+\sigma_1(E)\phi^f(x,E) \\
&=\int_E(\sigma_{11}^{el(+)}+\sigma_{11}^{re(+)})\phi^f(x,E')dE' \\
&+\int_E(\sigma_{11}^{el(-)}+\sigma_{11}^{re(-)})\phi^b(x,E')dE' \\
&+\eta^f(x,E)
\end{aligned} \tag{2.84}
$$

Choosing the vector $\mathbf{\Omega^b}=<-1,0,0>$, and following the above analysis yields the equation for the backward component of the neutron flux

$$
\begin{aligned}
-\frac{\partial}{\partial x}&\phi^b(x,E)+\sigma_1(E)\phi^b(x,E) \\
&=\int_E(\sigma_{11}^{el(+)}+\sigma_{11}^{re(+)})\phi^b(x,E')dE' \\
&+\int_E(\sigma_{11}^{el(-)}+\sigma_{11}^{re(-)})\phi^f(x,E')dE' \\
&+\eta^b(x,E)
\end{aligned} \tag{2.85}
$$

Now that the problem has been reduced to one spatial dimension, the target material can be described as a slab of material of length L. As such, the forward component of the flux will have a boundary condition at the front of the material, which can be defined as

$$\phi^f(0, E) = 0 \tag{2.86}$$

The backward component will have a boundary condition at the back of the material, which can be defined as

$$\phi^b(L, E) = 0 \tag{2.87}$$

The homogeneous front and back boundary conditions will be used hereafter to develop the solution methods in chapter III, but it is a trivial exercise to generalize to non-homogeneous conditions. Also note that the total flux of neutrons at depth x with energy E is

$$\phi^{tot}(x, E) = \phi^{HZETRN} + \left(\phi^f(x, E) + \phi^b(x, E)\right) \tag{2.88}$$

Remember that the terms $\sigma_{11}^{el(+)}$ and $\sigma_{11}^{re(+)}$ are the elastic and reactive production cross-sections associated with a secondary particle produced in the same general direction as the primary, while $\sigma_{11}^{el(-)}$ and $\sigma_{11}^{re(-)}$ are the elastic and reactive production cross-sections associated with a secondary particle produced in the opposite direction as the primary. Therefore, the integral

$$\int_E (\sigma_{11}^{el(-)} + \sigma_{11}^{re(-)}) \phi^b(x, E') dE' \tag{2.89}$$

appearing in equation (2.84) represents the source of neutrons produced in the forward direction by a backward propagating flux, and the integral

$$\int_E (\sigma_{11}^{el(-)} + \sigma_{11}^{re(-)}) \phi^f(x, E') dE' \tag{2.90}$$

appearing in equation (2.85) represents the source of neutrons produced in the backward direction by a forward propagating flux.

Recall also that the forward and backward cross-sections are sensitive to projectile energy and hence the limits of integration must be made explicit. First define the linear differential operators for flux production in the forward (f) and backward (b) directions as

$$B_f[\phi] \equiv \left[\frac{\partial}{\partial x} + \sigma_1(E) \right] \phi \qquad (2.91)$$

$$B_b[\phi] \equiv \left[-\frac{\partial}{\partial x} + \sigma_1(E) \right] \phi \qquad (2.92)$$

then for a target material with β distinct atomic species, the coupled system of equations describing the forward and backward components of the low-energy isotropic neutron flux is given as

$$
\begin{aligned}
B_f[\phi^f(x,E)] = \sum_\beta \Bigg[& \int_E^{E/\alpha_\beta^*} \sigma_{11,\beta}^{el}(E,E') \; \phi^f(x,E')dE' \\
& + \int_E^\infty \sigma_{11,\beta}^{re(+)}(E,E') \; \phi^f(x,E')dE' \\
& + \int_{E/\alpha_\beta^*}^{E/\alpha_\beta} \sigma_{11,\beta}^{el}(E,E') \; \phi^b(x,E')dE' \qquad (2.93) \\
& + \int_E^\infty \sigma_{11,\beta}^{re(-)}(E,E') \; \phi^b(x,E')dE' \Bigg] \\
& + \eta^f(x,E)
\end{aligned}
$$

$$
\begin{aligned}
B_b[\phi^b(x,E)] = \sum_\beta \Bigg[& \int_E^{E/\alpha_\beta^*} \sigma_{11,\beta}^{el}(E,E') \; \phi^b(x,E')dE' \\
& + \int_E^\infty \sigma_{11,\beta}^{re(+)}(E,E') \; \phi^b(x,E')dE' \\
& + \int_{E/\alpha_\beta^*}^{E/\alpha_\beta} \sigma_{11,\beta}^{el}(E,E') \; \phi^f(x,E')dE' \qquad (2.94) \\
& + \int_E^\infty \sigma_{11,\beta}^{re(-)}(E,E') \; \phi^f(x,E')dE' \Bigg] \\
& + \eta^b(x,E)
\end{aligned}
$$

In this thesis, three different numerical solution techniques for obtaining the forward

(ϕ^f) and backward (ϕ^b) components of the low energy neutron flux as a function of

position x and energy E are investigated.

CHAPTER III

THREE SOLUTION TECHNIQUES

In this chapter three different solution methods are introduced for representing

the flux of neutrons, $\phi(E,x)$, with energy E at position x in a slab of material

$0 \leq x \leq L$. The coupled equations introduced in chapter II, describing the forward and

backward components of the low-energy isotropic neutron flux are analyzed, and the

coupling terms are approximated. The approximations ultimately lead to a decoupling

of the forward and backward components, and three solution techniques – the

Collocation method, Wilson's method, and the Fixed Point – Series method – are then

applied to the resulting non-coupled system.

The Collocation method begins by assuming that the low energy neutron flux

can be expressed as a linear combination of basis splines with support in the E

variable. The assumption leads to a system of ordinary differential equations of the

form

$$\frac{\partial \vec{\phi}}{\partial x} = A\vec{\phi} + \vec{\eta} \tag{3.1}$$

It is at this point where the current application of the Collocation method will differ

from that presented by Clowdsley [16,25,30] and Feldman [27]. Clowdsley

introduced the so called Multi-Group Technique by assuming average values of the

neutron flux over small energy regimes, and then used the Mean Value Theorem for

Integrals to approximate the matrix A appearing in equation (3.1). Conversely, Feldman calculated the A matrix using numerical integration and solved the above system using a finite difference approach. Though both methods have advantages (and yield good results), the approximations made in the Multi-Group technique were extensive, and the differencing techniques in Feldman's approach led to a heavy computational cost. Our purpose here is to both avoid any further approximations while keeping the computational cost at a minimum.

Wilson's method [11,32] begins by splitting the low-energy neutron flux into a sum of two terms referred to as the fundamental and perturbational parts. The solution for the fundamental part represents the propagation of only those neutrons produced by the high-energy forward component with no source contribution. The source of neutrons produced by the fundamental solution is calculated separately and the collocation method is then used to solve the remaining equation for the perturbational part.

The Fixed Point – Series method extends the perturbation technique used in Wilson's method. Both the forward and backward components are split into fundamental and perturbational parts and the first steps of Wilson's method are followed. The perturbational term is then further split into two terms and the process is repeated. Computationally speaking, Wilson's method and the Fixed Point – Series methods are much less efficient than the Collocation method. However, the physical insight offered by these two methods far outweighs that provided by the Collocation method, because secondary neutron production can be observed more closely.

Further, the true advantage of the latter two methods lies in their applicability to the more complicated coupled model introduced in chapter II.

NON-COUPLED NEUTRON TRANSPORT MODEL

The coupled system of equations describing the forward and backward components of the low-energy neutron flux, ϕ^f and ϕ^b was given in chapter II. In order to ease notation slightly, define the following integral operators

$$I_{(+)}^{el}[\phi] = \sum_\beta \int_E^{E/\alpha_\beta^*} \sigma_{11,\beta}^{el}(E,E')\phi(x,E')dE' \tag{3.2}$$

$$I_{(-)}^{el}[\phi] = \sum_\beta \int_{E/\alpha_\beta^*}^{E/\alpha_\alpha} \sigma_{11,\beta}^{el}(E,E')\phi(E',x)dE' \tag{3.3}$$

$$I_{(+)}^{re}[\phi] = \sum_\beta \int_E^{\infty} \sigma_{11,\beta}^{re(+)}(E,E')\phi(x,E')dE' \tag{3.4}$$

$$I_{(-)}^{re}[\phi] = \sum_\beta \int_E^{\infty} \sigma_{11,\beta}^{re(-)}(E,E')\phi(x,E')dE' \tag{3.5}$$

where the sum over β is taken to account for materials with multiple atomic species. Recall from chapter II, the (+) notation refers to secondary particles produced in the same general direction of the projectile (scattering angle $\theta \in [0,\pi/2]$), while the (−) notation refers to secondary particles produced in the opposite direction of the projectile (scattering angle $\theta \in [\pi/2,\pi]$). The coupled system of equations introduced in chapter II for $\phi^f(x,E)$ and $\phi^b(x,E)$ can now be given in operator form as

$$B_f[\phi^f] = I_{(+)}^{el}[\phi^f] + I_{(+)}^{re}[\phi^f] + I_{(-)}^{el}[\phi^b] + I_{(-)}^{re}[\phi^b] + \eta^f \tag{3.6}$$

$$B_b[\phi^b] = I^{el}_{(+)}[\phi^b] + I^{re}_{(+)}[\phi^b] + I^{el}_{(-)}[\phi^f] + I^{re}_{(-)}[\phi^f] + \eta^b \qquad (3.7)$$

Recall that the source terms $\eta^f(x,E)$ and $\eta^b(x,E)$ are secondary neutrons produced in the forward and backward directions by a high-energy primary source.

The advantage of writing the coupled system in operator form is that the physical meaning of each term can now be easily discussed. First, examine the right hand side of equation (3.6). The terms $I^{el}_{(+)}[\phi^f]$ and $I^{re}_{(+)}[\phi^f]$ represent the secondary neutrons produced through elastic and reactive processes in the forward direction by a forward flux (no change in direction). Conversely, the terms $I^{el}_{(-)}[\phi^b]$ and $I^{re}_{(-)}[\phi^b]$ represent the secondary neutrons produced through elastic and reactive processes in the forward direction by a backward flux (change in direction). Similarly, the terms $I^{el}_{(+)}[\phi^b]$ and $I^{re}_{(+)}[\phi^b]$ represent the secondary neutrons produced through elastic and reactive processes in the backward direction by a backward flux (no change in direction), and the terms $I^{el}_{(-)}[\phi^f]$ and $I^{re}_{(-)}[\phi^f]$ represent the secondary neutrons produced through elastic and reactive processes in the backward direction by a forward flux (change in direction).

The linear differential operators $B_f[\phi]$ and $B_b[\phi]$ were defined as

$$B_f[\phi] \equiv \left[\frac{\partial}{\partial x} + \sigma_1(E) \right] \phi \qquad (3.8)$$

$$B_b[\phi] \equiv \left[-\frac{\partial}{\partial x} + \sigma_1(E) \right] \phi \qquad (3.9)$$

The quantities $\frac{\partial}{\partial x}\phi^f(E,x)$ and $\frac{\partial}{\partial x}\phi^b(E,x)$ are the rates of change in the number of

forward and backward neutrons of energy E with respect to distance traveled. The

minus sign in equation (3.9) physically represents the propagation direction of the

backward component.

The total macroscopic cross section for a neutron with energy E is given by

$\sigma_1(E)$ in units of $[cm^2 / g]$. Note that the probability that a neutron with energy E

will suffer a nuclear collision in moving a distance dx is given by $\sigma_1(E)dx$, and the

terms $\sigma_1(E)\phi^f(E,x)$ or $\sigma_1(E)\phi^b(x,E)$ represent the number of neutrons (forward or

backward respectively) with energy E at depth x lost due to nuclear collisions.

In the introduction to this chapter, references were given to Feldman and

Clowdsley who have both solved neutron transport models using collocation

Techniques [16,25,27,30]. Feldman solved a coupled system very similar to that

given by equations (3.6) and (3.7), with the only difference being exclusion of nuclear

reactive processes. It is true that for low energy particles, there will be very little

fragmentation and so elastic processes will dominate. However, inclusion of the

reactive processes does not add considerable complexity (algebraically or

computationally), and so they can be added quite easily. He solved the system by

implementing a collocation technique resulting in a system of linear differential

equations. The resulting system was then solved using a finite difference scheme

leading to well over 20 hours of computational time for a single material problem [27]

(multi-material problems will be discussed in chapter IV). Conversely, Clowdsley

solved a non-coupled system by also using a collocation technique but grouped certain particles together according to their kinetic energy. The grouping allowed for simplifications and hence the computational cost was reduced. The marked difference in computational cost between the two methods though was primarily due to the complexity of the coupled system in comparison to the non-coupled system. Further, since the results given in each case did not differ greatly, it can be concluded that one can work with the non-coupled model without significant error. As such, we now proceed to decouple the system of equations given in chapter II.

The coupling term in equation (3.6) is $I_{(-)}^{el}[\phi^b] + I_{(-)}^{re}[\phi^b]$ and the coupling term in equation (3.7) is $I_{(-)}^{el}[\phi^f] + I_{(-)}^{re}[\phi^f]$; the physical interpretation of each has been given above. Their contributions will be approximated by replacing ϕ^b with ϕ^f in equation (3.6) and ϕ^f with ϕ^b in equation (3.7). These approximations are expected to be less valid near the front and back boundaries (and any interfaces between materials in a multi-layer configuration); however, far enough away from any boundaries (or interfaces), these approximations are expected to be fairly accurate. Future work will make direct comparisons between the models to see how much information is actually lost by these assumptions. The system of equations now takes the form

$$B_f[\phi^f] = I_{(+)}^{el}[\phi^f] + I_{(+)}^{re}[\phi^f] + I_{(-)}^{el}[\phi^f] + I_{(-)}^{re}[\phi^f] + \eta^f \qquad (3.10)$$

$$B_b[\phi^b] = I_{(+)}^{el}[\phi^b] + I_{(+)}^{re}[\phi^b] + I_{(-)}^{el}[\phi^b] + I_{(-)}^{re}[\phi^b] + \eta^b \qquad (3.11)$$

Further simplifications can now be made. Consider the integral source terms on the

right hand side of equation (3.10)

$$
I_{(+)}^{el}[\phi^f] + I_{(+)}^{re}[\phi^f] + I_{(-)}^{el}[\phi^f] + I_{(-)}^{re}[\phi^f]
$$

$$
= \sum_{\beta} \left[\int_E^{E/\alpha_\beta^*} \sigma_{11,\beta}^{el}(E,E')\phi^f(x,E')dE' \right.
$$

$$
+ \int_E^{\infty} \sigma_{11,\beta}^{re(+)}(E,E')\phi^f(x,E')dE' \tag{3.12}
$$

$$
+ \int_{E/\alpha_\beta^*}^{E/\alpha_\beta} \sigma_{11,\beta}^{el}(E,E')\phi^f(x,E')dE'
$$

$$
\left. + \int_E^{\infty} \sigma_{11,\beta}^{re(-)}(E,E')\phi^f(x,E')dE' \right]
$$

Recall that $\sigma_{11,\beta}^{re} = \sigma_{11,\beta}^{re(+)} + \sigma_{11,\beta}^{re(-)}$ so that equation (3.12) simplifies to

$$
I_{(+)}^{el}[\phi^f] + I_{(+)}^{re}[\phi^f] + I_{(-)}^{el}[\phi^f] + I_{(-)}^{re}[\phi^f]
$$

$$
= \sum_{\beta} \left[\begin{array}{c} \int_E^{E/\alpha_\beta} \sigma_{11,\beta}^{el}(E,E')\phi^f(x,E')dE' \\ + \int_E^{\infty} \sigma_{11,\beta}^{re}(E,E')\phi^f(x,E')dE' \end{array} \right] \tag{3.13}
$$

and the integral source terms on the right hand side of equation (3.11) become

$$
I_f^{el}[\phi^b] + I_f^{re}[\phi^b] + I_b^{el}[\phi^b] + I_b^{re}[\phi^b]
$$

$$
= \sum_{\beta} \left[\begin{array}{c} \int_E^{E/\alpha_\beta} \sigma_{11,\beta}^{el}(E,E')\phi^b(x,E')dE' \\ + \int_E^{\infty} \sigma_{11,\beta}^{re}(E,E')\phi^b(x,E')dE' \end{array} \right] \tag{3.14}
$$

Hence, the non-coupled system of equations for ϕ^f and ϕ^b is given by

$$
B_f[\phi^f] = \sum_{\beta} \left[\int_E^{E/\alpha_\beta} \sigma_{11,\beta}^{el}(E,E')\phi^f(x,E')dE' \right.
$$

$$
\left. + \int_E^{\infty} \sigma_{11,\beta}^{re}(E,E')\phi^f(x,E')dE' \right] + \eta^f(x,E') \tag{3.15}
$$

$$B_b[\phi^b] = \sum_\beta \left[\int_E^{E/\alpha_\beta} \sigma_{11,\beta}^{el}(E,E')\phi^b(x,E')dE' \right.$$

$$\left. + \int_E^\infty \sigma_{11,\beta}^{re}(E,E')\phi^b(x,E')dE' \right] + \eta^b(x,E')$$

(3.16)

Equations (3.15) and (3.16) are the non-coupled system of equations describing the

forward and backward components of the low-energy neutron flux.

COLLOCATION METHOD

We assume solutions to the non-coupled system of equations (3.15) and (3.16)

of the form

$$\hat{\phi}^f(x,E) = \sum_{j=1}^N \phi^f(x,E_j)B_j(E)$$

(3.17)

$$\hat{\phi}^b(x,E) = \sum_{j=1}^N \phi^b(x,E_j)B_j(E)$$

(3.18)

From reference [33], the functions $B_j(E)$ are linear basis splines with support

$\left[E_{j-1}, E_{j+1}\right]$. Define $B_j(E)$ as

$$B_j(E) = \begin{cases} \dfrac{E-E_{j-1}}{E_j - E_{j-1}}, & E \in \left[E_{j-1}, E_j\right] \\[2ex] \dfrac{E_{j+1}-E}{E_{j+1}-E_j}, & E \in \left[E_j, E_{j+1}\right] \\[2ex] 0 & , \; otherwise \end{cases}$$

(3.19)

Note that $B_j(E_i) = \delta_{ij}$ (δ_{ij} is the Kronecker delta) and $B_j(E) = 0$ for all $E \leq E_{j-1}$ and

$E \geq E_{j+1}$ as illustrated in fig. 13.
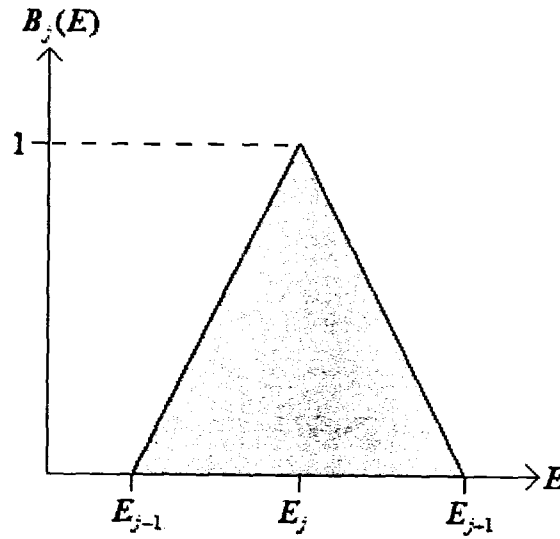
Fig. 13. Linear B-Spline.

Substitution of equations (3.17) and (3.18) into equations (3.15) and (3.16) respectively yields

$$\sum_{j=1}^{N}\frac{\partial}{\partial x}\phi^{f}(x,E_{j})B_{j}(E)+\sigma_{1}(E)\sum_{j=1}^{N}\phi^{f}(x,E_{j})B_{j}(E)$$

$$=\sum_{j=1}^{N}\phi^{f}(x,E_{j})\sum_{\beta}\left(\begin{array}{c}\int_{E}^{\infty}\sigma_{11,\beta}^{re}(E,E')B_{j}(E')dE'\\[2mm]+\int_{E}^{E/\alpha_{\beta}}\sigma_{11,\beta}^{el}(E,E')B_{j}(E')dE'\end{array}\right)+\eta^{f}(x,E)\qquad(3.20)$$

$$-\sum_{j=1}^{N}\frac{\partial}{\partial x}\phi^{b}(x,E_{j})B_{j}(E)+\sigma_{1}(E)\sum_{j=1}^{N}\phi^{b}(x,E_{j})B_{j}(E)$$

$$=\sum_{j=1}^{N}\phi^{b}(x,E_{j})\sum_{\beta}\left(\begin{array}{c}\int_{E}^{\infty}\sigma_{11,\beta}^{re}(E,E')B_{j}(E')dE'\\[2mm]+\int_{E}^{E/\alpha_{\beta}}\sigma_{11,\beta}^{el}(E,E')B_{j}(E')dE'\end{array}\right)+\eta^{b}(x,E)\qquad(3.21)$$

Evaluate equations (3.20) and (3.21) at E_i for $i=1,2,...,N$, and obtain

$$\frac{\partial}{\partial x}\phi^f(x,E_i) = -\sigma_1(E_i)\phi^f(x,E_i)$$

$$= \sum_{j=1}^{N}\phi^f(x,E_j)\sum_{\beta}\left(\begin{array}{l}\int_{E_i}^{\infty}\sigma_{11,\beta}^{re}(E_i,E')B_j(E')dE'\\ + \int_{E_i}^{E_i/\alpha_\beta}\sigma_{11,\beta}^{el}(E_i,E')B_j(E')dE'\end{array}\right) + \eta^f(x,E_i) \tag{3.22}$$

$$-\frac{\partial}{\partial x}\phi^b(x,E_i) = -\sigma_1(E_i)\phi^b(x,E_i)$$

$$+ \sum_{j=1}^{N}\phi^b(x,E_j)\sum_{\beta}\left(\begin{array}{l}\int_{E_i}^{\infty}\sigma_{11,\beta}^{re}(E_i,E')B_j(E')dE'\\ + \int_{E_i}^{E_i/\alpha_\beta}\sigma_{11,\beta}^{el}(E_i,E')B_j(E')dE'\end{array}\right) + \eta^b(x,E_i) \tag{3.23}$$

Define the matrix $A = \left(a_{ij}\right)$ with components

$$a_{ij} = -\sigma_1(E_i)B_j(E_i) + \sum_{\beta}\left(\begin{array}{l}\int_{E_i}^{\infty}\sigma_{11,\beta}^{re}(E_i,E')B_j(E')dE'\\ + \int_{E_i}^{E_i/\alpha_\beta}\sigma_{11,\beta}^{el}(E_i,E')B_j(E')dE'\end{array}\right) \tag{3.24}$$

The equations (3.22) and (3.23) can then be written in the form

$$\frac{\partial}{\partial x}\phi^f(x,E_i) = \sum_{j=1}^{N}a_{ij}\phi^f(x,E_j) + \eta^f(x,E_i) \tag{3.25}$$

$$-\frac{\partial}{\partial x}\phi^b(x,E_i) = \sum_{j=1}^{N}a_{ij}\phi^b(x,E_j) + \eta^b(x,E_i) \tag{3.26}$$

Before proceeding to solve equations (3.25) and (3.26), some simplifications to the A-matrix will be helpful. Let

$$a_{ij} = a_{ij}^{(1)} + a_{ij}^{(2)} + a_{ij}^{(3)} \tag{3.27}$$

with

$$a_{ij}^{(1)} = -\sigma_1(E_i)B_j(E_i) \tag{3.28}$$

$$a_{ij}^{(2)} = \sum_{\beta} \int_{E_i}^{\infty} \sigma_{11,\beta}^{re}(E_i, E')B_j(E')dE'$$

(3.29)

$$a_{ij}^{(3)} = \sum_{\beta} \int_{E_i}^{E_i/\alpha_\beta} \sigma_{11,\beta}^{el}(E_i, E')B_j(E')dE'$$

(3.30)

First note that $B_j(E_i) = 0$ for all $i \neq j$ and so $a_{ij}^{(1)}$ is a diagonal matrix of the form

$$a_{ij}^{(1)} = \begin{pmatrix} -\sigma_1(E_1) & 0 & \cdots & 0 \\ 0 & \ddots & \ddots & \vdots \\ \vdots & \ddots & \ddots & 0 \\ 0 & \cdots & 0 & -\sigma_1(E_N) \end{pmatrix}$$

(3.31)

The production cross-sections $\sigma_{11,\beta}^{el}(E,E')$ and $\sigma_{11,\beta}^{re}(E,E')$ are both zero for $E' < E$

(the projectile energy must always be greater than that of the fragment). Also,

$B_j(E) = 0$ for all $E \geq E_{j+1}$ and so $a_{ij}^{(2)}$ and $a_{ij}^{(3)}$ are upper triangular matrices and take

the simplified forms

$$a_{ij}^{(2)} = \sum_{\beta} \int_{E_a}^{E_{j+1}} \sigma_{11,\beta}^{re}(E_i, E')B_j(E')dE'$$

(3.32)

$$a_{ij}^{(3)} = \sum_{\beta} \int_{E_a}^{E_\beta} \sigma_{11,\beta}^{el}(E_i, E')B_j(E')dE'$$

(3.33)

where $E_\beta = \min\{E_{j+1}, E_i/\alpha_\beta\}$ and $E_a = \max\{E_i, E_{j-1}\}$. Clearly, the A-matrix must be

upper-triangular and so our systems of differential equations can be written as

$$\frac{\partial}{\partial x}\begin{bmatrix} \phi^f(x, E_1) \\ \phi^f(x, E_2) \\ \vdots \\ \phi^f(x, E_N) \end{bmatrix} = \begin{bmatrix} a_{11} & a_{12} & \cdots & a_{1N} \\ 0 & a_{22} & & \vdots \\ \vdots & \ddots & \ddots & \vdots \\ 0 & \cdots & 0 & a_{NN} \end{bmatrix}\begin{bmatrix} \phi^f(x, E_1) \\ \phi^f(x, E_2) \\ \vdots \\ \phi^f(x, E_N) \end{bmatrix} + \begin{bmatrix} \eta^f(x, E_1) \\ \eta^f(x, E_2) \\ \vdots \\ \eta^f(x, E_N) \end{bmatrix}$$

(3.34)

$$-\frac{\partial}{\partial x}\begin{bmatrix} \phi^b(x,E_1) \\ \phi^b(x,E_2) \\ \vdots \\ \phi^b(x,E_N) \end{bmatrix} = \begin{bmatrix} a_{11} & a_{12} & \cdots & a_{1N} \\ 0 & a_{22} & & \vdots \\ \vdots & \ddots & \ddots & \vdots \\ 0 & \cdots & 0 & a_{NN} \end{bmatrix}\begin{bmatrix} \phi^b(x,E_1) \\ \phi^b(x,E_2) \\ \vdots \\ \phi^b(x,E_N) \end{bmatrix} + \begin{bmatrix} \eta^b(x,E_1) \\ \eta^b(x,E_2) \\ \vdots \\ \eta^b(x,E_N) \end{bmatrix} \tag{3.35}$$

In order to solve the above systems, we begin by examining the equations for

$\phi^f(x,E_N)$ and $\phi^b(x,E_N)$ obtained from the last row of the matrix equations (3.34)

and (3.35).

$$\frac{\partial}{\partial x}\phi^f(x,E_N) = a_{NN}\phi^f(x,E_N) + \eta^f(x,E_N) \tag{3.36}$$

$$-\frac{\partial}{\partial x}\phi^b(x,E_N) = a_{NN}\phi^b(x,E_N) + \eta^b(x,E_N) \tag{3.37}$$

Upon rearrangement of terms and introduction of an integrating factor, equation (3.36)

can be solved exactly as follows

$$\frac{\partial}{\partial x}\phi^f(x,E_N) - a_{NN}\phi^f(x,E_N) = \eta^f(x,E_N) \tag{3.38}$$

$$\frac{\partial}{\partial x}\left[e^{-a_{NN}x}\phi^f(x,E_N)\right] = e^{-a_{NN}x}\eta^f(x,E_N) \tag{3.39}$$

Note the boundary condition $\phi^f(0,E) = 0$ and integrate to obtain

$$\int_0^x \frac{\partial}{\partial x'}\left[e^{-a_{NN}x'}\phi^f(x',E_N)\right]dx' = \int_0^x e^{-a_{NN}x'}\eta^f(x',E_N)dx' \tag{3.40}$$

so that the fundamental solution is

$$\phi^f(x,E_N) = \int_0^x e^{a_{NN}(x-x')}\eta^f(x',E_N)dx' \tag{3.41}$$

Equation (3.37) is solved in a similar manner with a slight deviation to account for the boundary condition. Note that

$$-\frac{\partial}{\partial x}\phi^b(x,E_N)-a_{NN}\phi^b(x,E_N)=\eta^b(x,E_N)$$

(3.42)

$$\frac{\partial}{\partial x}\left[e^{a_{NN}x}\phi^b(x,E_N)\right]=-e^{a_{NN}x}\eta^b(x,E_N)$$

(3.43)

The boundary condition for ϕ^b is specified as $\phi^b(L,E)=0$ and so integration over the interval $[x,L]$ yields

$$\int_x^L\frac{\partial}{\partial x'}\left[e^{a_{NN}x'}\phi^b(x',E_N)\right]dx'=-\int_x^L e^{a_{NN}x'}\eta^b(x,'E_N)dx'$$

(3.44)

$$\phi^b(x,E_N)=\int_x^L e^{-a_{NN}(x-x')}\eta^b(x',E_N)dx'$$

(3.45)

Now examine the equations for $\phi^f(x,E_{N-1})$ and $\phi^b(x,E_{N-1})$ from the $N-1^{st}$ row of the matrix equations (3.34) and (3.35)

$$\frac{\partial}{\partial x}\phi^f(x,E_{N-1})=a_{N-1,N-1}\phi^f(x,E_{N-1})+a_{N-1,N}\phi^f(x,E_N)+\eta^f(x,E_{N-1})$$

(3.46)

$$-\frac{\partial}{\partial x}\phi^b(x,E_{N-1})=a_{N-1,N-1}\phi^b(x,E_{N-1})+a_{N-1,N}\phi^b(x,E_N)+\eta^b(x,E_{N-1})$$

(3.47)

The terms $\phi^f(x,E_N)$ and $\phi^b(x,E_N)$ are now known and can be considered as source terms remaining on the right hand side. Hence, by using similar integrating factors as before, the exact solutions to equations (3.46) and (3.47) will be given by

$$\phi^f(x,E_{N-1})=\int_0^x e^{a_{N-1,N-1}(x-x')}\left[\eta^f(x',E_{N-1})+a_{N-1,N}\phi^f(x',E_N)\right]dx'$$

(3.48)

$$\phi^b(x,E_{N-1})=\int_x^L e^{-a_{N-1,N-1}(x-x')}\left[\eta^b(x',E_{N-1})+a_{N-1,N}\phi^b(x',E_N)\right]dx'$$

(3.49)

Continuing the back substitution of previously known solutions into the next lower

row of the A-matrix representation, one obtains the solutions for $\phi^f(x, E_{N-j})$ and

$\phi^b(x, E_{N-j})$ for $(j = 1, 2, ..., N-1)$ as

$$\phi^f(x, E_{N-j}) = \int_0^x e^{a_{N-j,N-j}(x-x')} \left[\begin{array}{l} \eta^f(x', E_{N-j}) \\ + \sum_{k=0}^{j-1} a_{N-j,N-k} \phi^f(x', E_{N-k}) \end{array} \right] dx' \qquad (3.50)$$

$$\phi^b(x, E_{N-j}) = \int_x^L e^{-a_{N-j,N-j}(x-x')} \left[\begin{array}{l} \eta^b(x', E_{N-j}) \\ + \sum_{k=0}^{j-1} a_{N-j,N-k} \phi^b(x', E_{N-k}) \end{array} \right] dx' \qquad (3.51)$$

The solution for $E = E_N$ is given by equations (3.41) and (3.45). The solutions (3.41),

(3.45), (3.48) and (3.49) can be written in the compact form

$$\phi^f(x, E_{N-j}) = \int_0^x e^{a_{N-j,N-j}(x-x')} \left[\eta^f(x', E_{N-j}) \right.$$
$$\left. + (1 - \delta_{j0}) \cdot \sum_{k=0}^{j-1} a_{N-j,N-k} \phi^f(x', E_{N-k}) \right] dx' \qquad (3.52)$$

$$\phi^b(x, E_{N-j}) = \int_x^L e^{-a_{N-j,N-j}(x-x')} \left[\eta^b(x', E_{N-j}) \right.$$
$$\left. + (1 - \delta_{j0}) \cdot \sum_{k=0}^{j-1} a_{N-j,N-k} \phi^b(x', E_{N-k}) \right] dx' \qquad (3.53)$$

for $j = 0, 1, ..., N-1$, where δ is the Kronecker delta.

WILSON'S METHOD

Following references [11] and [32], let the forward and backward components

of flux have the following forms

$$\phi^f = \phi_0^f + \phi_1^f \qquad (3.54)$$

$$\phi^b = \phi_0^b + \phi_1^b \tag{3.55}$$

Substitution of equations (3.54) and (3.55) into the non-coupled system (3.15) and (3.16) yields

$$
\begin{aligned}
B_f\left[\phi_0^f\right] + B_f\left[\phi_1^f\right] &= \sum_\beta \int_E^\infty \sigma_{11,\beta}^{re}\left(\phi_0^f + \phi_1^f\right) dE' \\
&+ \sum_\beta \int_E^{E/\alpha_\beta} \sigma_{11,\beta}^{el}\left(\phi_0^f + \phi_1^f\right) dE' + \eta^f(x,E)
\end{aligned}
\tag{3.56}
$$

$$
\begin{aligned}
B_b\left[\phi_0^b\right] + B_b\left[\phi_1^b\right] &= \sum_\beta \int_E^\infty \sigma_{11,\beta}^{re}\left(\phi_0^b + \phi_1^b\right) dE' \\
&+ \sum_\beta \int_E^{E/\alpha_\beta} \sigma_{11,\beta}^{el}\left(\phi_0^b + \phi_1^b\right) dE' + \eta^b(x,E)
\end{aligned}
\tag{3.57}
$$

Define the fundamental solutions ϕ_0^f and ϕ_0^b to be solutions of the differential equations

$$B_f\left[\phi_0^f\right] = \eta^f \tag{3.58}$$

$$B_b\left[\phi_0^b\right] = \eta^b \tag{3.59}$$

with boundary conditions $\phi_0^f(0,E) = 0$, $\phi_0^b(L,E) = 0$. The equation (3.58) can be written in the expanded from

$$\frac{\partial}{\partial x}\phi_0^f(x,E) + \sigma_1(E)\phi_0^f(x,E) = \eta^f(x,E) \tag{3.60}$$

Upon introduction of an integrating factor, one can write

$$\frac{\partial}{\partial x}\left[e^{\sigma_1(E)x}\phi_0^f(x,E)\right] = e^{\sigma_1(E)x}\eta^f(x,E) \tag{3.61}$$

Apply integration over the interval $[0,x]$ so that

$$\int_0^x \frac{\partial}{\partial x'}\left[e^{\sigma_1(E)x'}\phi_0^f(x',E)\right]dx' = \int_0^x e^{\sigma_1(E)x'}\eta^f(x',E)\,dx' \qquad (3.62)$$

which yields the solution for ϕ_0^f as

$$\phi_0^f(x,E) = \int_0^x e^{-\sigma_1(E)(x-x')}\eta^f(x',E)\,dx' \qquad (3.63)$$

Similarly, the equation (3.59) can be solved to obtain

$$-\frac{\partial}{\partial x}\phi_0^b(x,E) + \sigma_1(E)\phi_0^b(x,E) = \eta^b(x,E) \qquad (3.64)$$

$$\frac{\partial}{\partial x}\left[e^{-\sigma_1(E)x}\phi_0^b(x,E)\right] = -e^{-\sigma_1(E)x}\eta^b(x,E) \qquad (3.65)$$

$$\int_x^L \frac{\partial}{\partial x}\left[e^{-\sigma_1(E)x'}\phi_0^b(x',E)\right]dx' = -\int_x^L e^{-\sigma_1(E)x'}\eta^b(x',E)\,dx' \qquad (3.66)$$

with the fundamental solution

$$\phi_0^b(x,E) = \int_x^L e^{\sigma_1(E)(x-x')}\eta^b(x',E)\,dx' \qquad (3.67)$$

The forward and backward fundamental solutions represent the propagation of the first generation secondary neutrons produced by the high-energy straight-ahead solution. The equations (3.56) and (3.57) are now reduced to the form

$$B_f\left[\phi_1^f\right] = \sum_\beta \int_E^\infty \sigma_{11,\beta}^{re}\,\phi_1^f\,dE'$$
$$+\sum_\beta \int_E^{E/\alpha_\beta} \sigma_{11,\beta}^{el}\,\phi_1^f\,dE' + \xi_0^f(x,E) \qquad (3.68)$$

$$B_b\left[\phi_1^b\right] = \sum_\beta \int_E^\infty \sigma_{11,\beta}^{re}\,\phi_1^b\,dE'$$
$$+\sum_\beta \int_E^{E/\alpha_\beta} \sigma_{11,\beta}^{el}\,\phi_1^b\,dE' + \xi_0^b(x,E) \qquad (3.69)$$

with boundary conditions $\phi_1^f(E,0) = 0$, $\phi_1^b(E,L) = 0$, where

$$\xi_0^f(x,E) = \sum_\beta \int_E^\infty \sigma_{11,\beta}^{re} \phi_0^f dE' + \sum_\beta \int_E^{E/\alpha_\beta} \sigma_{11,\beta}^{el} \phi_0^f dE' \qquad (3.70)$$

$$\xi_0^b(x,E) = \sum_\beta \int_E^\infty \sigma_{11,\beta}^{re} \phi_0^b dE' + \sum_\beta \int_E^{E/\alpha_\beta} \sigma_{11,\beta}^{el} \phi_0^b dE' \qquad (3.71)$$

The solutions to equations (3.68) and (3.69) will be referred to as the perturbational

solutions. The source terms $\xi_0^f(x,E)$, $\xi_0^b(x,E)$ are the neutrons produced in the

forward and backward directions by the first generation secondaries. After $\xi_0^f(x,E)$

and $\xi_0^b(x,E)$ are calculated, it is clear that equations (3.68) and (3.69) are identical in

form to the original system given by (3.15) and (3.16) but with different source terms.

Hence, the collocation method described in the last section can be applied to solve for

the perturbational terms.

The true usefulness of Wilson's method will be seen when it is applied to the

coupled system of equations (3.6) and (3.7) previously discussed. Recall that some

modeling assumptions were made initially in order to decouple the system of

equations for the forward and backward components of the neutron flux. If one were

to leave the system as is, the above method could be used to maintain the coupling

through the fundamental solutions and their subsequent source terms. Though this

was not numerically simulated, a discussion will be given in the last section of this

chapter.

FIXED POINT – SERIES METHOD

In order to simplify notation, it will be necessary to let

$$f(x,E) = \phi^f(x,E) \qquad (3.72)$$

$$b(x,E) = \phi^b(x,E) \tag{3.73}$$

denote the forward and backward flux terms respectively. As in the previous method, split the forward and backward flux into a fundamental and perturbational component and write

$$f = f_0^{(1)} + f_1^{(1)} \tag{3.74}$$

$$b = b_0^{(1)} + b_1^{(1)} \tag{3.75}$$

where the subscripts $0,1$ refer to the fundamental and perturbational terms respectively, and the superscript (1) refers to the first iteration in this method. Substitute equations (3.72)-(3.75) into the system of equations (3.15) and (3.16) to obtain

$$\begin{aligned} B_f\left[f_0^{(1)}\right] + B_f\left[f_1^{(1)}\right] &= \sum_\beta \int_E^\infty \sigma_{11,\beta}^{re}\left(f_0^{(1)} + f_1^{(1)}\right) dE' \\ &+ \sum_\beta \int_E^{E/\alpha_\beta} \sigma_{11,\beta}^{el}\left(f_0^{(1)} + f_1^{(1)}\right) dE' + \eta^f(x,E) \end{aligned} \tag{3.76}$$

and

$$\begin{aligned} B_b\left[b_0^{(1)}\right] + B_b\left[b_1^{(1)}\right] &= \sum_\beta \int_E^\infty \sigma_{11,\beta}^{re}\left(b_0^{(1)} + b_1^{(1)}\right) dE' \\ &+ \sum_\beta \int_E^{E/\alpha_\beta} \sigma_{11,\beta}^{el}\left(b_0^{(1)} + b_1^{(1)}\right) dE' + \eta^b(x,E) \end{aligned} \tag{3.77}$$

Assume the fundamental components $f_0^{(0)}$ and $b_0^{(0)}$ satisfy

$$B_f\left[f_0^{(1)}\right] = \eta^f \tag{3.78}$$

$$B_b\left[b_0^{(1)}\right] = \eta^b \tag{3.79}$$

with boundary conditions $f_0^{(1)}(0, E) = 0$ and $b_0^{(1)}(L, E) = 0$, and solve these equations

using exactly the same technique used previously to obtain the fundamental terms in

Wilson's method. The solutions are found to be

$$f_0^{(1)}(x, E) = \int_0^x e^{-\sigma_1(E)(x-x')}\eta^f(x', E)\,dx' \qquad (3.80)$$

$$b_0^{(1)}(x, E) = \int_x^L e^{\sigma_1(E)(x-x')}\eta^b(x', E)\,dx' \qquad (3.81)$$

The fundamental solutions are then used to calculate the new source terms

$$\eta_1^f(x, E) = \sum_\beta \int_E^\infty \sigma_{11,\beta}^{re} f_0^{(1)}\,dE' + \sum_\beta \int_E^{E/\alpha_\beta} \sigma_{11,\beta}^{el} f_0^{(1)}\,dE' \qquad (3.82)$$

$$\eta_1^b(x, E) = \sum_\beta \int_E^\infty \sigma_{11,\beta}^{re} b_0^{(1)}\,dE' + \sum_\beta \int_E^{E/\alpha_\beta} \sigma_{11,\beta}^{el} b_0^{(1)}\,dE' \qquad (3.83)$$

so that equations (3.76), (3.77) become

$$B_f\left[f_1^{(1)}\right] = \sum_\beta \int_E^\infty \sigma_{11,\beta}^{re} f_1^{(1)}\,dE'$$
$$+ \sum_\beta \int_E^{E/\alpha_\beta} \sigma_{11,\beta}^{el} f_1^{(1)}\,dE' + \eta_1^f(x, E) \qquad (3.84)$$

and

$$B_b\left[b_1^{(1)}\right] = \sum_\beta \int_E^\infty \sigma_{11,\beta}^{re} b_1^{(1)}\,dE'$$
$$+ \sum_\beta \int_E^{E/\alpha_\beta} \sigma_{11,\beta}^{el} b_1^{(1)}\,dE' + \eta_1^b(x, E) \qquad (3.85)$$

Thus far, the first steps in Wilson's method have been followed identically; the

physical interpretation at this point is the same as well. The fundamental solutions

$f_0^{(1)}$, $b_0^{(1)}$ represent the propagation of first generation secondary neutrons produced by

the high-energy straight-ahead solution, and the source terms $\eta_1^f(x, E)$, $\eta_1^b(x, E)$ are

the secondary neutrons produced by the forward and backward fundamental solutions respectively. The departure taken from Wilson's method is to repeat the perturbation step instead of applying the Collocation method. Let

$$f_1^{(1)} = f_0^{(2)} + f_1^{(2)} \tag{3.86}$$

$$b_1^{(1)} = b_0^{(2)} + b_1^{(2)} \tag{3.87}$$

and substitute these equations into (3.84), (3.85). Now assume that $f_0^{(2)}$, $b_0^{(2)}$ satisfy

$$B_f \left[f_0^{(2)} \right] = \eta_1^f \tag{3.88}$$

$$B_b \left[b_0^{(2)} \right] = \eta_1^b \tag{3.89}$$

and solve these equations as before. The solutions will be given by

$$f_0^{(2)}(x,E) = \int_0^x e^{-\sigma_1(E)(x-x')} \eta_1^f(x',E)\,dx' \tag{3.90}$$

$$b_0^{(2)}(x,E) = \int_x^L e^{\sigma_1(E)(x-x')} \eta_1^b(x',E)\,dx' \tag{3.91}$$

Again calculate the source terms

$$\eta_2^f(x,E) = \sum_\beta \int_E^\infty \sigma_{11,\beta}^{re} f_0^{(2)}\,dE' + \sum_\beta \int_E^{E/\alpha_\beta} \sigma_{11,\beta}^{el} f_0^{(2)}\,dE' \tag{3.92}$$

$$\eta_2^b(x,E) = \sum_\beta \int_E^\infty \sigma_{11,\beta}^{re} b_0^{(2)}\,dE' + \sum_\beta \int_E^{E/\alpha_\beta} \sigma_{11,\beta}^{el} b_0^{(2)}\,dE' \tag{3.93}$$

and one is left with the equations

$$B_f \left[f_1^{(2)} \right] = \sum_\beta \int_E^\infty \sigma_{11,\beta}^{re} f_1^{(2)}\,dE'$$

$$+ \sum_\beta \int_E^{E/\alpha_\beta} \sigma_{11,\beta}^{el} f_1^{(2)}\,dE' + \eta_2^f(x,E) \tag{3.94}$$

$$B_b\left[b_1^{(2)}\right] = \sum_\beta \int_E^\infty \sigma_{11,\beta}^{re} \, b_1^{(2)} dE'$$

$$+ \sum_\beta \int_E^{E/\alpha_\beta} \sigma_{11,\beta}^{el} \, b_1^{(2)} dE' + \eta_2^b(x,E) \tag{3.95}$$

Note that we are again left with the exact same system of integro-differential equations as before with just a different set of source terms. To continue, let

$$f_1^{(2)} = f_0^{(3)} + f_1^{(3)} \tag{3.96}$$

$$b_1^{(2)} = b_0^{(3)} + b_1^{(3)} \tag{3.97}$$

and then follow through the same process outlined above.

The final solutions for the forward and backward components would then be given by

$$\phi^f = \sum_{k=1} f_0^{(k)} \tag{3.98}$$

$$\phi^b = \sum_{k=1} b_0^{(k)} \tag{3.99}$$

In theory, the sums appearing in (3.98) and (3.99) should be taken with an infinite number of terms, provided the two series converge. The issue of convergence will not be dealt with theoretically in this work, but one expects from physical grounds that the series should indeed do so. Further, despite the numerical summary given above, not much has been said about the physical interpretation of the Fixed Point – Series method.

One begins with a primary source of particles η_k; the equation to be solved for the fundamental solution describes pure propagation of said primary source with no contribution from secondary neutron production. Instead, the secondary particle

production due to $\phi_0^{(k+1)}$ is accounted for in the source calculation yielding η_{k+1}. The

perturbation process is repeated and the scheme starts over with η_{k+1} viewed as the

new primary source. A visual summary is provided below in fig. 14.

Perturbation

$$\phi_1^{(k)} = \phi_0^{(k+1)} + \phi_1^{(k+1)}$$

k=k+1

Re-write
equations

**Fundamental
Solution**

$$B\left[\phi_0^{(k+1)}\right] = \eta_k$$

Source Calculation

$$\eta_{k+1} = \sum_\beta \int_E^\infty \sigma_{11,\beta}^{re} \phi_0^{(k+1)} dE' + \sum_\beta \int_E^{E/\alpha_\beta} \sigma_{11,\beta}^{el} \phi_0^{(k+1)} dE'$$
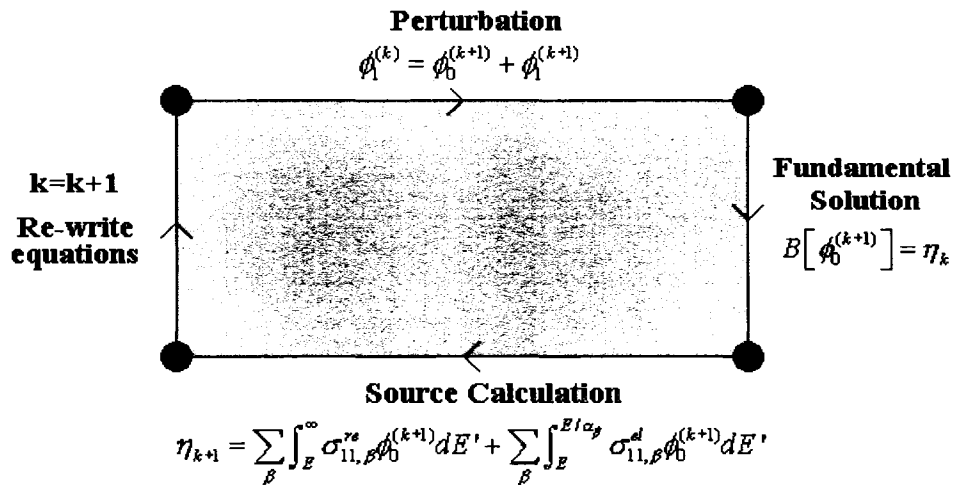
Fig. 14. Flow chart of Fixed Point - Series method.

Since elastic processes dominate low energy neutron propagation [6,30],

physical interpretation of such a scheme is really a matter of considering the

redistribution of energy through a series of such collisions. For a particular iteration,

one is propagating secondary neutrons produced by the previous iteration; hence, the

spectrum should be decreasing in magnitude as a function of iteration number.

Numerically speaking, this is exactly what is observed. In the extremely low energy

range (<10 MeV), one will see an initial spectral increase through the first few

iterations as low energy neutrons are deposited from higher energy projectiles.

However, at some iteration a maximum will be reached followed by a steady decline

until convergence is met. The maximum followed by decline is due to the loss of high-energy particles through several iterations.

Finally, it is clear that each of the three methods provides unique physical insight into the problem of low energy neutron transport. While each of the techniques is certainly distinct, they are also certainly related as seen in fig. 15.

Collocation   **Wilson's**   **Fixed Point - Series**

Pure Collocation   Perturbation with   Pure Perturbation
                      Collocation
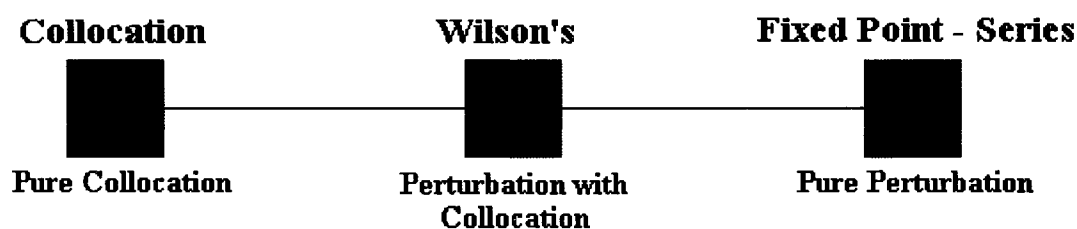
Fig. 15. Collocation method, Wilson's method, Fixed Point – Series method.

The true advantage of Wilson's method and the Fixed Point – Series method will be seen in their application to the fully coupled system.

APPLICATION TO COUPLED SYSTEM

The Collocation method presented here is by far the most computationally efficient of the three methods when dealing with the non-coupled system. The true purpose of Wilson's method and the Fixed Point – Series method was not only to validate the more recent version of the Collocation method, but also to provide indication of their applicability to the coupled system. That is, if one does not see convergence with the Fixed Point – Series method when applied to the non-coupled system, it would be futile to try such a technique on the more complicated coupled system. A brief discussion how to apply Wilson's method to the coupled system will

now be given. Though the Fixed Point – Series method would be applied in a very similar manner, it will be left out here as the application of both methods to the coupled model are topics of future work.

Consider the coupled system previously developed in chapter II and given by

$$B_f\left[\phi^f\right] = \int_E \left(\sigma_{11}^{el(+)} + \sigma_{11}^{re(+)}\right)\phi^f dE'$$
$$+ \int_E \left(\sigma_{11}^{el(-)} + \sigma_{11}^{re(-)}\right)\phi^b dE' + \eta^f(x,E) \tag{3.100}$$

$$B_b\left[\phi^b\right] = \int_E \left(\sigma_{11}^{el(+)} + \sigma_{11}^{re(+)}\right)\phi^b dE'$$
$$+ \int_E \left(\sigma_{11}^{el(-)} + \sigma_{11}^{re(-)}\right)\phi^f dE' + \eta^b(x,E) \tag{3.101}$$

As before, we assume the solution has a fundamental and perturbational part

$$\phi^f = \phi_0^f + \phi_1^f \tag{3.102}$$

$$\phi^b = \phi_0^b + \phi_1^b \tag{3.103}$$

Equations (3.102) and (3.103) are inserted into the coupled system yielding

$$B_f\left[\phi_0^f\right] + B_f\left[\phi_1^f\right] = \int_E \left(\sigma_{11}^{el(+)} + \sigma_{11}^{re(+)}\right)\left(\phi_0^f + \phi_1^f\right) dE'$$
$$+ \int_E \left(\sigma_{11}^{el(-)} + \sigma_{11}^{re(-)}\right)\left(\phi_0^b + \phi_1^b\right) dE' + \eta^f(x,E) \tag{3.104}$$

$$B_b\left[\phi_0^b\right] + B_b\left[\phi_1^b\right] = \int_E \left(\sigma_{11}^{el(+)} + \sigma_{11}^{re(+)}\right)\left(\phi_0^b + \phi_1^b\right) dE'$$
$$+ \int_E \left(\sigma_{11}^{el(-)} + \sigma_{11}^{re(-)}\right)\left(\phi_0^f + \phi_1^f\right) dE' + \eta^b(x,E) \tag{3.105}$$

Note that we assume ϕ_0^f, ϕ_0^b satisfy the linear differential equations

$$B_f\left[\phi_0^f\right] = \eta^f \tag{3.106}$$

$$B_b\left[\phi_0^b\right] = \eta^b \tag{3.107}$$

One can then calculate the source terms

$$\eta_0^{ff} = \int_E \left(\sigma_{11}^{el(+)} + \sigma_{11}^{re(+)} \right) \phi_0^f \, dE' \tag{3.108}$$

$$\eta_0^{bb} = \int_E \left(\sigma_{11}^{el(+)} + \sigma_{11}^{re(+)} \right) \phi_0^b \, dE' \tag{3.109}$$

$$\eta_0^{fb} = \int_E \left(\sigma_{11}^{el(-)} + \sigma_{11}^{re(-)} \right) \phi_0^b \, dE' \tag{3.110}$$

$$\eta_0^{bf} = \int_{E'} \left(\sigma_{11}^{el(-)} + \sigma_{11}^{re(-)} \right) \phi_0^f \, dE' \tag{3.111}$$

where η_0^{ff} represents a forward source due to a forward flux, η_0^{bb} represents a

backward source due to a backward flux, η_0^{fb} represents a forward source due to a

backward flux, and η_0^{bf} represents a backward source due to a forward flux. The

equations (3.104) and (3.105) now reduce to

$$B_f \left[\phi_1^f \right] = \int_E \left(\sigma_{11}^{el(+)} + \sigma_{11}^{re(+)} \right) \phi_1^f \, dE'$$
$$+ \int_E \left(\sigma_{11}^{el(-)} + \sigma_{11}^{re(-)} \right) \phi_1^b \, dE' + \eta_0^{ff}(E, x) + \eta_0^{fb}(x, E) \tag{3.112}$$

$$B_b \left[\phi_1^b \right] = \int_E \left(\sigma_{11}^{el(+)} + \sigma_{11}^{re(+)} \right) \phi_1^b \, dE'$$
$$+ \int_E \left(\sigma_{11}^{el(-)} + \sigma_{11}^{re(-)} \right) \phi_1^f \, dE' + \eta_0^{bf}(E, x) + \eta_0^{bb}(x, E) \tag{3.113}$$

One would then proceed with the same modeling assumptions used in the introduction

to decouple these equations, and ultimately the Collocation method should be used to

solve the resulting non-coupled system.

The advantage to such a scheme over what has previously been done is that the

coupling has now been approximated to a first order term. Of course, if one were to

apply the Fixed Point – Series method to this, the coupling would be fully accounted

for, but the computational cost would be extensive.

CHAPTER IV

MULTI-LAYER CONFIGURATIONS

HZETRN-05 is setup to calculate the flux of charged and neutral particles in a maximum of three different layers of material. The table of flux values produced is then used to approximate three-dimensional geometries of spacecraft, instrumentation and biological systems by employing ray trace algorithms and interpolation routines. In fact, certain versions of HZETRN have been generalized to N layers of material so that more complicated geometries can be simulated. As such, the three methods given in chapter III will be further developed for two and three layer configurations. It will be obvious at the end of the discussion that a generalization to N layers of material is trivial.

One of the stated advantages of deterministic methods is the reduced computational cost in the simulation of particle transport even in multi-layer configurations. As such, computational efficiency was a primary concern when the methods were evaluated numerically. From chapter III it is clear that all of the methods rely almost entirely on numerical integration; therefore, great care was taken to ensure that the same level of accuracy was used for each integral for two reasons. First, this level of consistency ensures that any major differences in the results given by the methods cannot be attributed to numerical error, and second, the number of integrals calculated by a specific method may then be used to indicate the computational cost it presents.

In this chapter the specific numerical techniques used in the three methods will be given, and the computational cost of each method will be summarized in terms of integral calculations. An introduction of multi-layer configurations will be given, followed by a discussion of how to apply the methods in a multi-layer setup.

NUMERICAL CONSIDERATIONS

All of the integrals to be calculated in the three methods can be expressed in the form

$$I = \int_a^b f_1(z) \cdot f_2(z) \, dz \tag{4.1}$$

where $f_1(z)$ can be computed exactly for any z and $f_2(z)$ is given as an array of numerical values where interpolation is used to generate numbers not found in the array. The variable z is used here as a dummy variable since integrations were taken over both energy (E) and depth (x) in all of the methods. In order to be consistent, all integrals were computed using a 5th order Gaussian quadrature along with 2nd order Lagrangian interpolation [33]; grid-refinement schemes were also used in order to improve accuracy. The integral I in equation (4.1) can be written as

$$I = \sum_{i=1}^{\alpha-1} \int_{z_i}^{z_{i+1}} f_1(z) \cdot f_2(z) \, dz \tag{4.2}$$

where $z_1 = a$, $z_\alpha = b$, $\alpha = (b-a)/\Delta z$ and $\Delta z = z_{i+1} - z_i$. To ensure that each integral was evaluated with the same level of accuracy, the same value of Δz was used for all methods. Several values of Δz were tested and the one used was small enough so that for $\Delta z \pm \varepsilon$ ($\varepsilon > 0$ is a number such that $\Delta z > \varepsilon$), results varied less than 1%.

Applying the 5th order Gaussian Quadrature to equation (4.2) yields

$$I \approx \sum_{i=1}^{\alpha-1} m_i \sum_{j=1}^{5} w_j \cdot \left[f_1(m_i \cdot t_j + c_i) \cdot f_2(m_i \cdot t_j + c_i) \right] \qquad (4.3)$$

where $m_i = \frac{1}{2}(z_{i+1} - z_i)$, $c_i = \frac{1}{2}(z_{i+1} + z_i)$. The coefficients t_j are the roots of the 5th

degree Legendre polynomial, and the coefficients w_j are the weights such that the

integration is exact for any polynomial of degree less than or equal to five. Table 1

gives the values of t_j, w_j for $j = 1, 2, \ldots 5$ below [33].

Table 1
Weights and nodes for 5th order Gaussian Quadrature.

j	nodes (t_j)	weights (w_j)
1	0.9061798459	0.2369268850
2	0.5384693101	0.4786286705
3	0.0000000000	0.5688888889
4	-0.5384693101	0.4786286705
5	-0.9061798459	0.2369268850

In order to quantify the computational cost presented by each of the methods,

the number of integrals calculated will be counted and the totals will be compared in

each case. Consider the problem of finding the low energy neutron flux for N_E

distinct energy values at N_x distinct depths in a single slab of material with a total of

β distinct atomic species.

In the Collocation method, the first integrals to be computed appear in

calculation of the A-matrix; they are

$$a_{ij}^{(2)} = \sum_{\beta} \int_{E_a}^{E_{j+1}} \sigma_{11,\beta}^{re}(E_i, E')B_j(E')dE' \tag{4.4}$$

$$a_{ij}^{(3)} = \sum_{\beta} \int_{E_a}^{E_\beta} \sigma_{11,\beta}^{el}(E_i, E')B_j(E')dE' \tag{4.5}$$

where the upper limit in equation (4.5) is dependent on the target atom considered.

Since A is an upper triangular $N_E \times N_E$ matrix it is clear that one must compute the

integral in equation (4.4) a total of $\beta \cdot \dfrac{N_E(N_E + 1)}{2}$ times and the integral in equation

(4.5) a total of $\beta \cdot \dfrac{N_E(N_E + 1)}{2}$ times. Hence, the total number of integrals computed

in the A-matrix is $\beta N_E(N_E + 1)$. The next set of integrals to be computed arise from

the solution to the system of ordinary differential equations; they are

$$\phi^f(x, E_{N_E-j}) = \int_0^x e^{a_{N_E-j,N_E-j}(x-x')} \left[\eta^f(x', E_{N_E-j}) \right.$$
$$\left. + (1 - \delta_{j0}) \cdot \sum_{k=0}^{j-1} a_{N_E-j,N_E-k} \, \phi^f(x', E_{N_E-k}) \right] dx' \tag{4.6}$$

$$\phi^b(x, E_{N_E-j}) = \int_x^L e^{-a_{N_E-j,N_E-j}(x-x')} \left[\eta^b(x', E_{N_E-j}) \right.$$
$$\left. + (1 - \delta_{j0}) \cdot \sum_{k=0}^{j-1} a_{N_E-j,N_E-k} \phi^b(x', E_{N_E-k}) \right] dx' \tag{4.7}$$

Recall, that the solution is required at N_E energy values and N_x depths. Hence, the

solutions ϕ^f and ϕ^b must be computed a total of $N_E \cdot N_x$ times each. The total

number of integrals computed in the Collocation method is therefore

$$I_{tot}^C = \left[\beta N_E(N_E + 1) \right] + \left[2N_E N_x \right] \tag{4.8}$$

The right hand side of equation (4.8) has been grouped in order to differentiate

between those integrals related to the A-matrix and those integrals related to the

solution of the system of differential equations. It has been observed that the A-matrix

is the more time-consuming of the two since $N_E > N_x$ in most cases, and for more

complex materials, the factor β could be as high as 10. In general, the quantity βN_E^2

will be the dominant term in equation (4.8).

In Wilson's method, the first integrals to be computed arise from the

fundamental solution given as

$$\phi_0^f(x, E) = \int_0^x e^{-\sigma_1(E)(x-x')} \eta^f(x', E)\, dx' \tag{4.9}$$

$$\phi_0^b(x, E) = \int_x^L e^{\sigma_1(E)(x-x')} \eta^b(x', E)\, dx' \tag{4.10}$$

Again, note that the solution is required at N_E energy values and N_x depths;

therefore, the integrals in equations (4.9) and (4.10) must be computed a total $N_E \cdot N_x$

times each, yielding a total of $2N_E \cdot N_x$. The next set of integrals to be computed are

the source terms generated by the fundamental solutions, namely

$$\xi^f(x, E) = \sum_\beta \int_E^\infty \sigma_{11,\beta}^{re} \phi_0^f\, dE' + \sum_\beta \int_E^{E/\alpha_\beta} \sigma_{11,\beta}^{el} \phi_0^f\, dE' \tag{4.11}$$

$$\xi^b(x, E) = \sum_\beta \int_E^\infty \sigma_{11,\beta}^{re} \phi_0^b\, dE' + \sum_\beta \int_E^{E/\alpha_\beta} \sigma_{11,\beta}^{el} \phi_0^b\, dE' \tag{4.12}$$

The source terms ξ^f and ξ^b will also need to be computed at N_E energy values and

N_x depths; the total number of times one would compute the source integral is

$2\beta N_E N_x$. Recall, that the last step in Wilson's method was to solve for the

perturbational term by using the Collocation technique; this results in a total of

$\beta N_E(N_E + 1) + 2N_E N_x$ integral calculations. Hence, the total number of integrals to

be computed for Wilson's method is

$$I_{tot}^{W} = \left[2\beta N_E N_x\right] + \left[2N_E N_x\right] + \left\{\left[\beta N_E(N_E + 1)\right] + \left[2N_E N_x\right]\right\} \qquad (4.13)$$

As expected, a non-negligible number of integral calculations have been added. Of particular interest is the fact that the source integrals will dominate the computational time and therefore, the factor of $2\beta N_E N_x$ will be the most important term in trying to decrease the total computational cost.

In the Fixed Point – Series method, we only have two sets of integrals – those given by equations (4.9), (4.10), and those given by equations (4.11), (4.12). Recall that those sets of integrals are computed several times resulting in a series solution with K terms in it. The total number of integrals to be computed will therefore be given by

$$I_{tot}^{S} = K\left\{\left[2\beta N_E N_x\right] + \left[2N_E N_x\right]\right\} \qquad (4.14)$$

Again, the source calculations are by far the most expensive computationally speaking, and therefore the term $K\left(2\beta N_E N_x\right)$ will dominate run-time considerations.

Consider the case where $N_E = 63$, $N_x = 10$ and $\beta = 2$ (this could correspond to finding the low energy neutron flux in water for 10 distinct depths and 63 distinct energy values – a very common problem). Plugging these numbers into (4.8), (4.13), and (4.14) yields

$$I_{tot}^{C} = 9,324 \qquad (4.15)$$

$$I_{tot}^{W} = 13,104 \qquad (4.16)$$

$$I_{tot}^{S} = 94,500 \qquad (4.17)$$

The value for I_{tot}^S was obtained by assuming 25 iterations were needed for

convergence. Though the number of iterations needed was found to be energy grid

and material dependent, it was found that anywhere from 15 to 45 terms in the series

could be needed. The number of integral calculations gives an indication as to overall

computational cost, but it can be deceiving since some integrals proved to be more

costly than others.

Clearly, one could indeed pick values for N_E, N_x, and β ultimately showing

the methods to be comparable in computational cost, but the idea here was to compare

the methods under the same circumstances in order to highlight the possible

differences between them. Further, the source integrals used in the Fixed Point –

Series method typically require the longest run time of any of the integrals mentioned

above, and hence run time comparisons will only exaggerate the behavior displayed in

equations (4.15) - (4.17).

MULTI-LAYER HZETRN

Recall from chapter II that the neutron flux was decomposed into a high-

energy straight-ahead component and a low-energy isotropic component modeled as a

bi-directional form; the computer code HZETRN-05, developed by John Wilson et. al.

at NASA LaRC [6,9-15], was used to solve for the high-energy component and an

isotropic neutron source term was then calculated from this numerical solution.

Currently, HZETRN-05 is setup to calculate radiation transport through three

materials referred to as materials one, two and three respectively. The algorithm first

calculates the flux at a number of depths in material one; the depths are defined at the

beginning of the program (including the zero depth), and stored in the x(k) array

$(k = 1, ..., IX)$. Then for each of the material one depths, the algorithm calculates

radiation flux at a number of depths in material two - also defined at the beginning of

the program (including the zero depth) - and stored in the $y(l)$ array $(l = 1, ..., IY)$.

Finally, for each of the material one and material two depth combinations, the

algorithm calculates radiation flux at a number of depths in material three defined at

the beginning of the program (including the zero depth), and stored in the $u(m)$ array

$(m = 1, ..., IU)$. All of the fluxes due to galactic cosmic radiation are stored in the

$f(i, j, k, l, m)$ array, where $f(i, j, k, l, m)$ is the flux of type j particles with energy

$et(i)$ at material one depth $x(k)$, material two depth $y(l)$, and material three depth $u(m)$.

Alternatively, the fluxes due to solar particle events or fluxes due to trapped radiation

are stored in the $ff(i, j, k, l, m)$ array where the only difference now is that the index i

refers to an energy $etf(i)$. Hereafter, only the $f(i, j, k, l, m)$ array will be mentioned

and it will be assumed that all statements made about it are true for $ff(i, j, k, l, m)$ as

well.

Because HZETRN-05 computes forward moving fluxes, the output it produces

can be used to approximated many different physical situations. For example,

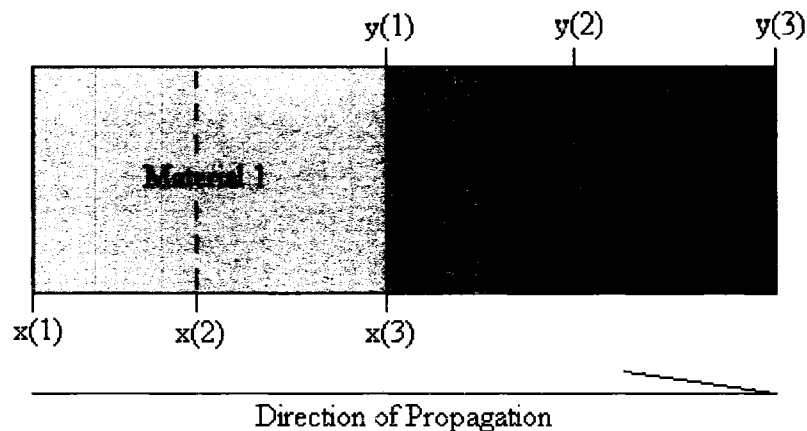consider the simple case $IX=IY=3$, $IU=1$ illustrated in fig. 16 below.

Fig. 16. Two material example.

The quantity $f(i,j,2,1,1)$ is the flux of type j particles with energy $et(i)$ at depth $x(2)$, $y(1) = 0$, $u(1) = 0$. However, because forward moving fluxes do not "see" anything past the current depth, the quantity $f(i,j,2,1,1)$ could be interpreted as the flux of type j ions with energy $et(i)$ at depth $x(2)$ with just about anything behind it. Alternatively, it could be viewed as the flux of type j ions with energy $et(i)$ propagating through the backside of a material of total depth $x(2)$ with absolutely nothing behind it.

The source terms generated by the high-energy straight-ahead solution display the same type of flexibility as well. The arrays $NSORC(i,k,l,m)$ and $NSORCF(i,k,l,m)$ are used to store the source terms where the index i refers to the energy value $EN(i)$ and the indices k, l, m refer to the depths $x(k)$, $y(l)$, $u(m)$ as before. Note that the arrays $NSORC$ and $NSORCF$ can also be used for a variety of material configurations. Historically, such ambiguities were both acceptable and necessary because no backward flux components were considered. It was not until Clowdsley's work

[16,25,30] that the need to define maximum depths was discovered. Perhaps the best way to see the need for such definitions is to consider the boundary conditions for the forward and backward components of low energy neutron flux in a single slab of material of depth L, namely

$$\phi^f(E,0) = 0 \tag{4.18}$$

$$\phi^b(E,L) = 0 \tag{4.19}$$

Equation (4.19) clearly shows that the backward component of flux must be referenced from some maximum depth $x = L$. All of the intermediate depths between $x = 0$ and $x = L$ are now forced to represent depths within the material. As such, many of the combinations previously available in a multi-material configuration can now be disregarded. Dropping such combinations will not only speed the program up greatly, but will also result in a much more specific output. A discussion of how to implement the three methods into HZETRN-05 for two or three material configurations is now given.

TWO MATERIALS

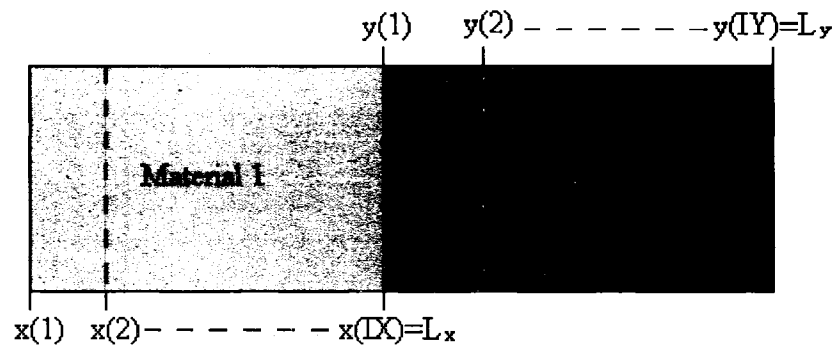Consider the two-material configuration given below in fig. 17

Fig. 17. General two material configuration.

Assume that there are IX material one depths ranging from $x_1 = x(1) = 0$ to

$x_{IX} = x(IX) = L_x$, and there are IY material two depths ranging from $y_1 = y(1) = 0$ to

$y_{IY} = y(IY) = L_y$. There will also be IIN energy values ranging from $E_1 = E_{min}$ to

$E_{IIN} = E_{max}$ (Normally the values $E_{min} = .01\,MeV$ and $E_{max} = 400\,MeV$ are taken.).

The forward and backward components of flux will only be defined if $x \in [0, L_x]$ and

$y = 0$ or $x = L_x$ and $y \in [0, L_y]$; therefore, the forward component flux is defined as

$$\phi^f(x, y, E) = \begin{cases} \phi_x^f(x, E) & , x \in [0, L_x] \ and \ y = 0 \\ \phi_y^f(y, E) & , x = L_x \ and \ y \in [0, L_y] \end{cases} \qquad (4.20)$$

and the backward component of flux at any point in the material can be defined as

$$\phi^b(x, y, E) = \begin{cases} \phi_x^b(x, E) & , x \in [0, L_x] \ and \ y = 0 \\ \phi_y^b(y, E) & , x = L_x \ and \ y \in [0, L_y] \end{cases} \qquad (4.21)$$

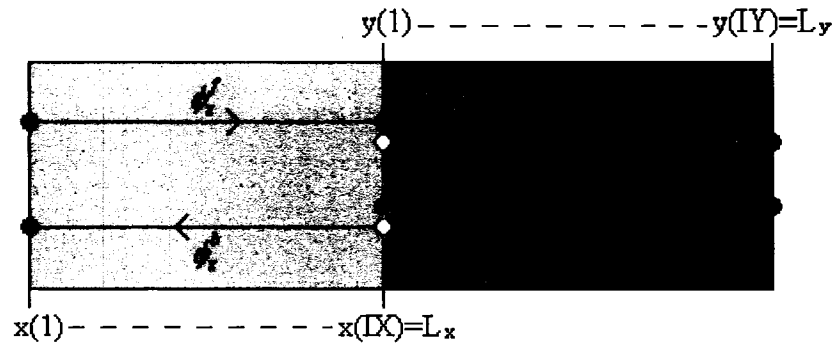The fig. 18 provides a visual summary of definitions (4.20) and (4.21).

Fig. 18. Forward and backward components of the isotropic neutron flux in two materials.

The fluxes ϕ^f and ϕ^b are required to be continuous at the interface $x = L_x$, $y = 0$; this condition will be satisfied by requiring

$$\phi_y^f(0,E) = \phi_x^f(L_x,E) \tag{4.22}$$

$$\phi_x^b(L_x,E) = \phi_y^b(0,E) \tag{4.23}$$

Assume also that HZETRN-05 has generated the source terms in materials one and two. Let the forward component of the source term in materials one and two be denoted as $\eta_x^f(x,E)$ for $x \in [0,L_x]$ and $\eta_y^f(y,E;L_x)$ for $y \in [0,L_y]$, and the backward component of the source term in materials one and two be denoted as $\eta_x^b(x,E)$ for $x \in [0,L_x]$ and $\eta_y^b(y,E;L_x)$ for $y \in [0,L_y]$. The L_x dependencies in $\eta_y^f(y,E;L_x)$, $\eta_y^b(y,E;L_x)$ are used to denote that these source terms were calculated in material two with a material one of depth L_x in front of it. Noting the definition of the source term given in chapter II and the fact that the production cross-sections are material dependent implies that the source terms will not be continuous across the interface

between the two materials. That is, $\eta_x^f(L_x, E) \neq \eta_y^f(0, E)$ and $\eta_x^b(L_x, E) \neq \eta_y^b(0, E)$.

Since the boundary condition for the forward component of the flux is given at the front of the material, and the boundary condition for the backward component is given at the back of the material, the first step must be to find the forward flux in material one and the backward flux in material two as illustrated in fig. 19 below.
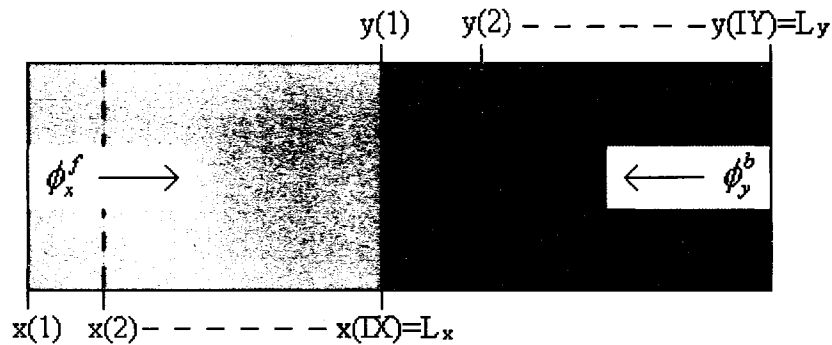
Fig. 19. First steps in calculating the forward and backward components of the isotropic neutron flux in two materials.

Though the front and back boundary conditions are automatically satisfied in all of the methods, implementation of the continuity condition differs between the three methods and therefore they must be dealt with individually.

The solution given by the Collocation method for the forward component in material one is

$$\phi_x^f(x, E_{IIN-j}) = \int_0^x e^{a_{IIN-j,IIN-j}(x-x')} \Big[\eta^f(x', E_{IIN-j})$$
$$+ (1-\delta_{j0}) \cdot \sum_{k=0}^{j-1} a_{IIN-j,IIN-k} \phi_x^f(x', E_{IIN-k}) \Big] dx' \tag{4.24}$$

The coefficients a_{ij} are obtained via the definition for the A-matrix given in chapter

III with cross-sections related to material one. The front condition is clearly satisfied

since $\phi_x^f(0, E_{IIN-j}) = 0$, but in order to properly define the boundary condition at the

interface one must reconsider the system of ordinary differential equations from which

the forward component was obtained. For the forward component of flux in material

two, this system is

$$\frac{\partial}{\partial y}\begin{bmatrix} \phi_y^f(y, E_1) \\ \phi_y^f(y, E_2) \\ \vdots \\ \phi_y^f(y, E_{IIN}) \end{bmatrix} = \begin{bmatrix} b_{11} & b_{12} & \cdots & b_{1,IIN} \\ & b_{22} & & \vdots \\ & & \ddots & \vdots \\ & & & b_{IIN,IIN} \end{bmatrix}\begin{bmatrix} \phi_y^f(y, E_1) \\ \phi_y^f(y, E_2) \\ \vdots \\ \phi_y^f(y, E_{IIN}) \end{bmatrix}$$
$$+ \begin{bmatrix} \eta_y^f(y, E_1; L_x) \\ \eta_y^f(y, E_2; L_x) \\ \vdots \\ \eta_y^f(y, E_{IIN}; L_x) \end{bmatrix} \tag{4.25}$$

where the coefficients $\{b_{ij}\}$ are obtained using the definition of the A-matrix given in

chapter III, using cross-sections for material two. Examining the last equation in the

system of equations (4.25) it is clear that

$$\frac{\partial}{\partial y}\phi_y^f(y, E_{IIN}) - b_{IIN,IIN}\phi_y^f(y, E_{IIN}) = \eta_y^f(y, E_{IIN}; L_x) \tag{4.26}$$

and upon introducing an integrating factor equation (4.26) can be rewritten as

$$\int_0^y \frac{\partial}{\partial y'}\left[e^{-b_{IIN,IIN}y'}\phi_y^f(y', E_{IIN})\right]dy' = \int_0^y e^{-b_{IIN,IIN}y'}\eta_y^f(y', E_{IIN}; L_x)dy' \tag{4.27}$$

The left hand side can be further simplified so that

$$e^{-b_{IIN,IIN}y}\phi_y^f(y, E_{IIN}) - \phi_y^f(0, E_{IIN}) = \int_0^y e^{-b_{IIN,IIN}y'}\eta_y^f(y', E_{IIN}; L_x)dy' \tag{4.28}$$

Note that we require $\phi_y^f(0, E_{IIN}) = \phi_x^f(L_x, E_{IIN})$, so that equation (4.28) is now given in the compact form

$$\phi_y^f(y, E_{IIN}) = \phi_x^f(L_x, E_{IIN})e^{b_{IIN,IIN} \cdot y} + \int_0^y e^{b_{IIN,IIN}(y-y')} \eta_y^f(y', E_{IIN}; L_x)\, dy' \quad (4.29)$$

The $IIN - 1^{st}$ equation is

$$\frac{\partial}{\partial y}\phi_y^f(y, E_{IIN-1}) - b_{IIN-1,IIN-1}\phi_y^f(y, E_{IIN-1})$$

$$= \eta_y^f(y, E_{IIN}; L_x) + b_{IIN-1,IIN}\phi_y^f(y, E_{IIN}) \quad (4.30)$$

following the exact procedure given above, the solution to equation (4.30) is

$$\phi_y^f(y, E_{IIN-1}) = e^{b_{IIN-1,IIN-1} \cdot y}\phi_x^f(L_x, E_{IIN-1})$$

$$+ \int_0^y e^{b_{IIN-1,IIN-1}(y-y')}\left[\begin{array}{c}\eta_y^f(y', E_{IIN-1}; L_x) \\ +b_{IIN-1,IIN}\phi_y^f(y', E_{IIN})\end{array}\right]dy' \quad (4.31)$$

Clearly, in order to solve the remaining $IIN - 2$ equations, one would continue the back substitution procedure and note the interface boundary condition so that the solution to the system of differential equations (4.25) can be written in the closed form

$$\phi_y^f(y, E_{IIN-j}) = e^{b_{IIN-j,IIN-j} \cdot y}\phi_x^f(L_x, E_{IIN-j})$$

$$+ \int_0^y e^{b_{IIN-j,IIN-j}(y-y')}\left[\eta_y^f(y', E_{IIN-j}; L_x)\right.$$

$$\left. +(1-\delta_{j0}) \cdot \sum_{k=0}^{j-1} b_{IIN-j,IIN-k}\phi_y^f(y', E_{IIN-k})\right]dy' \quad (4.32)$$

The backward component of the flux is handled in exactly the same way, except that transport is started in material two instead of material one. The solution given by the Collocation method in material two for $y \in [0, L_y]$ is

$$\phi_y^b(y, E_{IIN-j}) = \int_y^{L_y} e^{-b_{IIN-j,IIN-j}(y-y')} \Big[\eta_y^b(y', E_{IIN-j}; L_x)$$

$$+ (1 - \delta_{j0}) \cdot \sum_{k=0}^{j-1} b_{IIN-j,IIN-k} \phi_y^b(y', E_{IIN-k}) \Big] dy' \qquad (4.33)$$

The back condition has been satisfied since $\phi_y^b(L_y, E_{IIN-j}) = 0$; in order to satisfy the

interface boundary condition one must again reconsider the system of differential

equations from which the solution for the backward component in material one is

obtained. This system is

$$-\frac{\partial}{\partial x} \begin{bmatrix} \phi_x^b(x, E_1) \\ \phi_x^b(x, E_2) \\ \vdots \\ \phi_x^b(x, E_{IIN}) \end{bmatrix} = \begin{bmatrix} a_{11} & a_{12} & \cdots & a_{1,IIN} \\ & a_{22} & & \vdots \\ & & \ddots & \vdots \\ & & & a_{IIN,IIN} \end{bmatrix} \begin{bmatrix} \phi_x^b(x, E_1) \\ \phi_x^b(x, E_2) \\ \vdots \\ \phi_x^b(x, E_{IIN}) \end{bmatrix}$$

$$+ \begin{bmatrix} \eta_x^b(x, E_1) \\ \eta_x^b(x, E_2) \\ \vdots \\ \eta_x^b(y, E_{IIN}) \end{bmatrix} \qquad (4.34)$$

The last equation in the system of equations (4.34) is

$$\frac{\partial}{\partial x} \phi_x^b(x, E_{IIN}) + a_{IIN,IIN} \phi_x^b(x, E_{IIN}) = -\eta_x^b(x, E_{IIN}) \qquad (4.35)$$

Introduce an integrating factor and integrate equation (4.35) to obtain

$$\int_x^{L_x} \frac{\partial}{\partial x'} \Big[e^{a_{IIN,IIN} x'} \phi_x^b(x', E_{IIN}) \Big] dx' = -\int_x^{L_x} e^{a_{IIN,IIN} x'} \eta_x^b(x', E_{IIN}) dx' \qquad (4.36)$$

The left hand side of equation (4.36) can be further simplified as

$$e^{a_{IIN,IIN} L_x} \phi_x^b(L_x, E_{IIN}) - e^{a_{IIN,IIN} x} \phi_x^b(x, E_{IIN}) = -\int_x^{L_x} e^{a_{IIN,IIN} x'} \eta_x^b(x', E_{IIN}) dx' \qquad (4.37)$$

Note that $\phi_x^b(L_x, E_{IIN}) = \phi_y^b(0, E_{IIN})$, and equation (4.37) becomes

$$\phi_x^b(x, E_{IIN}) = e^{-a_{IIN,IIN}(x-L_x)}\phi_y^b(0, E_{IIN}) + \int_x^{L_x} e^{-a_{IIN,IIN}(x-x')}\eta_x^b(x', E_{IIN})\,dx' \qquad (4.38)$$

The remaining $N-1$ equations are solved in a similar manner using the back substitution procedure outlined above; the solution for the backward component of flux in material one is given in the compact form

$$\phi_x^b(x, E_{IIN-j}) = e^{-a_{IIN-j,IIN-j}(x-L_x)}\phi_y^b(0, E_{IIN-k})$$

$$+ \int_x^{L_x} e^{-a_{IIN-j,IIN-j}(x-x')}\left[\eta_x^b(x', E_{IIN-j})\right. \qquad (4.39)$$

$$\left. + (1-\delta_{j0})\cdot\sum_{k=0}^{j-1} a_{IIN-j,IIN-k}\phi_x^b(x', E_{IIN-k})\right]dx'$$

For Wilson's method, the implementation is slightly more difficult since the propagation is handled in two steps. Begin by solving for the forward component in material one and the backward component in material two. Recall that the forward and backward components were both split as a sum of a fundamental term and a perturbational term as $\phi^f = \phi_0^f + \phi_1^f$ and $\phi^b = \phi_0^b + \phi_1^b$, or

$$\phi^f(x, y, E) = \begin{cases} \phi_{x,0}^f(x, E) + \phi_{x,1}^f(x, E) & , x \in [0, L_x] \text{ and } y = 0 \\ \phi_{y,0}^f(y, E) + \phi_{y,1}^f(y, E) & , y \in [0, L_y] \text{ and } x = L_x \end{cases} \qquad (4.40)$$

$$\phi^b(x, y, E) = \begin{cases} \phi_{x,0}^b(x, E) + \phi_{x,1}^b(x, E) & , x \in [0, L_x] \text{ and } y = 0 \\ \phi_{y,0}^b(y, E) + \phi_{y,1}^b(y, E) & , y \in [0, L_y] \text{ and } x = L_x \end{cases} \qquad (4.41)$$

The solution for the fundamental part of the forward component in material one given in chapter III is

$$\phi_{x,0}^f(x, E) = \int_0^x e^{-\sigma_1^{(r)}(E)(x-x')}\eta_x^f(x', E)\,dx' \qquad (4.42)$$

where the superscript x is to denote that the macroscopic cross-section is related to material one. The solution for the fundamental part of the backward component in material two was also given in chapter III

$$\phi^b_{y,0}(y,E) = \int_y^{L_y} e^{\sigma_1^{(y)}(E)(y-y')} \eta^b_y(y',E;L_x)\, dy' \tag{4.43}$$

where the superscript y is to denote the macroscopic cross-section is related to material two. The front condition is clearly satisfied by $\phi^f_{x,0}$, while $\phi^b_{y,0}$ clearly satisfies the back condition. In order to satisfy the interface boundary conditions, a procedure almost identical to that outlined for the Collocation method is used. Consider the differential equation for the fundamental forward component of flux in material two

$$\frac{\partial}{\partial y}\phi^f_{y,0}(y,E) + \sigma_1^{(y)}(E)\phi^f_{y,0}(y,E) = \eta^f_y(y,E;L_x) \tag{4.44}$$

Multiply both sides of equation (4.44) by the appropriate integrating factor and integrate to obtain

$$\int_0^y \frac{\partial}{\partial y'}\left[e^{\sigma_1^{(y)}(E)\cdot y'}\phi^f_{y,0}(y',E_{IIN}) \right] dy' = \int_0^y e^{\sigma_1^{(y)}(E)\cdot y'}\eta^f_y(y',E_{IIN};L_x)\, dy' \tag{4.45}$$

Note that $\phi^f_{y,0}(0,E) = \phi^f_{x,0}(L_x,E)$, and equation (4.45) becomes

$$\phi^f_{y,0}(y,E) = e^{-\sigma_1^{(y)}(E)\cdot y}\phi^f_{x,0}(L_x,E) + \int_0^y e^{-\sigma_1^{(y)}(E)\cdot(y-y')}\eta^f_y(y',E;L_x)\, dy' \tag{4.46}$$

Following an almost identical procedure, the fundamental part of the backward component in material one is found to be

$$\phi^b_{x,0}(x,E) = e^{\sigma_1^{(x)}(E)(x-L_x)}\phi^b_{y,0}(0,E) + \int_x^{L_x} e^{\sigma_1^{(x)}(E)(x-x')}\eta^b_x(x',E)\, dx' \tag{4.47}$$

For clarity, we will simplify notation here and recall that the next step in

Wilson's method was a source calculation. The source integrals are of the form

$$\xi_x^f(x, E) = \int_E \sigma_{11}^{(x)}(E, E')\phi_{x,0}^f(x, E')dE' \qquad (4.48)$$

$$\xi_y^f(y, E; L_x) = \int_E \sigma_{11}^{(y)}(E, E')\phi_{y,0}^f(y, E')dE' \qquad (4.49)$$

$$\xi_x^b(x, E) = \int_E \sigma_{11}^{(x)}(E, E')\phi_{x,0}^b(x, E')dE' \qquad (4.50)$$

$$\xi_y^b(y, E; L_x) = \int_E \sigma_{11}^{(y)}(E, E')\phi_{y,0}^b(y, E')dE' \qquad (4.51)$$

where the superscripts *(x)* and *(y)* suggest whether to use cross-sections related to the first or second materials respectively. Finally, using the source terms calculated in equations (4.48) - (4.51), one uses the Collocation method for two layers outlined above to solve for the perturbational term.

The Fixed Point – Series method can be summarized quite easily now that we have introduced how to enforce continuity of the fundamental solution across the interface. It will not be necessary to go into great detail here about how to implement the Fixed Point – Series method for a two-layer configuration - all that is required is a series of fundamental solutions and source calculations. One would repeatedly obtain the fundamental terms given by equations (4.42), (4.43), (4.46) and (4.47), and then calculate the source terms defined in equations (4.48) and (4.51).

The total computational cost for the two-layer configuration is of course greater than in the one-layer case. However, one cannot simply double the expressions obtained previously in order to approximate the computational cost presented. Such an approximation would be too simple since the number of x-values (IX) and the number of y-values (IY) may not be the same, and the number of atomic species in material one may not be the same as the number in material two. Let the

number of depths in material one be denoted as $N_x = IX$, and the number of depths in

material two be denoted as $N_y = IY$. Also, let β_x be the number of atomic species in

material one and β_y be the number of atomic species in material two. The total

number of integrals computed by each method in a two-layer configuration will now

be given by

$$I_{tot}^C = \left[N_E(N_E + 1)(\beta_x + \beta_y) \right] + \left[2N_E(N_x + N_y) \right] \tag{4.52}$$

$$\begin{aligned} I_{tot}^W = &\left[2N_E(\beta_x N_x + \beta_y N_y) \right] + \left[2N_E(N_x + N_y) \right] \\ &+ \left\{ \left[N_E(N_E + 1)(\beta_x + \beta_y) \right] + \left[2N_E(N_x + N_y) \right] \right\} \end{aligned} \tag{4.53}$$

$$I_{tot}^S = K \left\{ \left[2N_E(\beta_x N_x + \beta_y N_y) \right] + \left[2N_E(N_x + N_y) \right] \right\} \tag{4.54}$$

Clearly there will be an increase in computational cost dependent on the

number of atomic species and depth values used in the second layer. For one of the

early two-layer test runs conducted in this research, the values $\beta_x = 5$, $\beta_y = 2$,

$N_x = 10$, $N_y = 8$, and $N_E = 63$ were used. The number of integrals computed in each

method under these circumstances is

$$I_{tot}^C = 30,492 \text{ integrals} \tag{4.55}$$

$$I_{tot}^W = 41,076 \text{ integrals} \tag{4.56}$$

$$I_{tot}^S = 264,600 \text{ integrals} \tag{4.57}$$

As before, the Fixed-Point Series method is by far the most computationally expensive

method to use.

THREE MATERIALS

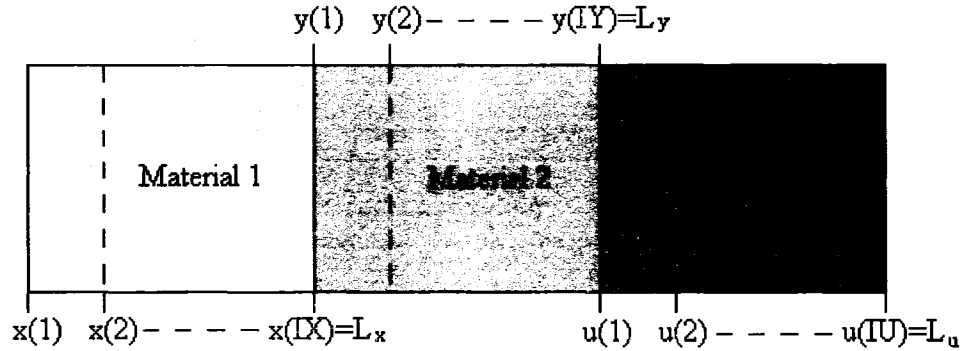Consider the three-material configuration given below in fig. 20.

Fig. 20. General three material configuration.

Assume that there are IX material one depths ranging from $x_1 = x(1) = 0$ to

$x_{IX} = x(IX) = L_x$; there are IY material two depths ranging from $y = y(1) = 0$ to

$y_{IY} = y(IY) = L_y$; there are IU material three depths ranging from $u_1 = u(1) = 0$ to

$u_{IU} = u(IU) = L_u$, and there are IIN energy values ranging from $E_1 = E_{\min}$ to

$E_{IIN} = E_{\max}$. The forward and backward components of the flux will be required to be

continuous across the interface between materials one and two and across the interface

between materials two and three. Define the forward component of the flux as

$$\phi^f(x,y,u,E) = \begin{cases} \phi_x^f(x,E) & , \ x \in [0,L_x] \ , \ y = 0 \ and \ u = 0 \\ \phi_y^f(y,E) & , \ x = L_x \ , \ y \in [0,L_y] \ and \ u = 0 \\ \phi_u^f(u,E) & , \ x = L_x \ , \ y = L_y \ and \ u \in [0,L_u] \end{cases} \tag{4.58}$$

$$\phi^b(x,y,u,E) = \begin{cases} \phi_x^b(x,E) & , \ x \in [0,L_x] \ , \ y = 0 \ and \ u = 0 \\ \phi_y^b(y,E) & , \ x = L_x \ , \ y \in [0,L_y] \ and \ u = 0 \\ \phi_u^b(u,E) & , \ x = L_x \ , \ y = L_y \ and \ u \in [0,L_u] \end{cases} \tag{4.59}$$

The piecewise definitions of the forward and backward components may be a bit
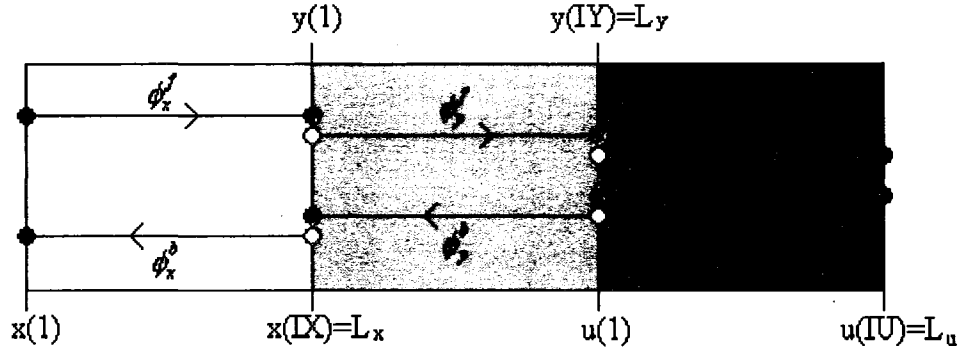
cumbersome; therefore, fig. 21 provides a visual summary.

Fig. 21. Forward and backward components of the isotropic neutron flux in three materials.

Recall that the fluxes ϕ^f and ϕ^b were required to be continuous at each of the interfaces; these conditions will be satisfied by demanding

$$\phi_y^f(0,E) = \phi_x^f(L_x,E) \tag{4.60}$$

$$\phi_u^f(0,E) = \phi_y^f(L_y,E) \tag{4.61}$$

$$\phi_y^b(L_y,E) = \phi_u^b(0,E) \tag{4.62}$$

$$\phi_x^b(L_x,E) = \phi_y^b(0,E) \tag{4.63}$$

As in the case of two materials, the source terms at the back boundary are required before backward propagation can begin. Hence, let HZETRN propagate and calculate source terms through materials one, two and three. The source values associated with material one will be denoted as $\eta_x^f(x,E)$, $\eta_x^b(x,E)$; the source values for material two with L_x g/cm^2 of material one in front of it will be denoted as

$\eta_y^f(y,E;L_x)$, $\eta_y^b(y,E;L_x)$, and the source values for material three with L_x g/cm^2 of

material one and L_y g/cm^2 of material two in front of it will be denoted as

$\eta_u^f(u,E;L_x,L_y)$ and $\eta_u^b(u,E;L_x,L_y)$. The L_x or L_y dependencies are used to note that

the source terms were calculated with a certain amount of material in front of the

current medium. The source terms will be discontinuous across the interfaces as

before.

Since the boundary condition for the forward component is given at the front

of the material, and the boundary condition for the backward component is given at

the back of the material, the first step must be to find the forward flux in material one

and the backward flux in material three as illustrated in fig. 22 below.
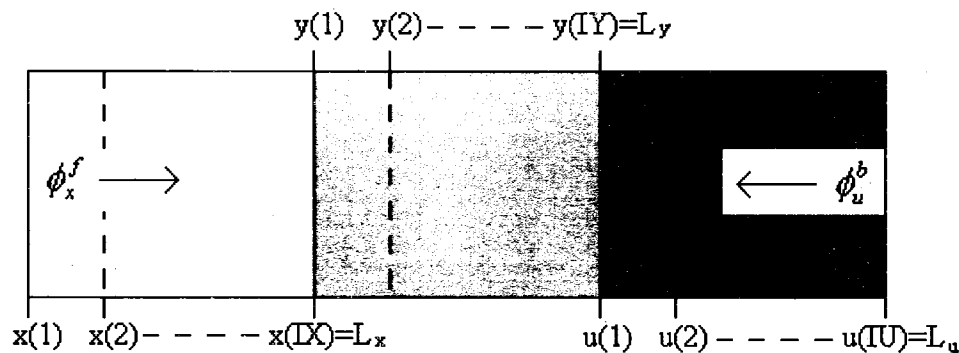

Fig. 22. First steps in calculating the forward and backward components of the
isotropic neutron flux in three materials.

Recall from above that the solution provided by the Collocation method for the

forward components in materials one and two are given by equations (4.24) and (4.32)

. It is easily verified that the forward component in material three must be given by

$$\phi_u^f(u, E_{IIN-j}) = e^{c_{IIN-j,IIN-j} \cdot u} \phi_y^f(L_y, E_{IIN-j})$$

$$+ \int_0^u e^{c_{IIN-j,IIN-j}(u-u')} \Big[\eta_u^f(y', E_{IIN-j}; L_x, L_y) \tag{4.64}$$

$$+ (1-\delta_{j0}) \cdot \sum_{k=0}^{j-1} c_{IIN-j,IIN-k} \phi_u^f(u', E_{IIN-k}) \Big] du'$$

where the coefficients $\{c_{ij}\}$ are obtained via the definition of the A-matrix given in chapter III using cross-sections related to material three.

The backward component of the flux in material three will be given by

$$\phi_u^b(u, E_{IIN-j}) = \int_u^{L_u} e^{-c_{IIN-j,IIN-j}(u-u')} \Big[\eta_u^b(u', E_{IIN-j}; L_x, L_u)$$

$$+ (1-\delta_{j0}) \cdot \sum_{k=0}^{j-1} c_{IIN-j,IIN-k} \phi_u^b(u', E_{IIN-k}) \Big] du' \tag{4.65}$$

Following the procedure outlined in the two-material case, the backward component in material two is

$$\phi_y^b(y, E_{IIN-j}) = e^{-b_{IIN-j,IIN-j}(y-L_y)} \phi_u^b(0, E_{IIN-k})$$

$$+ \int_y^{L_y} e^{-b_{IIN-j,IIN-j}(y-y')} \Big[\eta_y^b(y', E_{IIN-j}; L_x) \tag{4.66}$$

$$+ (1-\delta_{j0}) \cdot \sum_{k=0}^{j-1} b_{IIN-j,IIN-k} \phi_y^b(y', E_{IIN-k}) \Big] dy'$$

Finally, the backward component of the flux in material one is given as

$$\phi_x^b(x, E_{IIN-j}) = e^{-a_{IIN-j,IIN-j}(x-L_x)} \phi_y^b(0, E_{IIN-j})$$

$$\int_x^{L_x} e^{-a_{IIN-j,IIN-j}(x-x')} \Big[\eta_x^b(x', E_{IIN-j}) \tag{4.67}$$

$$+ (1-\delta_{j0}) \cdot \sum_{k=0}^{j-1} a_{IIN-j,IIN-k} \phi_x^b(x', E_{IIN-k}) \Big] dx'$$

Implementation of Wilson's method in three materials involves nothing more than repeating the above analysis; therefore, the results are given without details. Let the forward and backward components of flux be defined as

$$\phi^f(z,E) = \begin{cases} \phi^f_{x,0}(x,E) + \phi^f_{x,1}(x,E) & , x \in [0, L_x] \ , \ y = 0 \ \ and \ \ u = 0 \\ \phi^f_{y,0}(y,E) + \phi^f_{y,1}(y,E) & , x = L_x \ , \ y \in [0, L_y] \ and \ \ u = 0 \\ \phi^f_{u,0}(u,E) + \phi^f_{u,1}(u,E) & , x = L_x \ , \ y = L_y \ \ and \ \ u \in [0, L_u] \end{cases} \quad (4.68)$$

$$\phi^b(z,E) = \begin{cases} \phi^b_{x,0}(x,E) + \phi^b_{x,1}(x,E) & , x \in [0, L_x] \ , \ y = 0 \ \ and \ \ u = 0 \\ \phi^b_{y,0}(y,E) + \phi^b_{y,1}(y,E) & , x = L_x \ , \ y \in [0, L_y] \ and \ \ u = 0 \\ \phi^b_{u,0}(u,E) + \phi^b_{u,1}(u,E) & , x = L_x \ , \ y = L_y \ \ and \ \ u \in [0, L_u] \end{cases} \quad (4.69)$$

The solutions for the fundamental part of the forward component in materials one and two are given by equations (4.42) and (4.46). The fundamental part of the forward component in material three is

$$\phi^f_{u,0}(u,E) = e^{-\sigma_1^{(u)}(E)u} \phi^f_{y,0}(L_y,E) + \int_0^u e^{-\sigma_1^{(u)}(E)(u-u')} \eta_u^f(u',E;L_x,L_y) du' \quad (4.70)$$

where the superscripts (x), (y) or (u) are used to denote whether the macroscopic cross-section is related to materials one, two or three respectively. The interface condition will also be satisfied since

The solution for the fundamental part of the backward component in material three is

$$\phi^b_{u,0}(u,E) = \int_u^{L_u} e^{\sigma_1^{(u)}(E)(u-u')} \eta_u^b(u',E;L_x,L_y) du' \quad (4.71)$$

and the fundamental part of the backward component in material two is

$$\phi^b_{y,0}(y,E) = e^{\sigma_1^{(y)}(E)(y-L_y)} \phi^b_{u,0}(0,E) + \int_y^{L_y} e^{\sigma_1^{(y)}(E)(y-y')} \eta_y^b(E,y';L_x) dy' \quad (4.72)$$

so that the fundamental part of the backward component in material one is written as

$$\phi^b_{x,0}(x,E) = e^{\sigma_1^{(x)}(E)(x-L_x)} \phi^b_{y,0}(0,E) + \int_x^{L_x} e^{\sigma_1^{(x)}(E)(x-x')} \eta_x^b(x',E) dx' \quad (4.73)$$

The source calculations here are exactly the same as in the two-layer case with the addition of two extra terms – forward and backward sources in material three. The

source integrals are of the form

$$\xi_x^f(x,E) = \int_E \sigma_{11}^{(x)}(E,E')\phi_{x,0}^f(x,E')dE' \tag{4.74}$$

$$\xi_y^f(y,E;L_x) = \int_E \sigma_{11}^{(y)}(E,E')\phi_{y,0}^f(y,E')dE' \tag{4.75}$$

$$\xi_u^f(u,E;L_x,L_y) = \int_E \sigma_{11}^{(u)}(E,E')\phi_{u,0}^f(u,E')dE' \tag{4.76}$$

$$\xi_x^b(x,E) = \int_E \sigma_{11}^{(x)}(E,E')\phi_{x,0}^b(x,E')dE' \tag{4.77}$$

$$\xi_y^b(y,E;L_x) = \int_E \sigma_{11}^{(y)}(E,E')\phi_{y,0}^b(y,E')dE' \tag{4.78}$$

$$\xi_u^b(u,E;L_x,L_y) = \int_E \sigma_{11}^{(u)}(E,E')\phi_{u,0}^b(u,E')dE' \tag{4.79}$$

where the superscripts *(x)*, *(y)*, and *(u)* indicate whether cross-sections related to the first, second or third materials respectively are used. Finally, using the source terms calculated in equations (4.74) -(4.79), one uses the Collocation method for three layers outlined above to solve for the perturbational term.

The Fixed Point – Series method can once again be summarized quite easily now that we have introduced how to enforce continuity of the fundamental solution across the interfaces. Ultimately, one would repeatedly obtain the fundamental terms given above, and then calculate the source terms defined in equations (4.74)-(4.79).

The total computational cost for the three-layer configuration will once again increase depending on the number of depths and atoms in the third material.

Let $N_x = IX$, $N_y = IY$, and $N_u = IU$. Also, the quantity β referred to the number of distinct atoms in the material. Let β_x be the number of atoms in material one, β_y be the number of atoms in material two, and β_u be the number of atoms in material three.

The total number of integrals computed by each method in a two-layer configuration will now be given by

$$I_{tot}^C = \left[N_E(N_E+1)(\beta_x + \beta_y + \beta_u) \right] + \left[2N_E(N_x + N_y + N_u) \right] \tag{4.80}$$

$$I_{tot}^W = \left[2N_E(\beta_x N_x + \beta_y N_y + \beta_u N_u) \right] + \left[2N_E(N_x + N_y + N_u) \right]$$
$$+ \left\{ \left[N_E(N_E+1)(\beta_x + \beta_y + \beta_u) \right] + \left[2N_E(N_x + N_y + N_u) \right] \right\} \tag{4.81}$$

$$I_{tot}^S = K \left\{ \left[2N_E(\beta_x N_x + \beta_y N_y + \beta_u N_u) \right] + \left[2N_E(N_x + N_y + N_u) \right] \right\} \tag{4.82}$$

If the values $\beta_x = 5$, $\beta_y = 2$, $\beta_u = 2$, $N_x = 10$, $N_y = 8$, $N_u = 8$ and $N_E = 63$ are used, the number of integrals computed in each method is

$$I_{tot}^C = 39,564 \text{ integrals} \tag{4.83}$$

$$I_{tot}^W = 53,172 \text{ integrals} \tag{4.84}$$

$$I_{tot}^S = 340,200 \text{ integrals} \tag{4.85}$$

The overall increase in computational cost was not as drastic as it was in the jump from one to two materials; this is entirely due to the specific values chosen for the number of depths and atoms in each material. However, the important thing to notice here is the overwhelming computational cost presented by all of the methods in a three-material configuration.

CHAPTER V

RESULTS AND CONCLUSIONS

The uncoupled system of equations describing the forward and backward components of the low energy neutron flux is solved using each of the three methods for several different environments and shielding configurations. The first set of comparisons is made for the February 23, 1956 solar particle event (SPE) in one and two layer configurations. This particular SPE was chosen because it has been studied extensively over the past 50 years [6] and therefore provides a good place to start verification of the bi-directional model and the three solution methods. Next, Monte Carlo data [2] for the neutron flux aboard the International Space Station (ISS) and Russian Space Station (MIR) are considered. Though the ISS has received much more attention than MIR in recent years, they occupy similar orbital altitudes and inclinations so that under certain circumstances they can be studied simultaneously. Radiation studies within either of the stations is of the utmost importance due to the critical roles both of them will play in future space flight missions and research. Finally, the methods are applied to various three-layer configurations to verify their agreement in a more complicated physical system.

FEBRUARY 23, 1956 SOLAR PARTICLE EVENT

The HZETRN-05 computer code is able to consider three different types of radiation environments to be used as boundary conditions for the propagator routine – solar particle events, galactic cosmic rays (GCR) and trapped radiation (TRP). Fig. 23

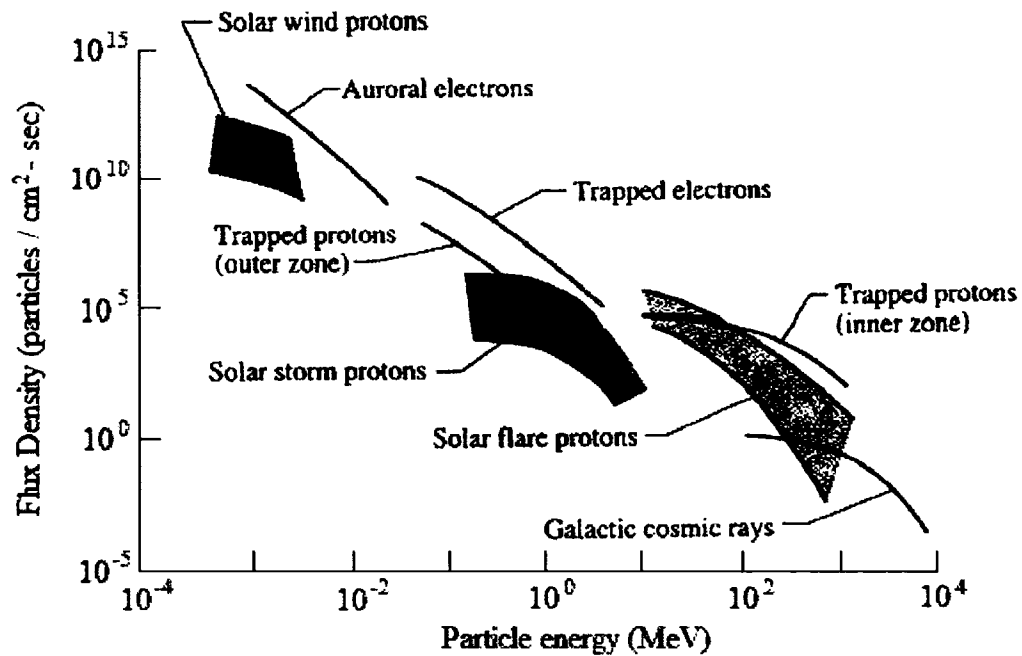characterizes the energies associated with different types of radiation in space [6].

Fig. 23. Space radiation environment.

A solar particle event can be described as a mass ejection of energetic protons from the sun [17]; in fig. 23 these protons are represented by the solar flare and solar storm regions. The ejected protons will ultimately interact with shielding materials resulting in production of neutrons and other light ions; the neutron production and propagation is the primary interest here.

The SPE on February 23, 1956 was the first well-documented event and is still studied extensively today due to its relative magnitude; the other SPEs available in HZETRN-05 are: 1960 (LaRC), 1960 (KING), 1972 (LaRC), 1989 (August), 1989 (September), 1989 (October). The seven SPEs are shown below in fig. 24.
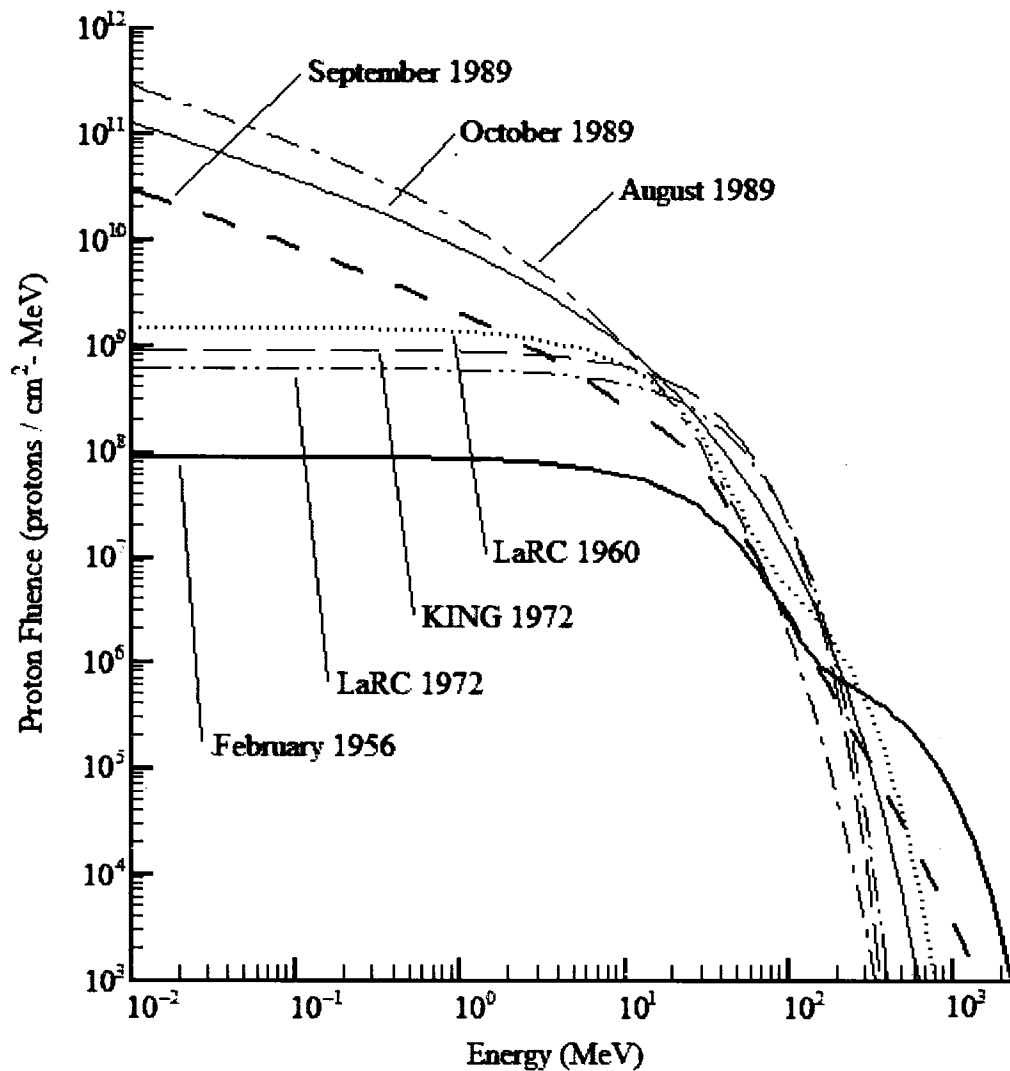
Fig. 24. Proton spectra for SPEs available in HZETRN-05.

From fig. 24, it is clear that the February 1956 spectrum has the largest high-energy proton fluence of the seven SPEs and will therefore result in the greatest secondary neutron production.

To clarify the results given below, recall from chapter II that the solution for the neutron flux (or fluence) was split according to $\phi = \phi^{HZETRN} + \phi^{iso}$, where the

isotropic part was further split into forward and backward components as

$\phi^{iso} = \phi^f + \phi^b$. The solutions marked ϕ^{HZETRN} were obtained from HZETRN-05 using

only the straight-ahead component of the production cross-sections. In contrast, the

curves marked "HZETRN-05 Result" were obtained from HZETRN-05 using the full

production cross-section - this curve represents the current neutron flux results given

by HZETRN-05.

The three methods are first compared in $100 \, gm/cm^2$ of pure aluminum with

the February, 1956 SPE as boundary condition. Fig. 25 shows the three methods for
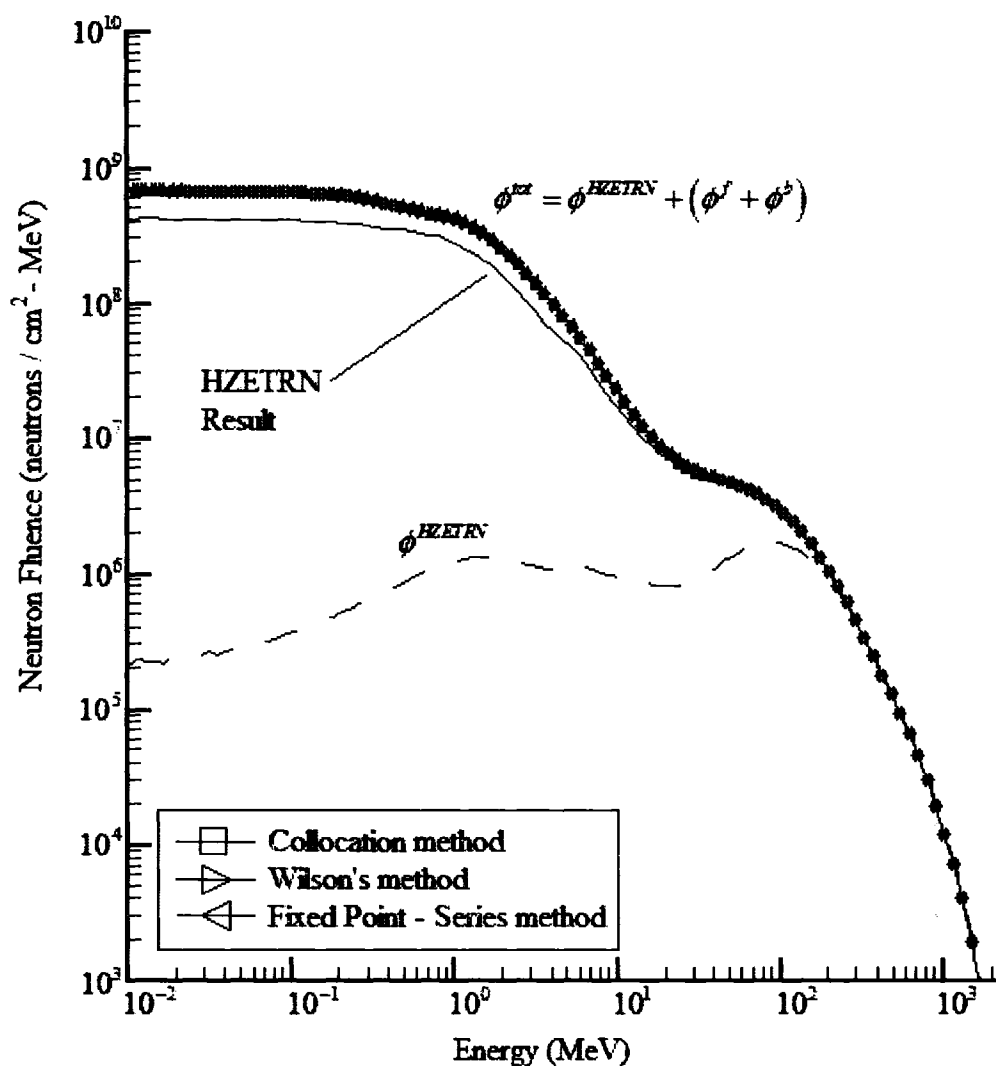
the depth $50 \, gm/cm^2$.

Fig. 25. Neutron fluence at $50\,g/cm^2$ in $100\,g/cm^2$ aluminum target exposed to the February, 1956 SPE.

The three methods are in excellent agreement with one another and display significant improvements over the HZETRN-05 neutron propagator at energies below $20\,MeV$.

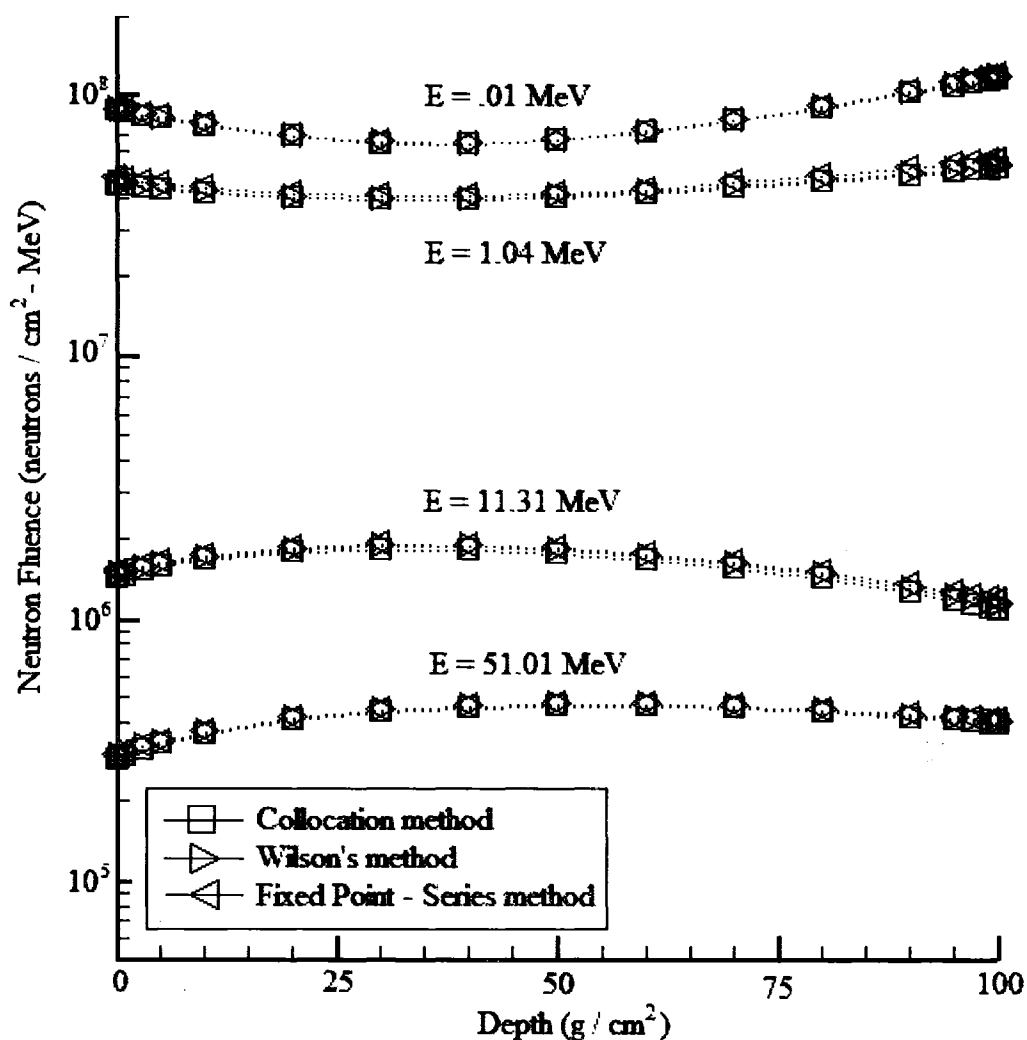Fig. 26 gives neutron fluences for $E = .01, 1.04, 11.31\,MeV$ as a function of depth into the material.

Fig. 26. Neutron fluence as a function of depth for $100\,g\,/\,cm^2$ aluminum target exposed to the February 1956 SPE.

Figs. 25 and 26 show that the methodologies are in excellent agreement for aluminum

targets, regardless of energy or depth.

It was stated in chapter III that the Fixed Point – Series method allowed for

increased physical insight into secondary neutron production. A brief summary of

expected neutron production behavior was also given. Fig. 27 below explicitly shows

some of the individual terms in the series solution for the forward component at a
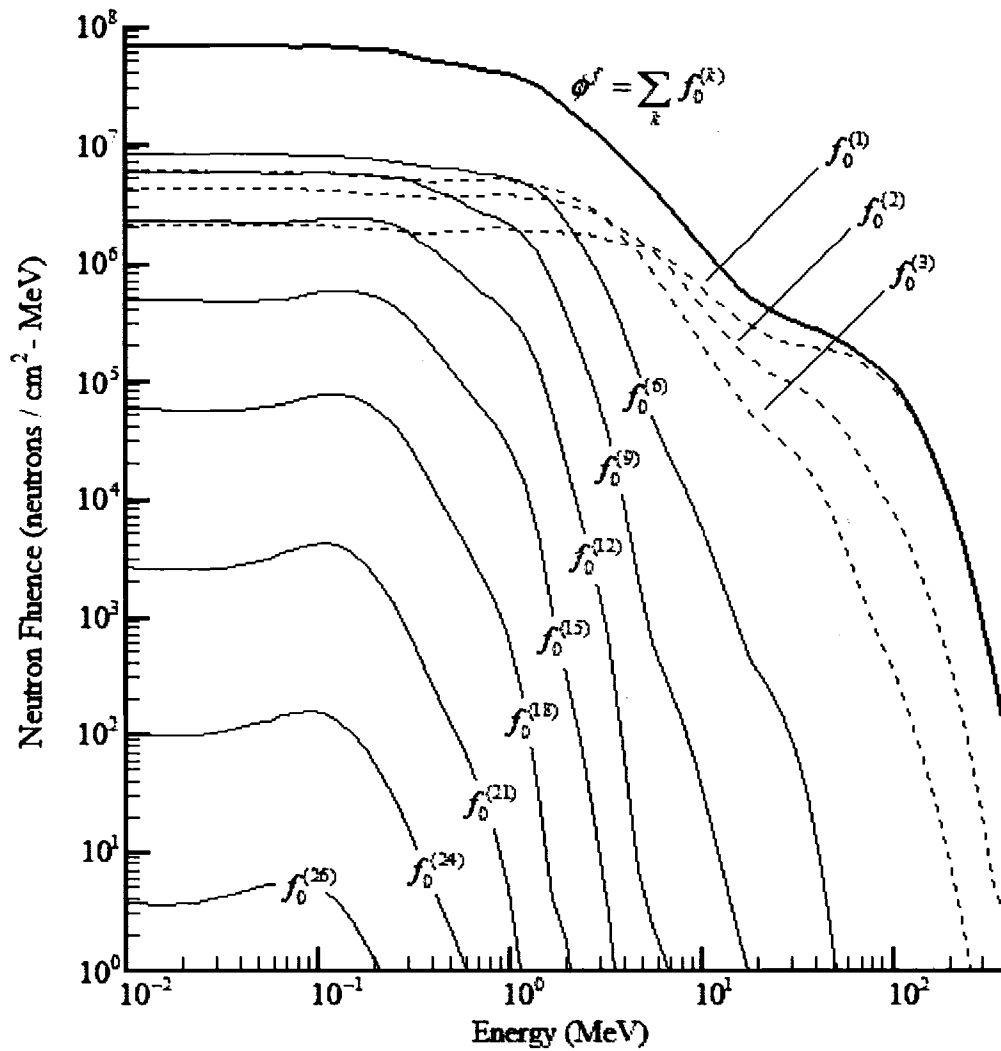
depth of $70\,g/cm^2$ in the aluminum target.

Fig. 27. Terms in series solution of forward component at depth of $70\,g/cm^2$ in $100\,g/cm^2$ aluminum target exposed to the February, 1956 SPE.

First notice that the first generation secondary neutrons $(f_0^{(1)})$ completely dominate

the spectrum above $100\,MeV$. This implies that those first generation particles with energy in $[100\,MeV, 400\,MeV]$ will primarily produce neutrons in the lower energy regimes. It is also clear from the fig. 27 that $f_0^{(k)}$ is a monotonically decreasing function of k for all energies above $100\,MeV$. Conversely, $f_0^{(k)}$ increases as a function of k for all energies below $10\,MeV$ until approximately the sixth or seventh term at which point the trend becomes monotonically decreasing again. This "build up" of low energy neutrons is expected as higher energy neutrons suffer collisions and give up much of their energy. However, at some point the number of high-energy neutrons has decreased sufficiently so that low energy production will decline and the decreasing trend returns. Fig. 28 gives some of the terms in the series solution for the backward component of the fluence at a depth of $70\,g/cm^2$ in the aluminum target.

The physical interpretation of the backward series terms is almost identical to that given above for the forward series terms. What is striking here is the number of terms required for convergence. Fig. 27 shows that it takes 26 terms in the forward series are needed to reach reasonable convergence, while in the backward series it takes only 18. This difference is accounted for by noting the relative depths through which a forward moving neutron and backward moving neutron must propagate to reach $70\,g/cm^2$ in a shield of depth $100\,g/cm^2$. The forward component must propagate the full $70\,g/cm^2$, while the backward component only propagates $30\,g/cm^2$. Note also that the maximum fluence of the forward component is almost a full order of magnitude larger than that of the backward component; hence, many more terms are needed to reach convergence for the forward component at this depth.
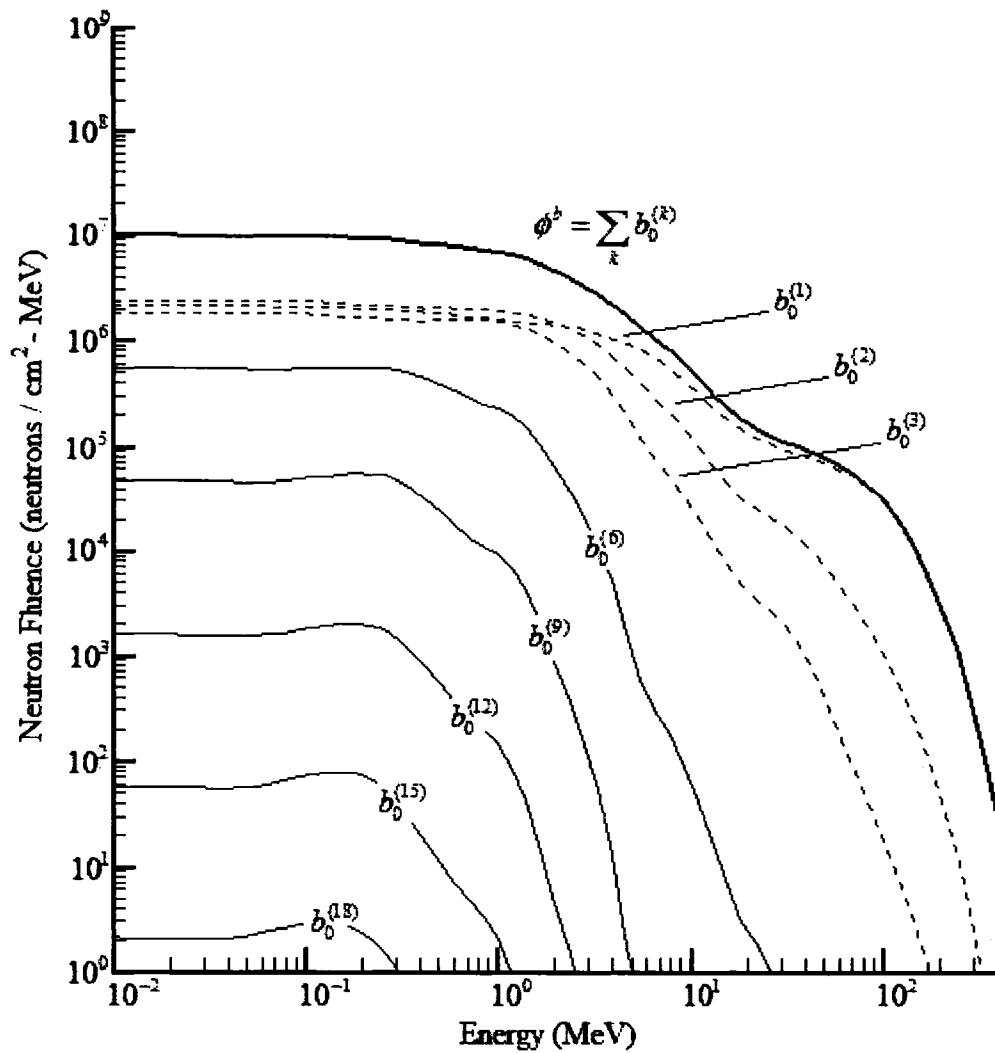
Fig. 28. Terms in series solution of backward component at depth of $70\,g/cm^2$ in $100\,g/cm^2$ aluminum target exposed to the February, 1956 SPE.

Monte Carlo data from reference [34] is available at various depths in a water target exposed to the February 1956 SPE. Maximum depths of the target were not explicitly defined and so the bi-directional model is difficult to compare to this data. Following reference [34], the bi-directional model can be easily modified so that all neutrons are assumed to propagate in the straight-ahead direction only. Recall that the

source term used in the bi-directional model was cut in half so that half of the particles

propagated forward and the other half backward. If one were to assume all of those

particles moved forward, the equation for the backward component of the fluence can

be ignored, and the equation for the forward component would remain with a source

term twice as large as before. It is then easily verified that the factor two will carry

through all of the methods resulting in a forward component that is now twice as large

as before. Figs. 29 - 31 give the results of the three methods under the straight-ahead

approximation for depths of $1 g / cm^2$, $10 g / cm^2$ and $30 g / cm^2$ in a water target
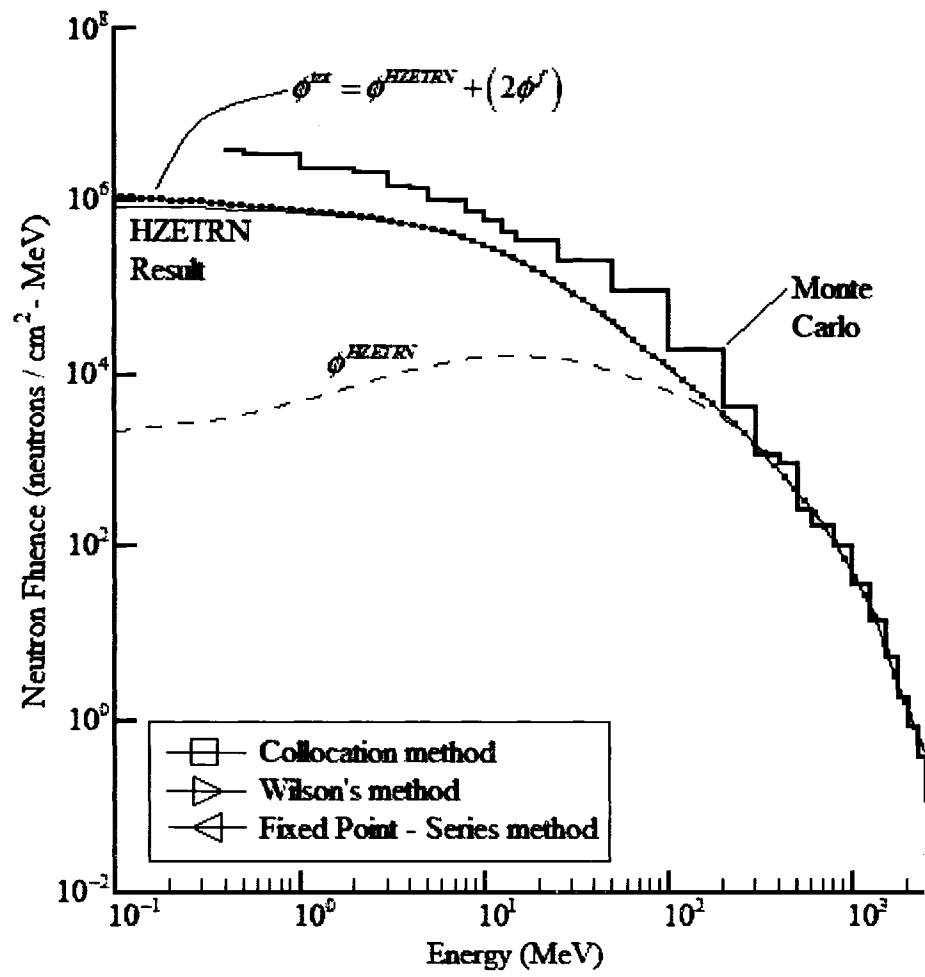
exposed to the February 1956 SPE.

Fig. 29. Straight ahead neutron fluence at $1 g / cm^2$ in water target exposed to the February, 1956 SPE.
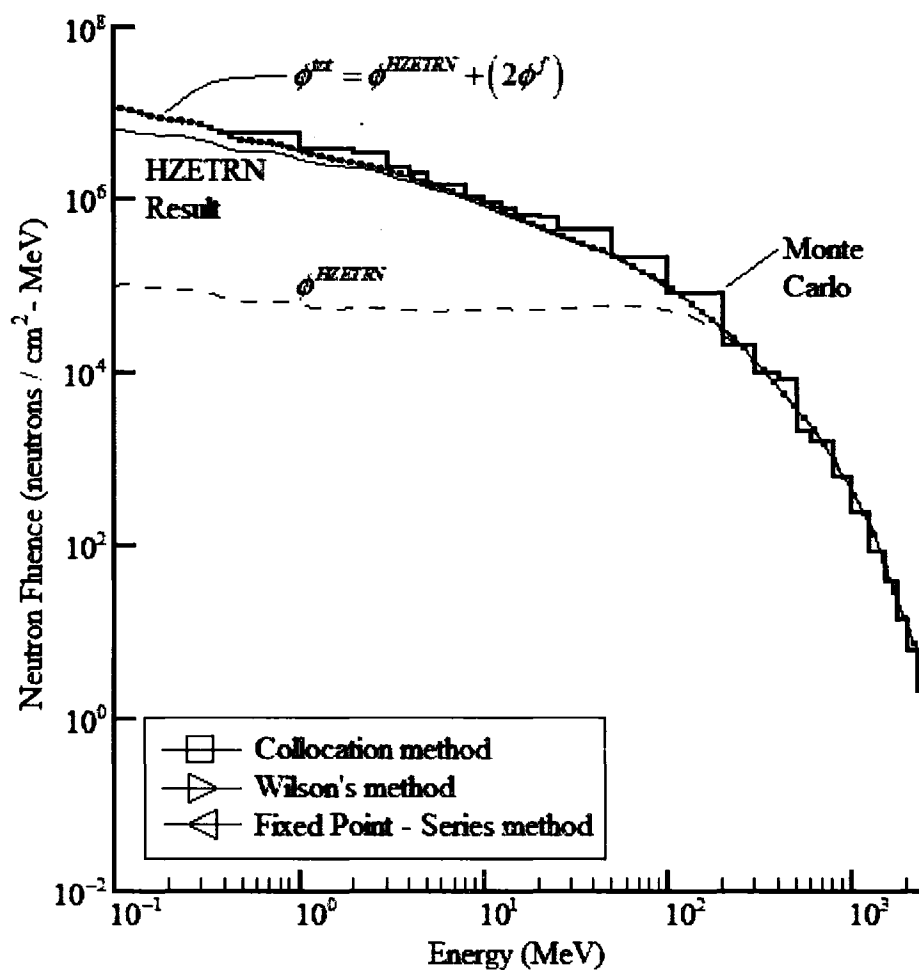
Fig. 30. Straight ahead neutron fluence at $10\,g/cm^2$ in water target exposed to the February, 1956 SPE.
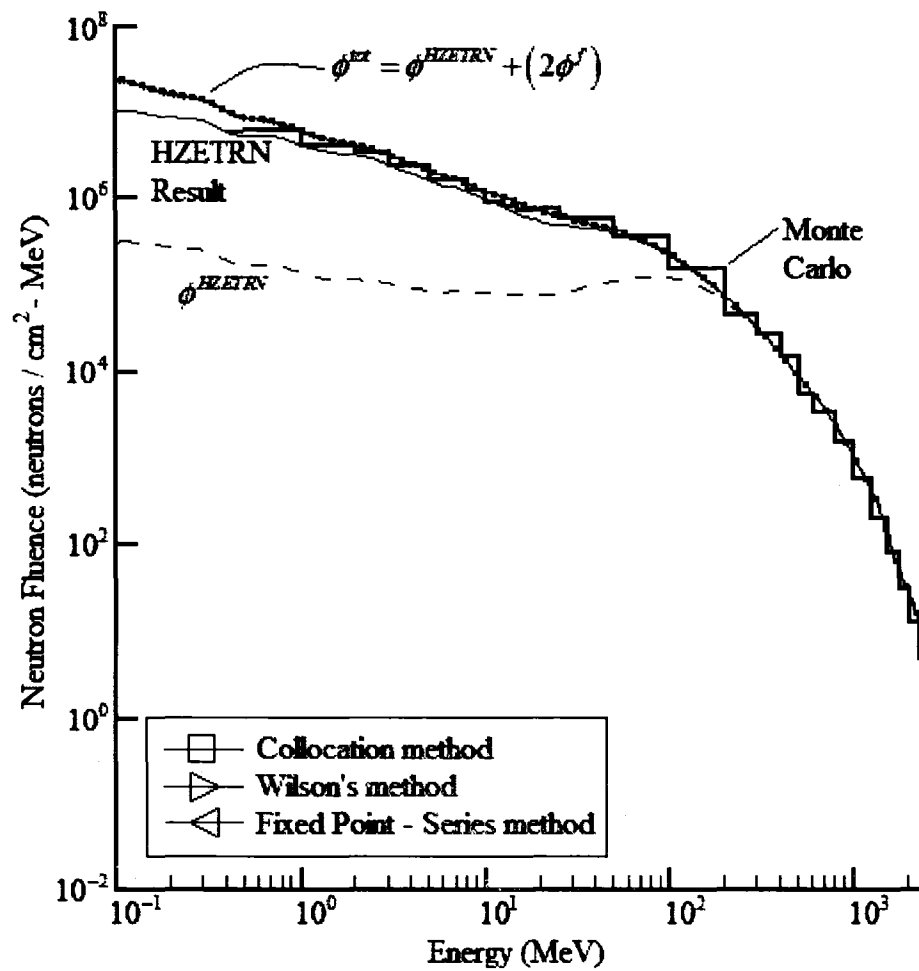
Fig. 31. Straight ahead neutron fluence at $30 \, g/cm^2$ in water target exposed to the February, 1956 SPE.

Figs. 29 - 31 show that the methods are in excellent agreement with one another at the various depths in the water target, and they are in good agreement with the Monte Carlo results except at the depth of $1 \, g/cm^2$. At such small depths, the backward component of the bi-directional model is normally the dominant term (just as the forward component is dominant at large depths in the material), and hence the underestimate is expected since the backward component was neglected for these

comparisons. In order to apply the bi-directional model, maximum depths of

$30\,g/cm^2$ and $100\,g/cm^2$ were chosen. Figs. 32 - 34 give the results at depths of

$1\,g/cm^2$, $10\,g/cm^2$ and $30\,g/cm^2$ in a $30\,g/cm^2$ water target exposed to the

February 1956 SPE.

Fig. 32. Neutron fluence at $1\,g/cm^2$ in $30\,g/cm^2$ water target exposed to the February, 1956 SPE.
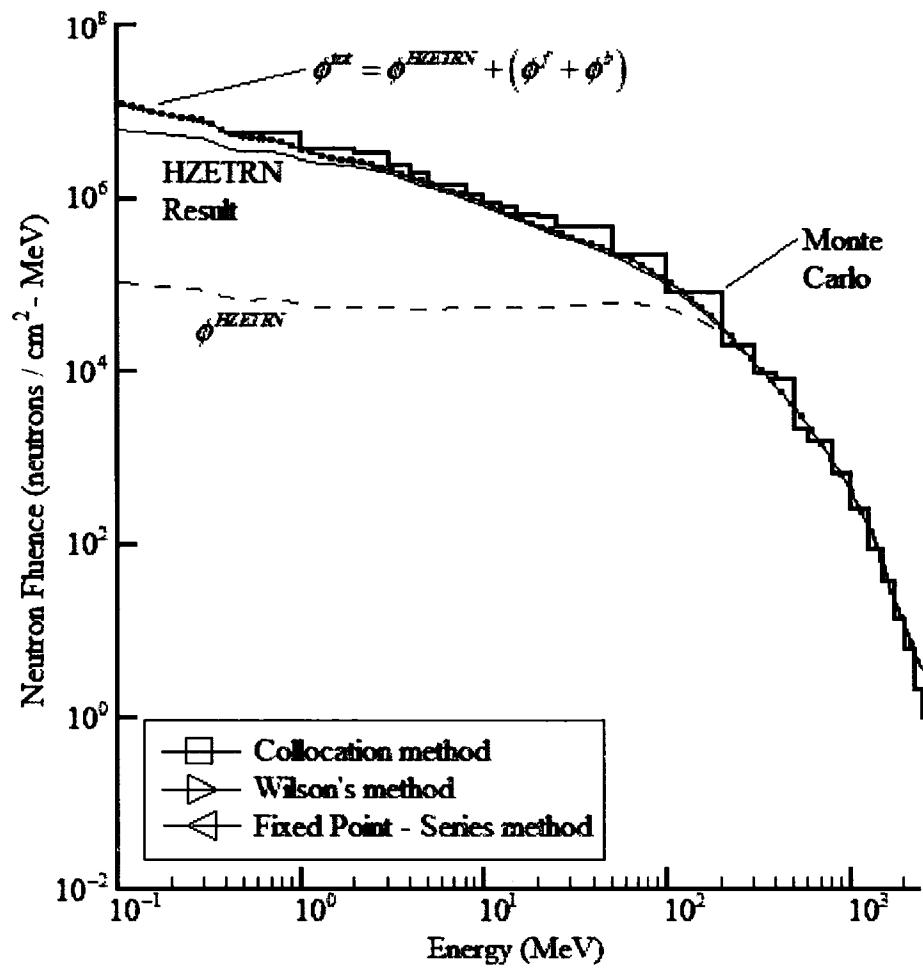
Fig. 33. Neutron fluence at $10\,g/cm^2$ in $30\,g/cm^2$ water target exposed to the February, 1956 SPE.

$$\phi^{tot} = \phi^{HZETRN} + \left(\phi^f\right)$$

HZETRN
Result

Monte
Carlo

ϕ^{HZETRN}

—☐— Collocation method
—▷— Wilson's method
—◁— Fixed Point - Series method

Fig. 34. Neutron fluence at $30\,g/cm^2$ in $30\,g/cm^2$ water target exposed to the February, 1956 SPE.

Figs. 35 - 37 give the results at depths of $1\,g/cm^2$, $10\,g/cm^2$ and $30\,g/cm^2$ in a $100\,g/cm^2$ water target exposed to the February 1956 SPE.
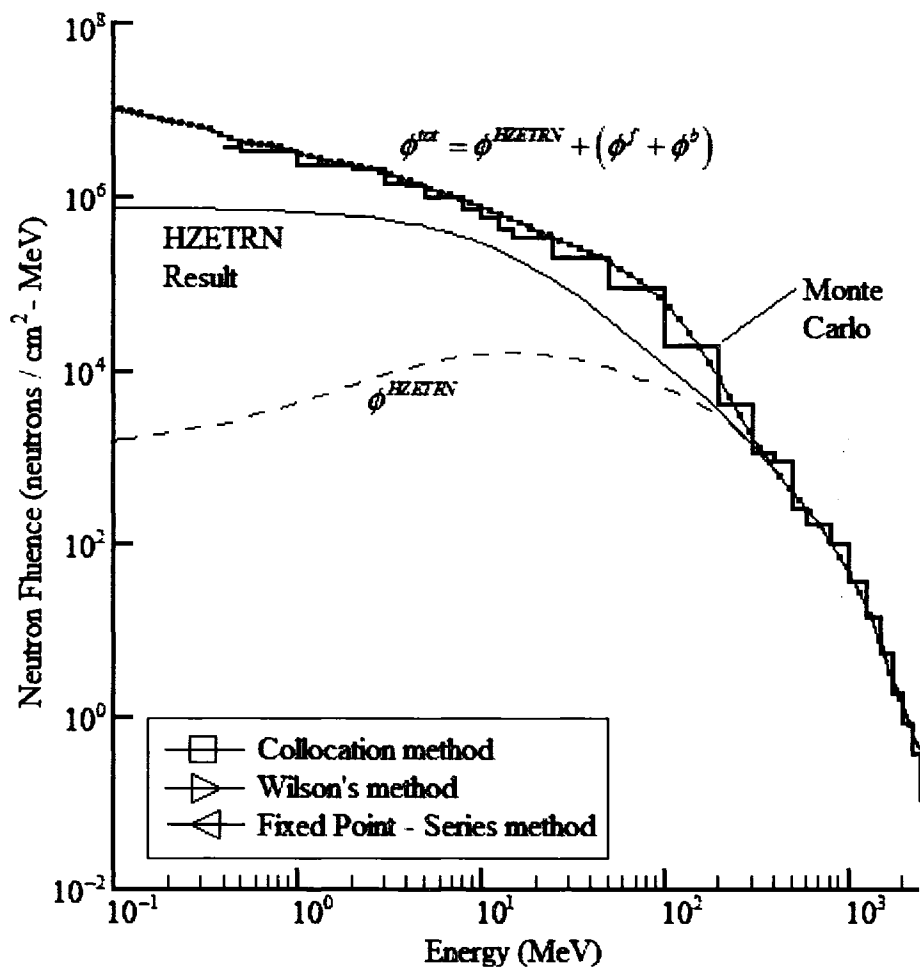
Fig. 35. Neutron fluence at $1 g / cm^2$ in $100 g / cm^2$ water target exposed to the February, 1956 SPE.
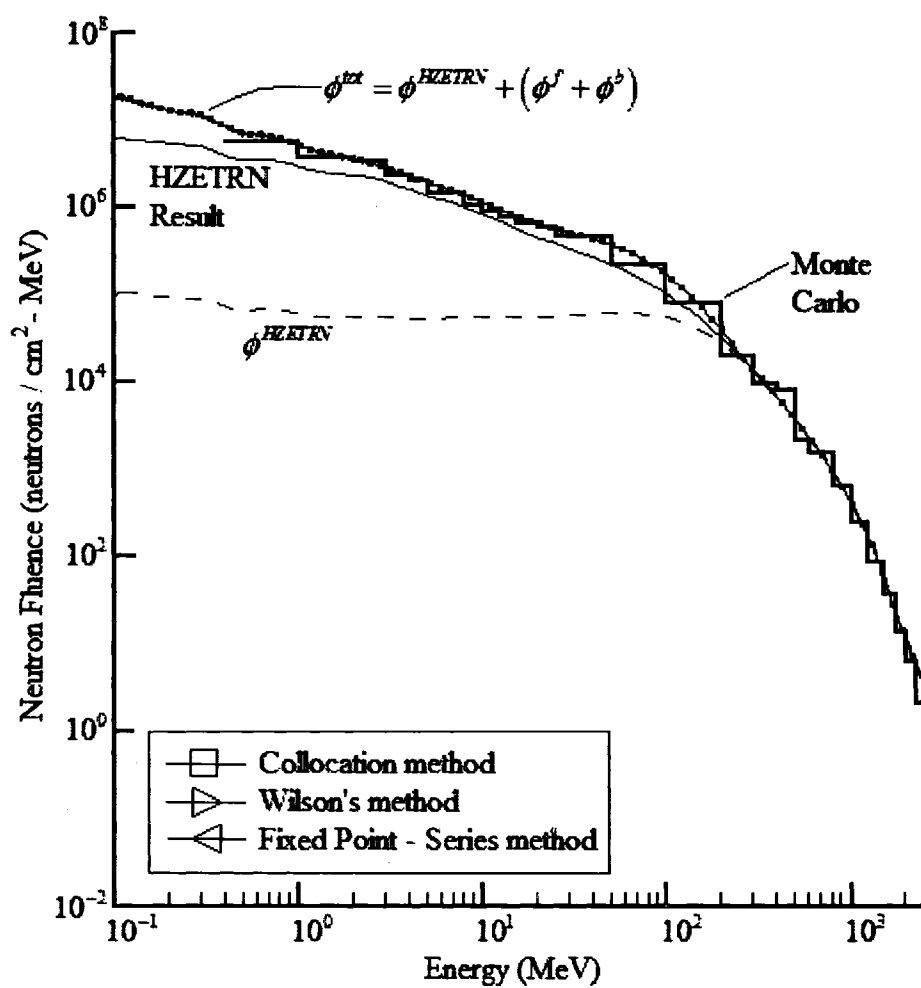
Fig. 36. Neutron fluence at $10\,g/cm^2$ in $100\,g/cm^2$ water target exposed to the February, 1956 SPE.
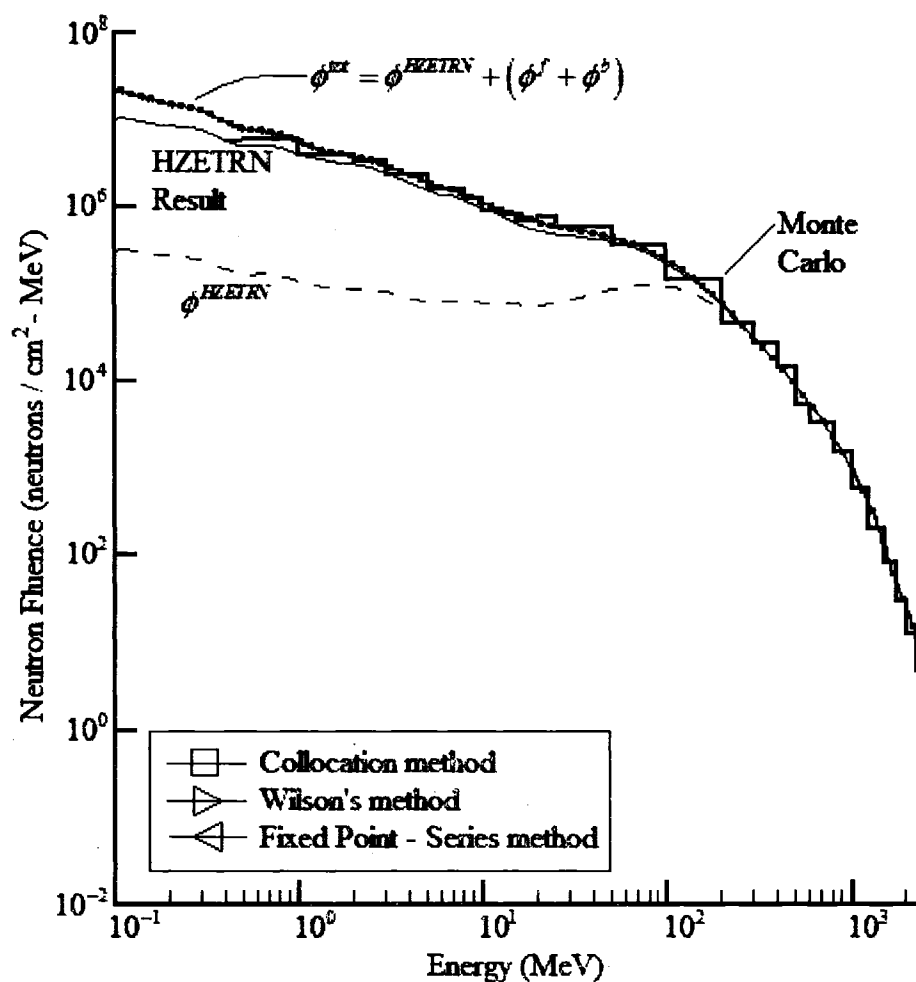
Fig. 37. Neutron fluence at $30\,g/cm^2$ in $100\,g/cm^2$ water target exposed to the February, 1956 SPE.
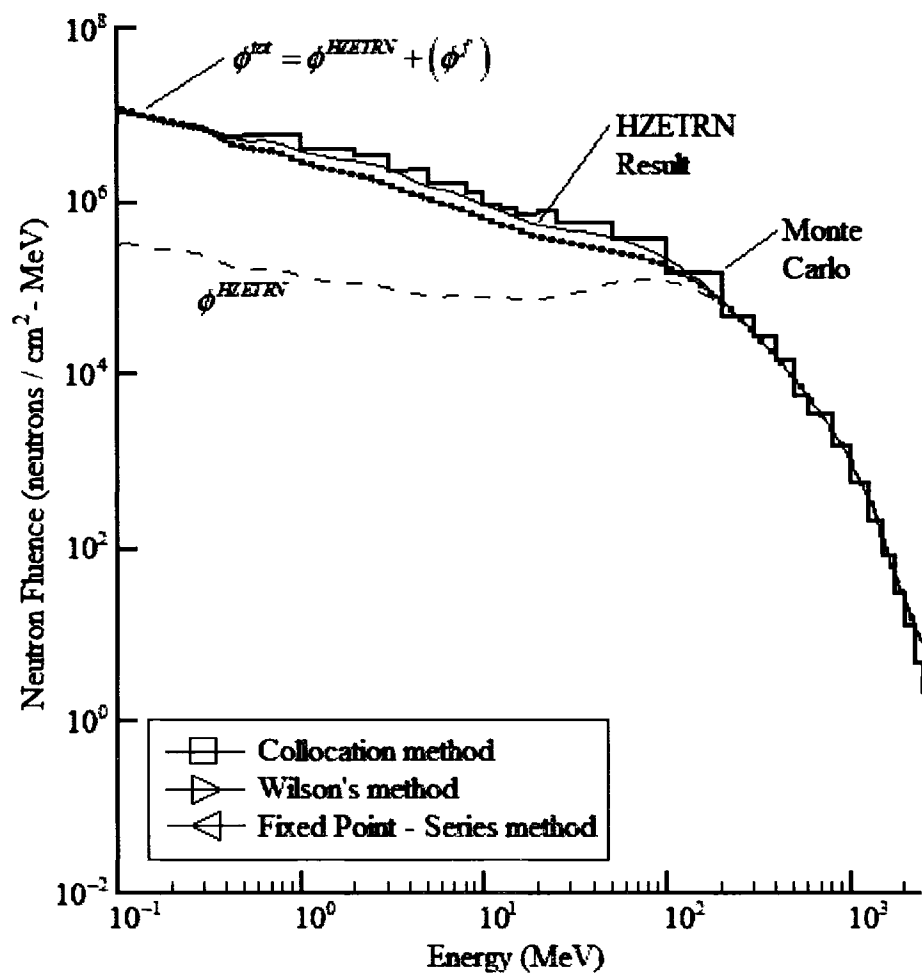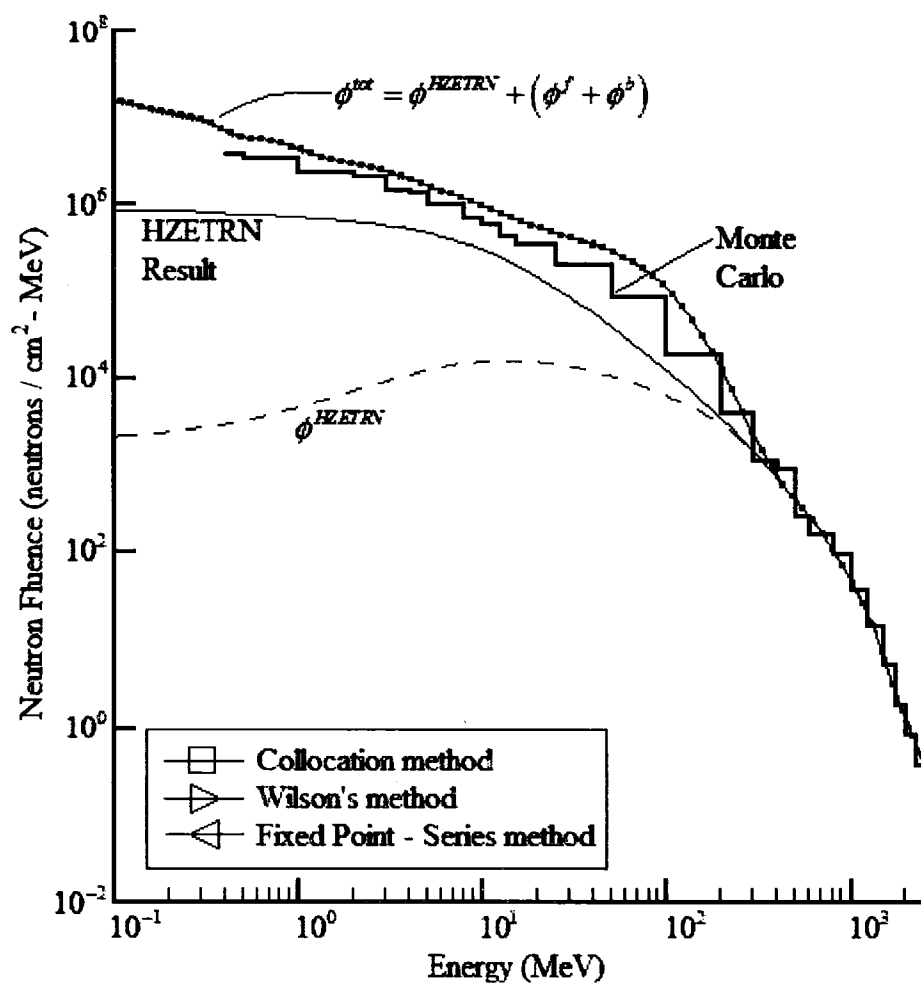
The first conclusion to be drawn from figs. 32 - 37 is that at short depths – where the backward component dominates – the total neutron fluence is highly sensitive to the maximum depth chosen. Though the bi-directional model shows improvements in the total neutron fluence at the depth of $1\,g/cm^2$, fig. 35 (maximum depth of $100\,g/cm^2$) shows that it overestimates the Monte Carlo data while fig. 32 (maximum depth of $30\,g/cm^2$) show that it matches quite well to the Monte Carlo data. The next

conclusion is that at the intermediate depth of $10\,g\,/\,cm^2$, the total neutron fluence

does not seem to be as sensitive to the maximum depth chosen. In fig. 33 (maximum

depth of $30\,g\,/\,cm^2$) the model underestimates Monte Carlo data slightly, while in fig.

36 (maximum depth of $100\,g\,/\,cm^2$) the model is in excellent agreement with Monte

Carlo data. The deviation between the two cases is much smaller this time, and this is

primarily due to the fact that the forward component has grown sufficiently at this

larger depth to now be comparable to the backward component regardless of the

maximum depth chosen. Finally, at the depth of $30\,g\,/\,cm^2$ the model seems highly

sensitive to the maximum depth chosen. Once again, the sensitivity is due to the

backward component at this depth. Recall that the backward component has a

homogenous boundary condition at the right edge of the material and hence at

$30\,g\,/\,cm^2$ in a material of total depth $30\,g\,/\,cm^2$, $\phi^b(30,E) \equiv 0$. Therefore, the total

neutron fluence in fig. 34 underestimates the Monte Carlo data and the "HZETRN-05

Result". In order to adequately use the new methods at this depth, either a larger

maximum depth must be chosen to allow propagation of the backward component, or

a straight-ahead approximation must be used (Fig. 31 shows the new methods to be an

improvement over the current HZETRN-05 neutron propagator when both use the

straight-ahead approximation.). Fig. 37 shows that when a maximum depth of

$100\,g\,/\,cm^2$ is chosen, the bi-directional model matches very well to the Monte Carlo

data at a depth of $30\,g\,/\,cm^2$.

Ultimately, the above analysis verifies that the bi-directional model is highly

sensitive to the maximum depth chosen for positions near the front and back

boundary. However, for intermediate depths, the model is less sensitive and the straight-ahead approximation is also sufficient. Further, figs. 29 - 31 show that the new methods can be altered to operate under the straight-ahead approximation and still provide significant improvements over the current HZETRN-05 neutron propagator.

As before, the methods are now compared as a function of depth for specific energies. The comparison for a $30 \, g / cm^2$ water target exposed to the February 1956 SPE is given in fig. 38, and fig. 39 gives a comparison for a $100 \, g / cm^2$ water target exposed to the February 1956 SPE.
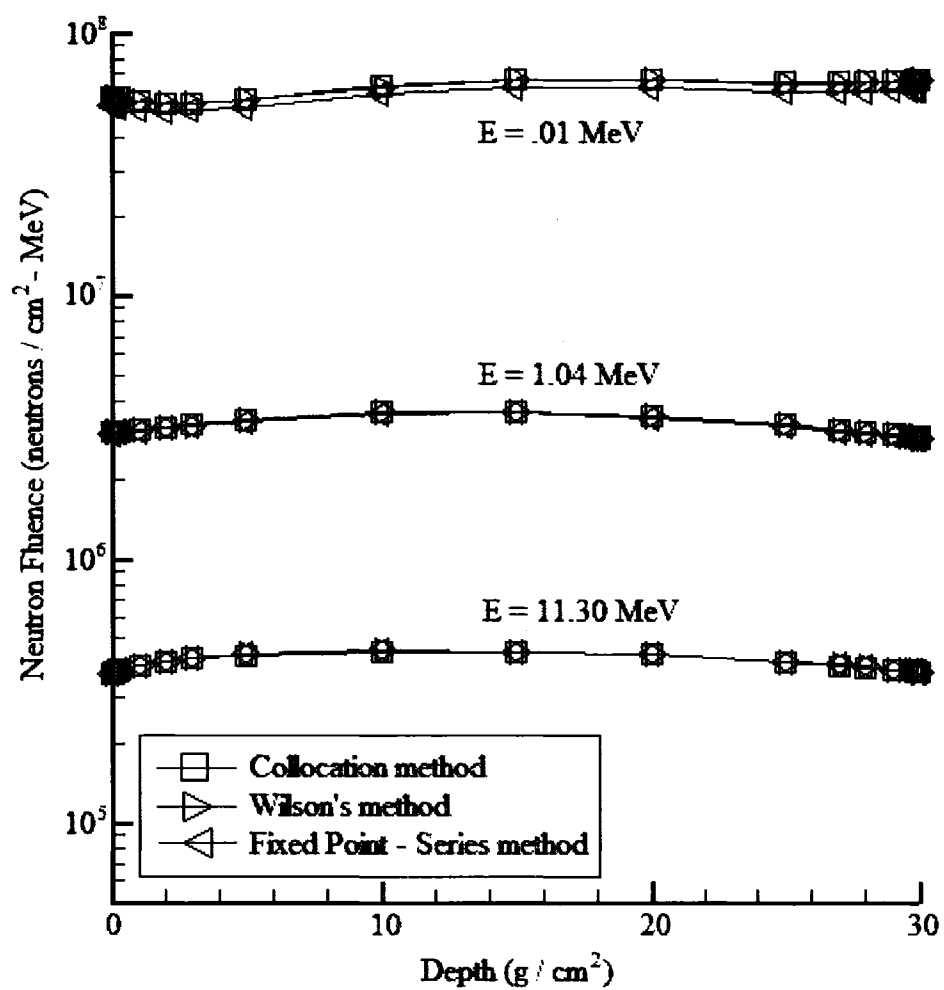
Fig. 38. Neutron fluence as a function of depth for $30\,g\,/\,cm^2$ water target exposed to the February 1956 SPE.
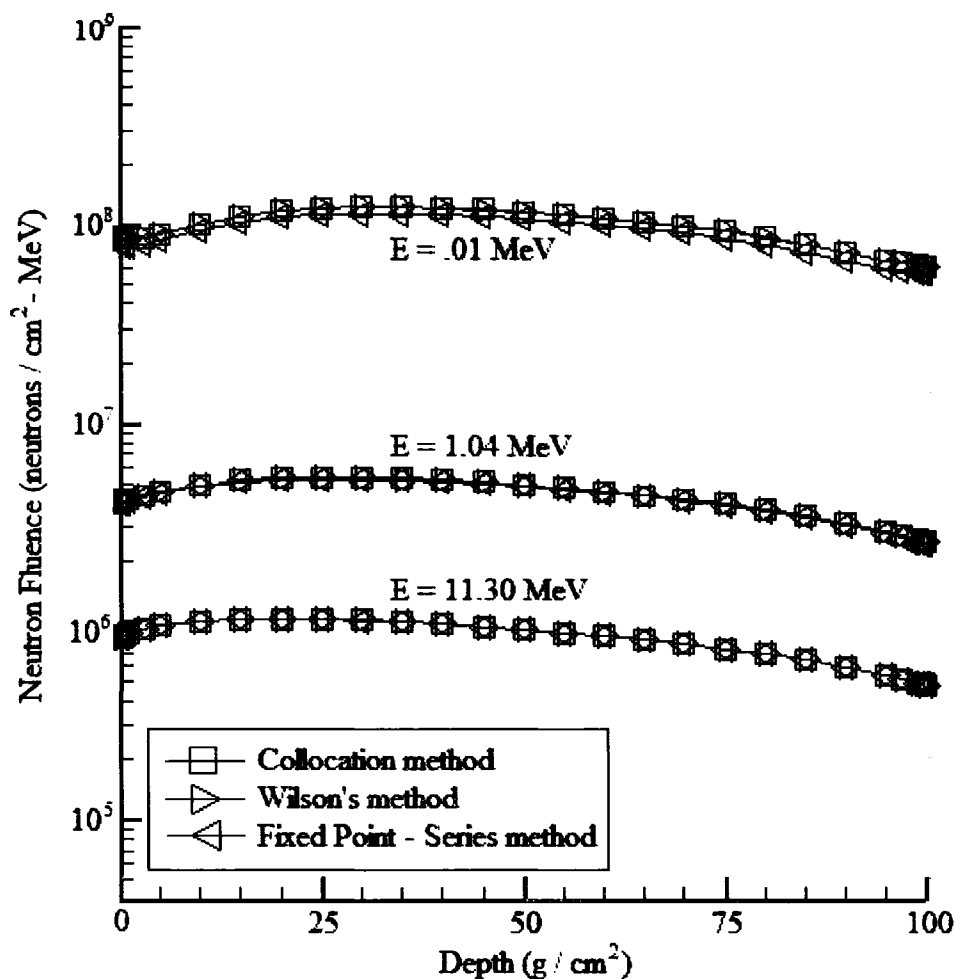
Fig. 39. Neutron fluence as a function of depth for $100\, g/cm^2$ water target exposed to the February 1956 SPE.

The deviation between the methods at the lowest energy $(E = .01\, MeV)$ is striking because fig. 26 above showed them to be in excellent agreement for the aluminum target. Since the external radiation environment was the same in both cases, and the error in figs. 38 and 39 does not exhibit depth dependence, the only conclusion must be that the error was material dependent.

Though it may be difficult to see in the figs. 38 and 39, the Fixed Point –

Series method is underestimating the other two methods at all depths for $E = .01\,MeV$.

To see the cause of the error, consider the form of the source integral for the case of a water target, it is of the form

$$I_{water}(x,E) = \int_E^\infty \left[\sigma_{11,hydrogen}^{re} + \sigma_{11,oxygen}^{re} \right] \phi\, dE'$$
$$+ \int_E^{E/\alpha_{hydrogen}} \sigma_{11,hydrogen}^{el} \phi\, dE' + \int_E^{E/\alpha_{oxygen}} \sigma_{11,hydrogen}^{el} \phi\, dE' \qquad (5.1)$$

where ϕ is some fluence. Since hydrogen has no neutrons in its nucleus, the term

$\sigma_{11,hydrogen}^{re} = 0$; further, since elastic processes dominate at low energies [6], the nuclear

reactive source integral can be dropped as its contribution and error are both

negligible. In this case equation (5.1) simplifies to

$$I_{water}(x,E) = \int_E^{E/\alpha_{hydrogen}} \sigma_{11,hydrogen}^{el} \phi\, dE' + \int_E^{E/\alpha_{oxygen}} \sigma_{11,oxygen}^{el} \phi\, dE' \qquad (5.2)$$

For the elastic collision integrals, the upper limit of integration is dependent on the

fragment energy and the mass of the target; for oxygen $(A_T = 16\,amu)$ and hydrogen

$(A_T = 1\,amu)$ we have

$$\alpha_{oxygen} = \left(\frac{16-1}{16+1} \right)^2 = \left(\frac{15}{17} \right)^2 \approx .779 \qquad (5.3)$$

$$\alpha_{hydrogen} = \left(\frac{1-1}{1+1} \right)^2 = 0 \qquad (5.4)$$

The collision integral is now written as

$$I_{water}(x,E) = \int_E^\infty \sigma_{11,hydrogen}^{el} \phi\, dE' + \int_E^{E/0.779} \sigma_{11,oxygen}^{el} \phi\, dE'$$
$$\equiv I_{hydrogen}(x,E) + I_{oxygen}(x,E) \qquad (5.5)$$

An identical analysis gives the collision integral for an aluminum target as

$$I_{aluminum}(x,E) = \int_{E}^{E/0.862} \sigma^{el}_{11,aluminum} \, \phi \, dE' \tag{5.6}$$

Equations (5.5) and (5.6) suggest that hydrogen target drastically changes the

numerical considerations that must be taken in order to evaluate the elastic collision

integrals. Now, for the Fixed Point – Series method, the integrals (5.5) and (5.6) are

computed explicitly, and hence numerical integration error can be made small by

increasing the number of subintervals over which the Gaussian Quadrature (discussed

in chapter IV) is applied. However, for either of the techniques using a collocation

technique, the source integral for a water target is approximated as

$$\hat{I}_{water}(x,E) = \sum_{k=1}^{N} \phi(x,E_k) \int_{E}^{\infty} \sigma^{el}_{11,hydrogen}(E,E') B_k(E') \, dE'$$
$$+ \sum_{k=1}^{N} \phi(x,E_k) \int_{E}^{E/0.779} \sigma^{el}_{11,oxygen}(E,E') B_k(E') \, dE' \tag{5.7}$$
$$\equiv \hat{I}_{hydrogen}(x,E) + \hat{I}_{oxygen}(x,E)$$

and for an aluminum target

$$\hat{I}_{aluminum}(x,E) = \sum_{k=1}^{N} \phi(x,E_k) \int_{E}^{E/0.862} \sigma^{el}_{11,aluminum}(E,E') B_k(E') \, dE' \tag{5.8}$$

where N is the number of energy points and $B_k(E)$ is the linear basis spline discussed

in chapter III. Consider the special case $\phi(x,E) = Ae^{bE} \equiv f(E)$, with $A = 10^8$ and

$b = -\ln(A)/400$. The exponential curve was chosen since all of the neutron fluence

(or flux) curves displayed exponential decay as a function of energy. Also, the depth

dependence is dropped because the integration is independent of it. The integrals

(5.5), (5.6), (5.7) and (5.8) were then computed with a high degree of accuracy and

error calculations were made according to

$$error_{hydrogen} = \sqrt{\sum_{k=1}^{N} \frac{\left(I_{hydrogen}(E_k) - \hat{I}_{hydrogen}(E_k)\right)^2}{\sqrt{\sum_{k=1}^{N}\left(I_{hydrogen}(E_k) - \hat{I}_{hydrogen}(E_k)\right)^2}}} \qquad (5.9)$$

$$error_{oxygen} = \sqrt{\sum_{k=1}^{N} \frac{}{\sqrt{\sum_{k=1}^{N}\left(I_{oxygen}(E_k) - \hat{I}_{oxygen}(E_k)\right)^2}}} \qquad (5.10)$$

$$error_{aluminum} = \sqrt{\sum_{k=1}^{N} \frac{}{\sqrt{\sum_{k=1}^{N}\left(I_{aluminum}(E_k) - \hat{I}_{aluminum}(E_k)\right)^2}}} \qquad (5.11)$$

Fig. 40 gives the error results for the cases $N = 63, 100, 250, 500, 1000$, and it is

clear that the error for the hydrogen target is considerably larger than that given by

either the oxygen or aluminum targets. This behavior is expected from the type of

approximation made. The collocation integrals (5.7) and (5.8) can be re-arranged to

show that the function ϕ (or f in the special case), is approximated by linear

interpolation across the integration domain. It is well known that the error given by

linear interpolation is $O(E_{k+1} - E_k)$, and so increasing the number of grid points

should reduce the interpolation error [32] for any target material – as shown in fig. 40.

However, for heavy targets, the elastic integration is taken over a very small interval

$(E, E/\alpha)$, and hence the error is not accumulated over the entire spectrum. For

hydrogen, the elastic integration is taken over (E, ∞) so that for very small E the error

induced by the linear interpolation may be quite large. Fig. 40 shows that the error is

controllable in any of the cases by simply increasing the number of collocation points,

but it is important to note that it takes almost approximately 1000 grid points for the

case of a hydrogen target to attain the same error given by an aluminum target with

only 63 grid points. Note that the collocation method results in a square A-matrix

having $N(N+1)/2$ non-zero entries (N is the number of energy grid points), so that if

63 grid points are taken, there will be 2016 non-zero entries in the A-matrix, and if

1000 grid points are taken, there will be 500,500 non-zero entries – almost 250 times
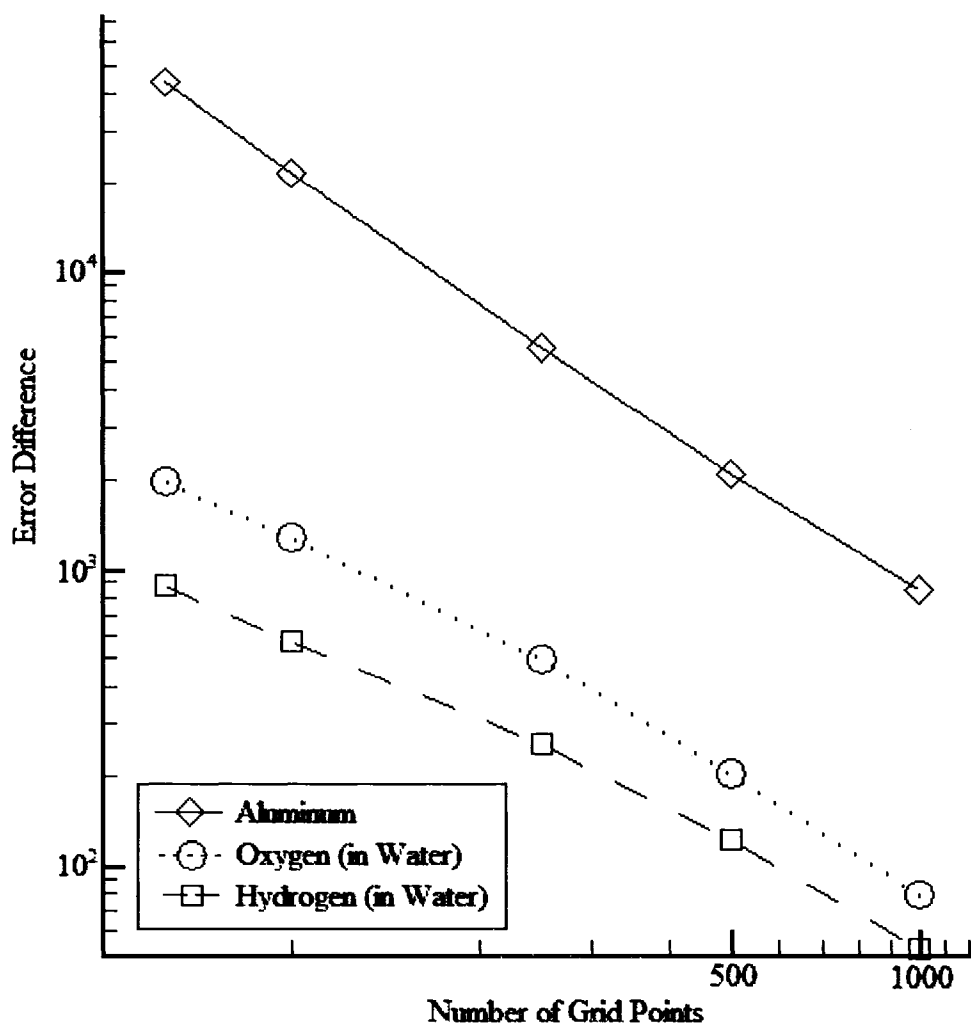
more terms.

Fig. 40. Error differences for aluminum, oxygen, hydrogen targets.

Since run-time is a major consideration when developing deterministic

transport codes, this case was not even considered. However, it can now be concluded

that many grid points are needed to ensure accuracy of the collocation technique. Future work will focus on trying quadratic or cubic splines in the collocation method, as well as analytically determining the error incurred for each of the methods.

The neutron fluence in a two-layer configuration of $100\,g\,/\,cm^2$ of aluminum followed by $100\,g\,/\,cm^2$ of water exposed to the February, 1956 SPE were calculated using the MCNPX Monte Carlo code [35] by Dr. Robert Singleterry at NASA LaRC. Data is also available from reference [30] from the Multi-Group method applied to the exact same non-coupled model used here. Figs. 41 - 44 give the results for various depths in the material.

Fig. 41. Neutron fluence at $1g/cm^2$ ($1g/cm^2$ in the aluminum) in $100g/cm^2$ of aluminum followed by $100g/cm^2$ of water exposed to the February, 1956 SPE.
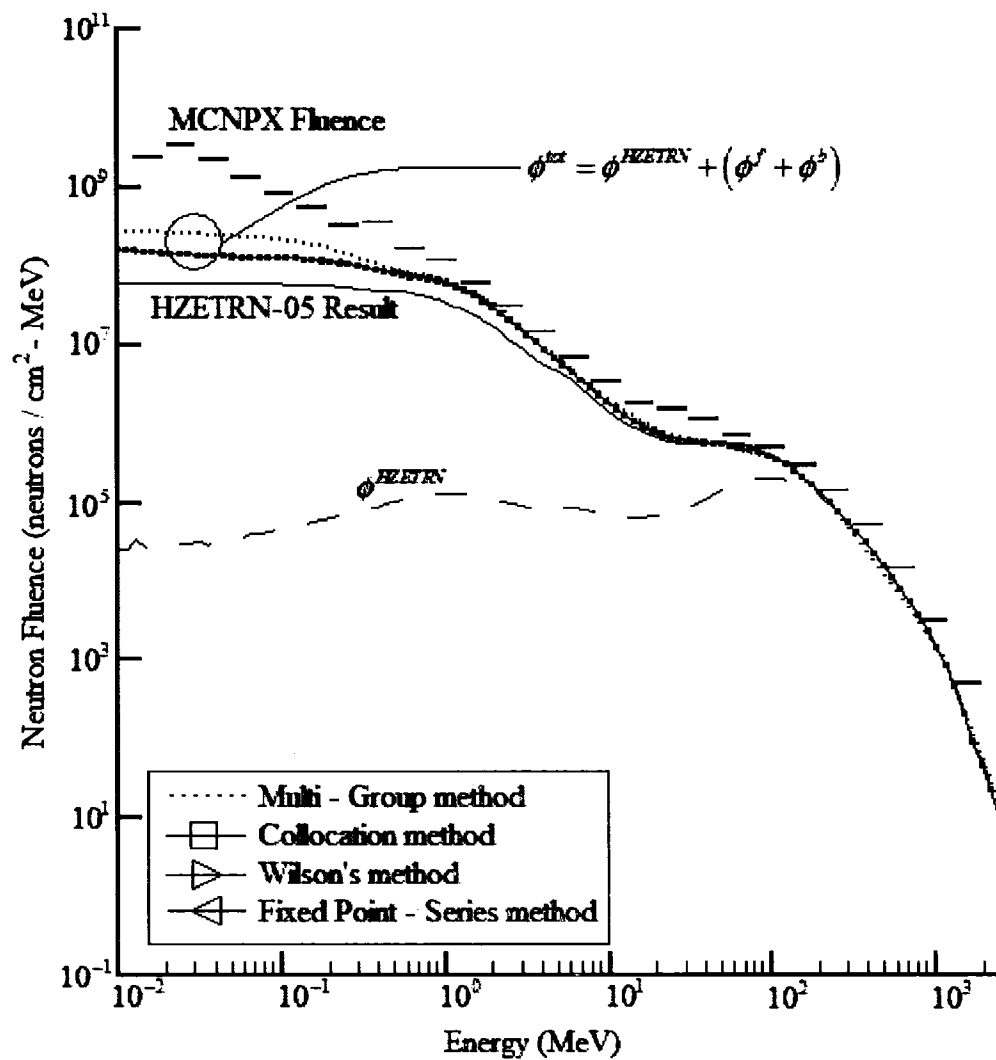
Fig. 42. Neutron fluence at $99\,g/cm^2$ ($99\,g/cm^2$ in the aluminum) in $100\,g/cm^2$ of aluminum followed by $100\,g/cm^2$ of water exposed to the February, 1956 SPE.
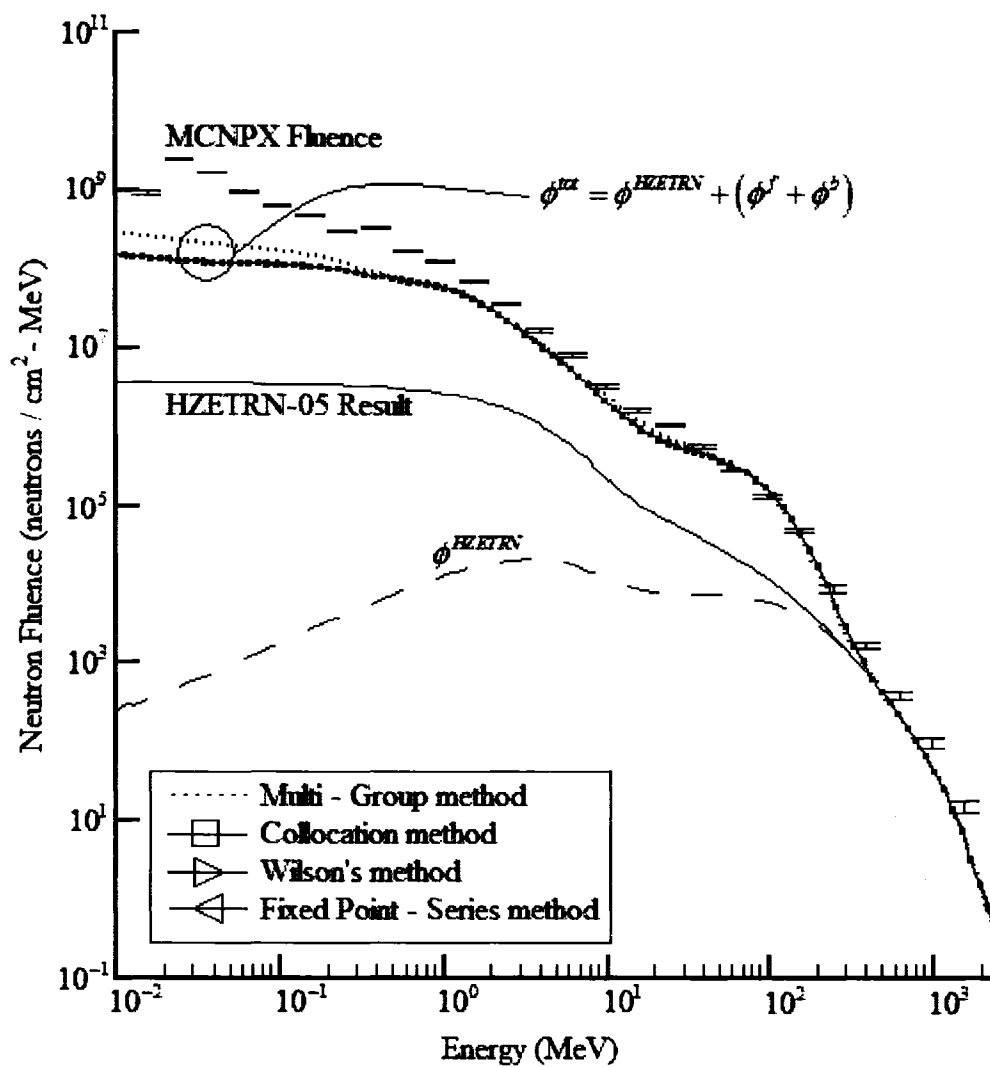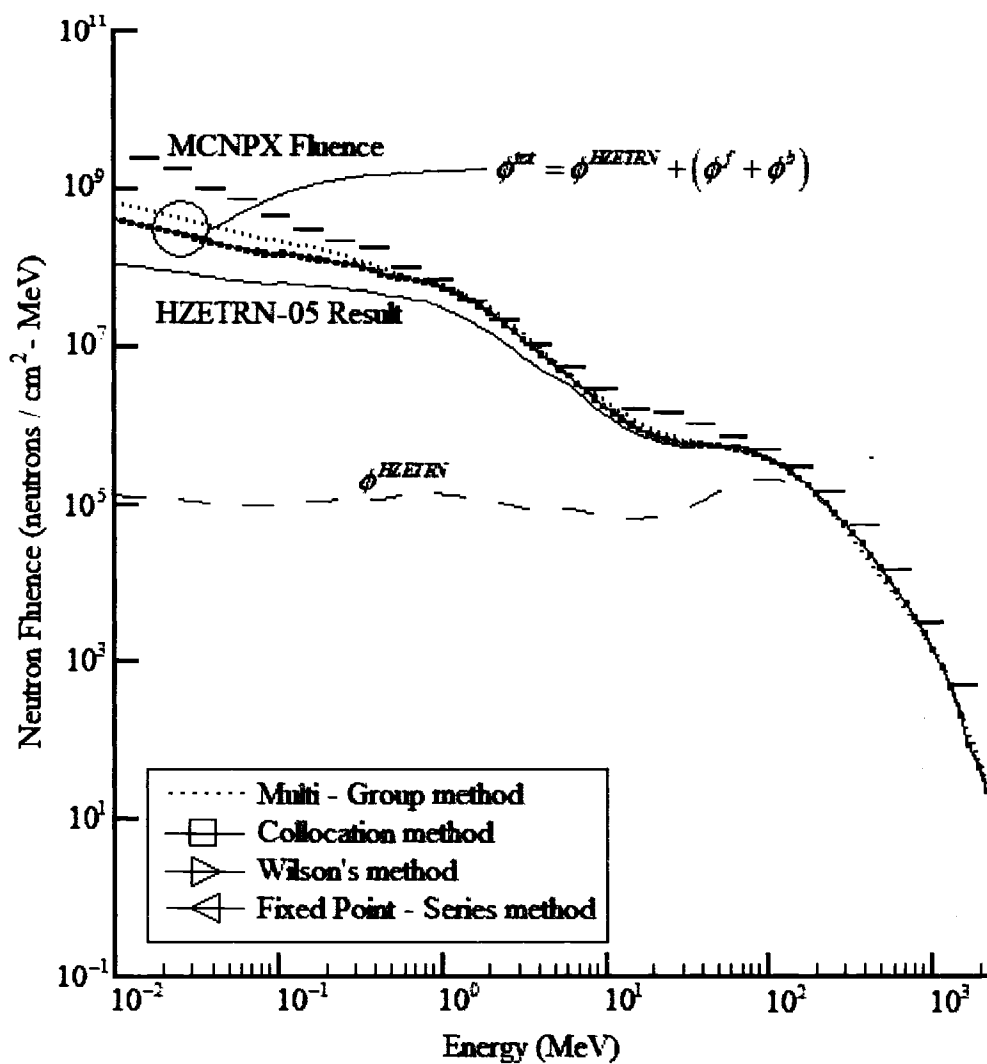
Fig. 43. Neutron fluence at $101 g/cm^2$ ($1 g/cm^2$ in the water) in $100 g/cm^2$ of aluminum followed by $100 g/cm^2$ of water exposed to the February, 1956 SPE.
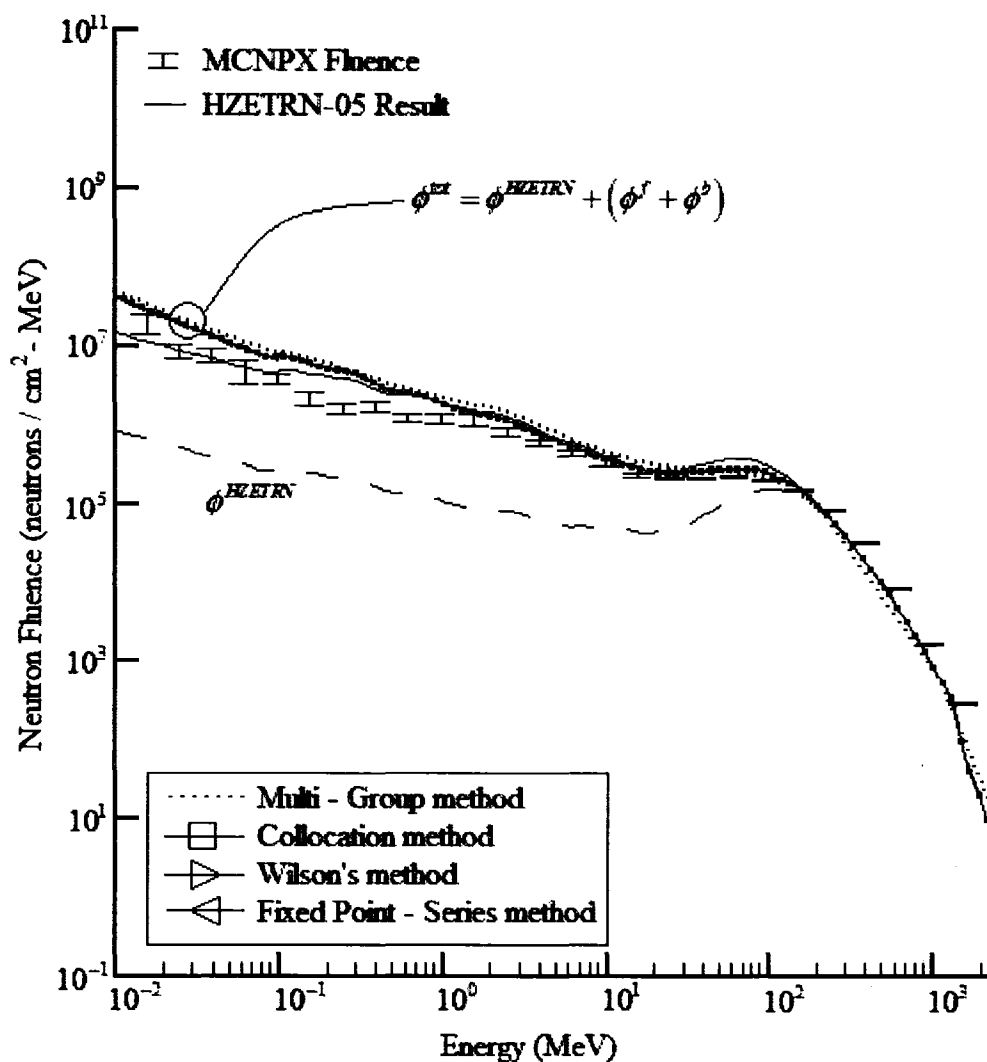
Fig. 44. Neutron fluence at $199\,g/cm^2$ ($99\,g/cm^2$ in the water) in $100\,g/cm^2$ of aluminum followed by $100\,g/cm^2$ of water exposed to the February, 1956 SPE.

First note that for figs. 41 - 44 the portion of the spectrum above $100\,MeV$ is completely dominated by the high-energy straight-ahead component ϕ^{HZETRN} obtained from the HZETRN computer code, and these results are in good agreement with the MCNPX results in all four cases. It is also clear that the portion of the spectrum

between 1 *MeV* and 100 *MeV* is dominated by the bi-directional model where it also is in good agreement with the MCNPX results in all four cases. For the portion of the spectrum less than 1 *MeV*, several things can be said about the deviation between the MCNPX results and the bi-directional model results.

Though the cross-section data is constantly scrutinized and tested, different programs may utilize different databases or interpolation routines and will therefore always account for a certain amount of deviation. Perhaps the largest source of error at energies below 1 *MeV* is the modeling assumption that neutrons propagate in one dimension – whether it is forward or backward. Neutrons at such low energies are expected to be highly isotropic, and it seems as though the bi-directional approximation may not be quite sufficient in such a low energy regime. Though there are discrepancies in the low energy regimes between the MCNPX results and the bi-directional model results, it is clear that the new model certainly improves upon the current HZETRN-05 neutron propagator, and all three methods are still in excellent agreement with one another.

The slight deviation between the Multi-Group method and the three methods presented here can also be explained. The Multi-Group method was implemented into a different version of HZETRN containing slightly different cross-section data and a different SOURCE routine (The SOURCE routine calculates the source terms used in the non-coupled model). Further, only 63 energy grid points were used in the Multi-Group method for the low-energy solution, where the current results were calculated using 100. Noting the results above about the accuracy (or lack thereof) of collocation techniques for targets with significant hydrogen content also implies that 63 grid

points may be insufficient to guarantee reasonable accuracy. The Multi-Group

method also approximates the A-matrix appearing in the Collocation method by using

a Mean Value Theorem for Integrals, which will also account for a certain amount of

the deviation. Ultimately, the four methods are still in good agreement with one

another despite these differences.

Fig. 45 shows the methods as a function of depth for fixed energy values. It is

clear that the continuity condition across the interface between the two materials was

satisfied and reasonable agreement is maintained for all of the methods. The deviation

for $E = .01\,MeV$ in the depths greater than $100\,g\,/\,cm^2$ (water) is explained exactly as

it was for fig. 40.
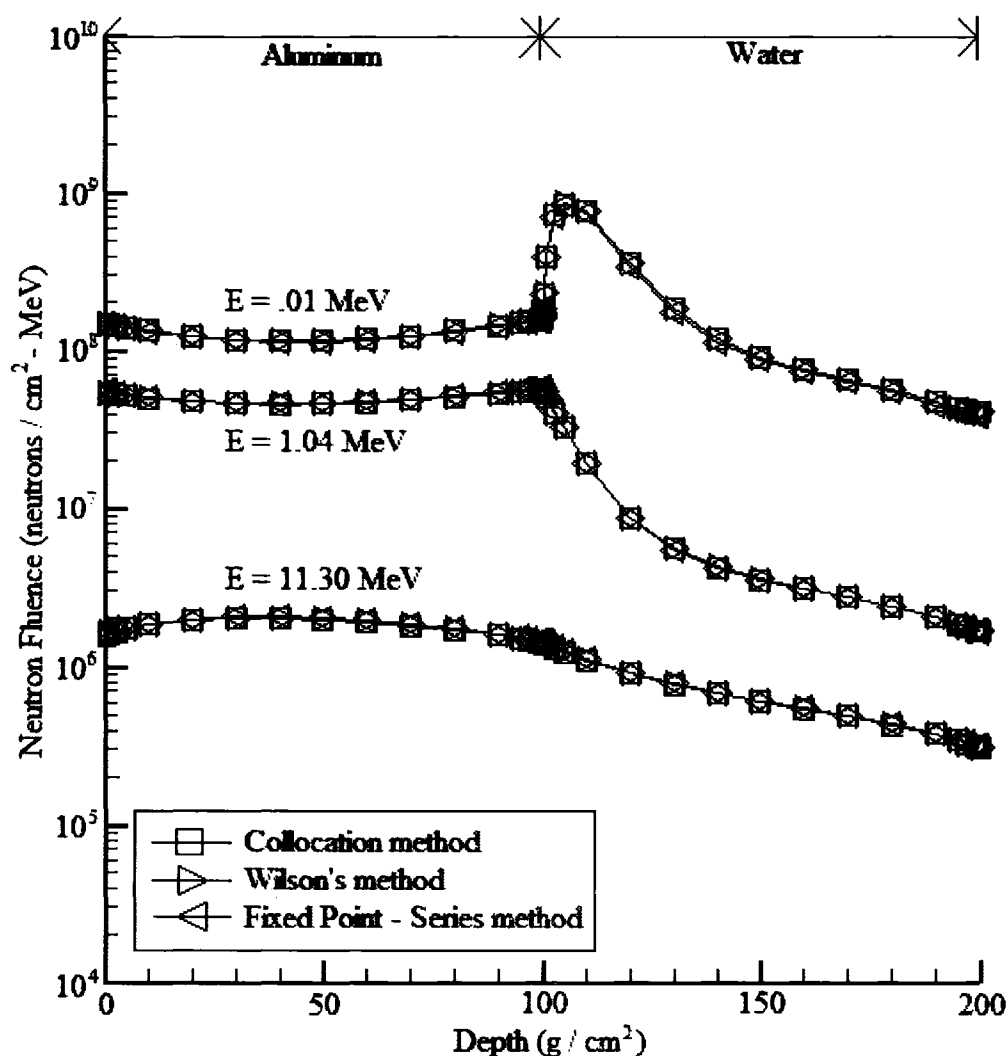
Fig. 45. Neutron fluence as a function of depth for $100\,g/cm^2$ aluminum followed by $100\,g/cm^2$ water exposed to the February 1956 SPE.

ISS AND MIR MONTE CARLO COMPARISONS

The importance of the International Space Station (ISS) and Russian Space station (MIR) to space flight missions has been well established over the past several years. Mars and lunar missions, radiation research and extended human presence in space all currently utilize the ISS or MIR in some way. As such, risk analysis related

to radiation exposure aboard these stations for instrumentation and astronauts is of the utmost importance.

The ISS and MIR space stations maintain an average altitude near 400 km above the earth's surface at an approximate inclination of $51.6°$ to the earth's equator; both stations are considered to be in low earth orbit (LEO) and are therefore affected by galactic cosmic rays (GCR) and trapped radiation (TRP). Of particular interest to LEO studies are the GCR and trapped radiation depicted in fig. 23. Though the flux density of GCR is many orders of magnitude below other types of radiation, the high energies involved have a significant impact on secondary neutron production and are therefore important here. The trapped protons – inner and outer zones – are also of importance here due to the high flux densities and relatively high energies of the trapped protons in the inner zone.

The physical geometry of the stations were both modeled as spheres composed of aluminum 2219, and it was assumed the observer or "detector" would be placed in the center of the sphere. Table 2 gives the elemental composition of the material.

Table 2
Elemental composition of aluminum 2219 by mass percentage.

Element	Mass Percentage
Aluminum	93.0
Copper	6.30
Manganese	0.30
Titanium	0.06
Vanadium	0.10
Zirconium	0.18

Obviously the ISS and MIR geometries are much more complicated than a single cylinder, but the assumption allowed for rapid comparison. The other alternative would be to employ ray trace algorithms available at NASA LaRC that interpolate off large flux tables to approximate the station geometry. The algorithms require knowledge of the observer or detector positioning as well as information about material composition at several points in the station. The source of the Monte Carlo data did not specify this information other than to state that results were averaged over aluminum 2219 depths of $20-40\,g\,/\,cm^2$ [2].

The proton spectrum from the 1990 GCR environment was chosen as the boundary condition for the Monte Carlo simulations using several inclinations ranging from the equator to the poles; the final results were then averaged over all the different inclinations. The trapped spectrum at LEO was also ignored in their study. In order to maintain the spirit of the comparison as a model for the secondary neutron production within the ISS and MIR stations, we chose an altitude of 400 km and an inclination of $51.6\,^{\circ}$ and used only the protons from the 1990 GCR spectrum as boundary condition. Fig. 46 shows the three methods under this space environment for aluminum 2219 target at depths of $20\,g\,/\,cm^2$ in a slab of $40\,g\,/\,cm^2$, $30\,g\,/\,cm^2$ in a slab of $60\,g\,/\,cm^2$ and $40\,g\,/\,cm^2$ in a slab of $80\,g\,/\,cm^2$.
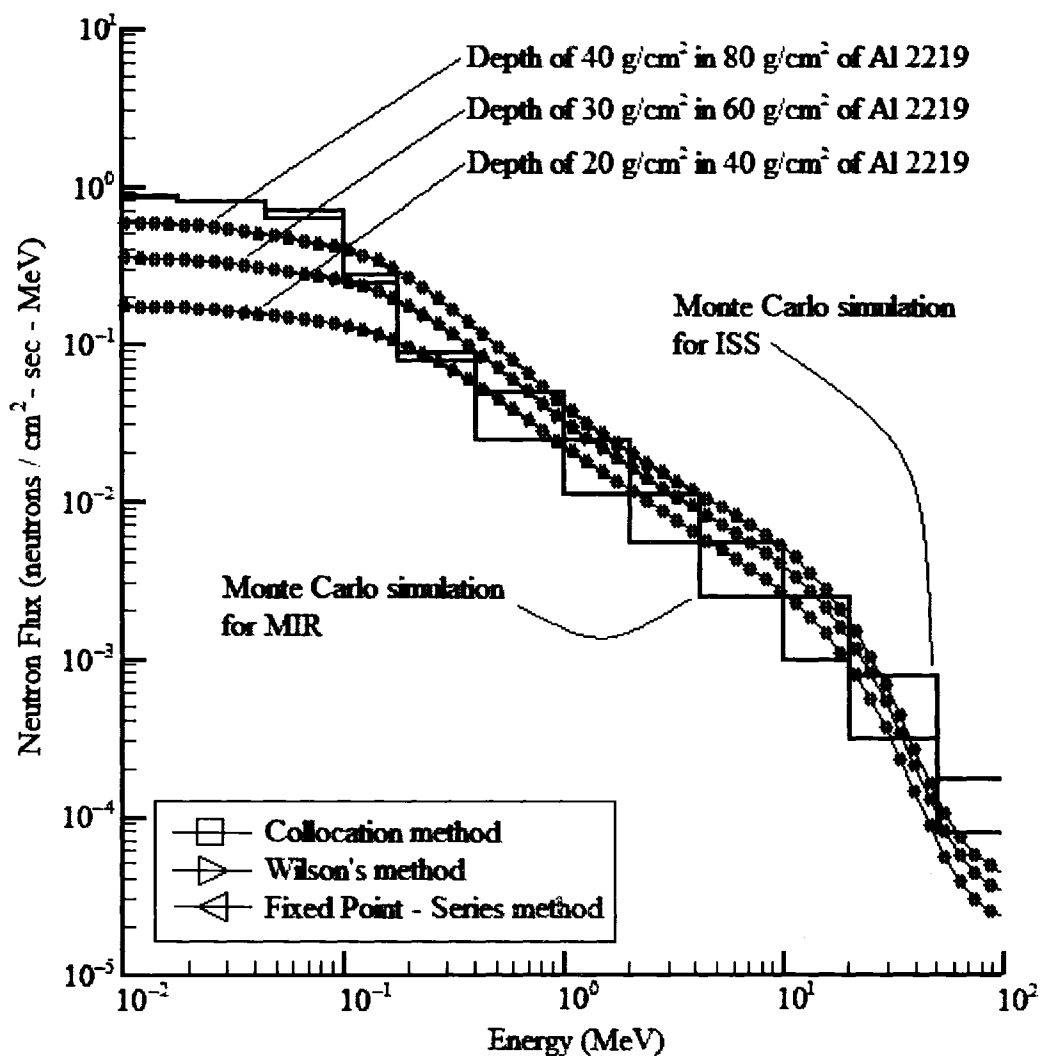
Fig. 46. Neutron flux for various depths of aluminum 2219 exposed to the 1990 GCR proton spectrum.

The depth of $40\,g/cm^2$ in a slab of $80\,g/cm^2$ is in reasonable agreement with the

Monte Carlo data, while the other depths fall short only in the energy region

$E < 1\,MeV$. The primary source of deviation between the Monte Carlo data and the

bi-directional model is due to the input boundary condition. Without specific

knowledge of what inclinations were chosen and how the averaging was carried out in

the Monte Carlo simulation, it is almost impossible to match the data exactly. Other sources of error include the modeling of the station geometry as a sphere and differences in the cross-sections used in each case. Despite the ambiguity in the space environment and possible differences in cross-sections, the bi-directional model is still in good agreement with the Monte Carlo results.

THREE LAYER CONFIGURATION

Neutron flux or fluence data for three layer configurations was not readily available for comparison purposes, and so nominal results are given for arbitrarily chosen environments and shielding configurations. The purpose of these simulations is to ensure agreement of the methods in the more complicated physical system. The first experiment was conducted for $5 g / cm^2$ of polyethylene followed by $40 g / cm^2$ of aluminum 2219 and $5 g / cm^2$ of polyethylene exposed to the same space environment used for the ISS/MIR comparison above. Polyethylene (CH_2) is composed of approximately 33% carbon and 66% hydrogen. The particular configuration was chosen because the ISS is now partially shielded by polyethylene and hence it could be used to model the ISS as a sphere (radius 20) composed of aluminum 2219 with $5 g / cm^2$ of polyethylene as an outer layer shield. Fig. 47 shows the results at a depth of $25 g / cm^2$ in the material.
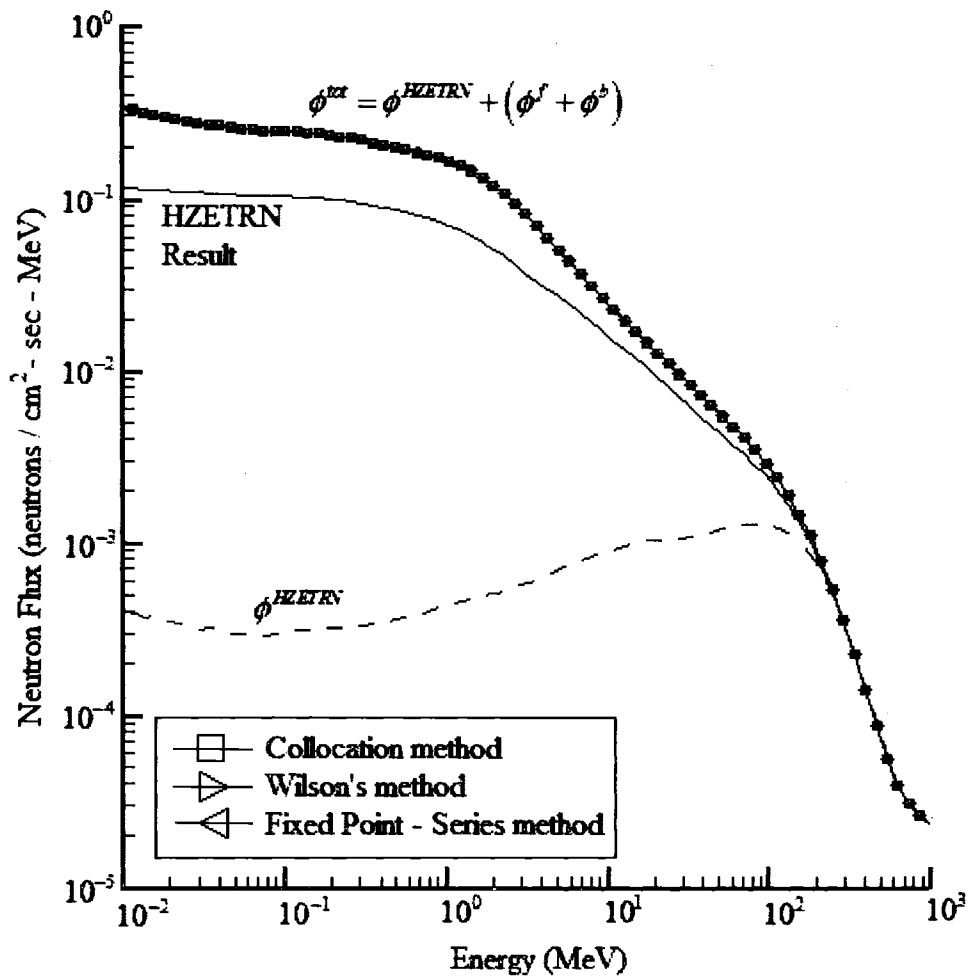
Fig. 47. Total neutron flux at a depth of $25\,g/cm^2$ in $5\,g/cm^2$ polyethylene followed by $40\,g/cm^2$ aluminum 2219 followed by $5\,g/cm^2$ polyethylene target exposed to 1990 GCR proton spectrum.

Fig. 48 gives the total neutron flux as a function of depth for various energies under

the same boundary condition and shielding material defined above.
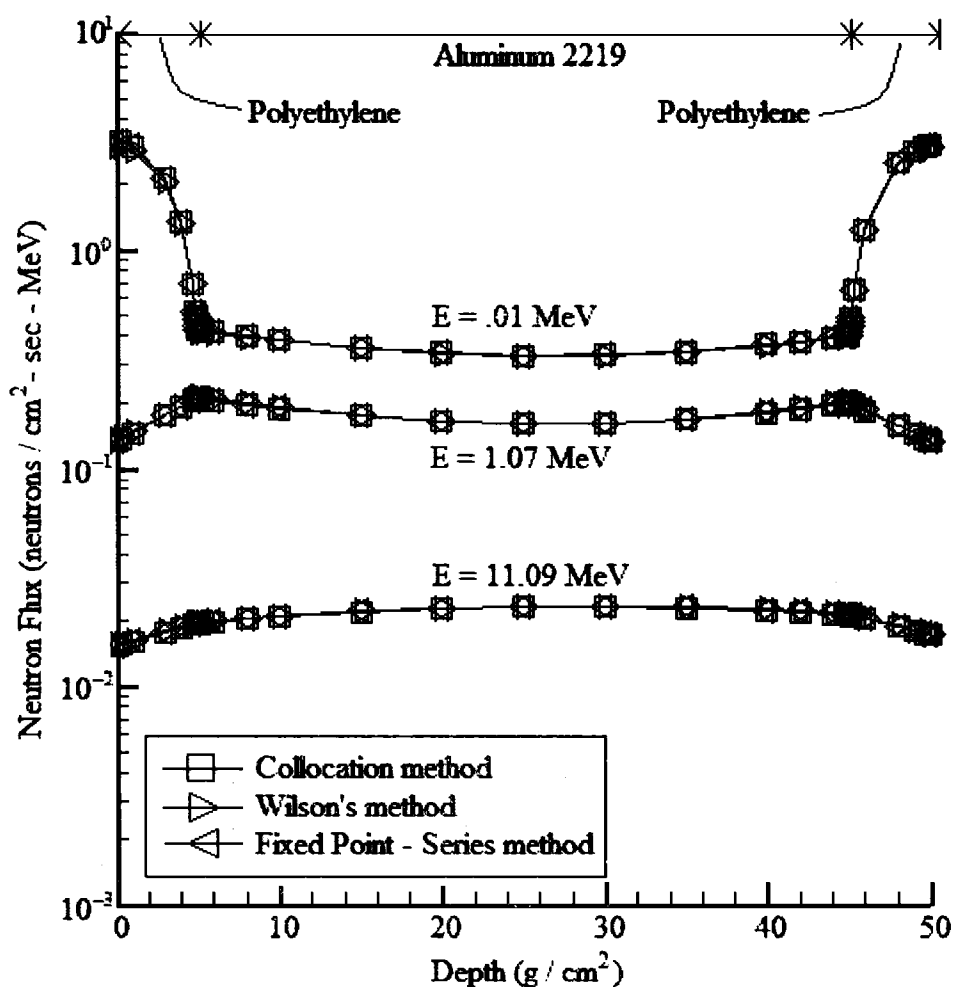
Fig. 48. Neutron flux as a function of depth for $5\,g/cm^2$ polyethylene followed by $40\,g/cm^2$ aluminum and $5\,g/cm^2$ polyethylene target exposed to the 1990 GCR proton spectrum.

The methods are in excellent agreement with one another at all depths and energies in the given three-layer configuration. The slight deviation between the methods at the left and right boundary for $E = .01\,MeV$ is again due to the hydrogen content in polyethylene.

CONCLUSIONS

The solution to the neutron Boltzmann equation was split into a high-energy

straight ahead component and low-energy isotropic component. The decomposition yielded one equation that was solved using HZETRN-05 and a non-coupled system of two equations describing the forward and backward components of the low-energy neutron flux. Three solution techniques were introduced which have applicability to both the coupled and non-coupled systems. The methods are applicable for materials with multiple atomic species and in shielding configurations up to three materials.

The methods were first compared in different shielding materials exposed to the February, 1956 SPE. For the first comparison, an aluminum slab of $100 \, g/cm^2$ was considered and results were given for various depths and energies. The methods were in excellent agreement with one another at all depths and energies in this case. The next comparison was made for a water target for which Monte Carlo data was readily available. The methods were shown to be in reasonable agreement with the Monte Carlo data, and the slight differences between the methods at the lowest of energies was shown to be due to the presence of significant hydrogen content in the shielding material. Finally, the methods were compared to Monte Carlo data in a two-layer configuration. The methods were once again in good agreement with eachother and showed reasonable agreement to the Monte Carlo data and the Multi-Group method.

The next comparison given was to a Monte Carlo simulation of the ISS and MIR station exposed to the proton component of the 1990 GCR spectrum. Though there exist ambiguities in the definition of the boundary condition used for the Monte Carlo simulation, the methods were in reasonable agreement to the data and excellent agreement with one another. A final example of a three-material configuration

exposed to the 1990 GCR spectrum was given to ensure that the methods were applicable in the more complicated shielding configuration. Once again, the methods were in excellent agreement with one another at all depths and energies.

There are several areas of future research that have arisen from this work. First, a detailed error analysis of the Collocation method applied to the non-coupled system will need to be given. A brief discussion of this was given above, and it seems as though the error is minimized as the atomic mass of the target is increased. It will also be necessary to explore the advantages of using higher order splines (quadratic and cubic) and examine the subsequent error response in each case.

Next, direct comparisons of the coupled and non-coupled models will need to be made. Though Feldman dealt with the coupled model using collocation and finite differencing techniques, the reported computational costs far outweighed those of the Mulit-Group method and the methods presented here. The natural question then becomes, does the coupled model provide enough improvement over the non-coupled model to substantiate such cost? This question will need to be considered in a variety of environments and shielding configurations.

REFERENCES

[1]   G. Bush, "A Renewed Spirit of Discovery," 2004,
       <http://www.whitehouse.gov/news/releases/2004/01/20040114-3.html> (15
       February 2007).

[2]   I. Getselev, S. Rumin, N. Sobolevsky, M. Ufimtsev, M. Podzolko, Absorbed
       Dose of Secondary Neutrons from Galactic Cosmic Rays Inside the
       International Space Station, Advances in Space Research 34 (2004), 1429 –
       1432.

[3]   E.R. Benton, E.V. Benton, Space Radiation Dosimetry in Low-Earth Orbit and
       Beyond, Nucl. Instr. and Meth. B 184 (2001), 255 – 294.

[4]   N. Heathcote, Nobel Prize Winners in Physics, Books for Libraries Press,
       Freeport, NY, 1971.

[5]   J.S. Walker, Permissible Dose, University of California Press, Los Angeles,
       CA, 2000.

[6]   J.W. Wilson, L.W. Townsend, W. Schimmerling, G.S. Khandlewal, F. Khan,
       J.E. Nealy, F.A. Cucinotta, L.C. Simonsen, J.L. Shinn, and J.W. Norbury,
       Transport Methods and Interactions for Space Radiation, NASA RP-1257,
       National Aeronautics and Space Administration, 1991.

[7]   R.D. Launius, J.M. Logsdon, R.W. Smith, Reconsidering Sputnik: Forty Years
       Since the Soviet Satellite, Harwood Academic Publishers, Canada, 2000.

[8]   J.G. Roederer, Dynamics of Geomagnetically Trapped Radiation, Springer-
       Verlag, New York, NY, 1970.

[9]   J.W. Wilson, L.W. Townsend, J.E. Nealy, S.Y. Chun, B.S. Hong, W.W. Buck,
       S.L. Lamkin, B.D. Ganapol, F. Khan, and F.A. Cucinotta, BRYNTRN: A
       Baryon Transport Model, NASA TP 2887, National Aeronautics and Space
       Administration, 1989.

[10]   J.L. Shinn, J.W. Wilson, M. Weyland, and F.A. Cucinotta, Improvements in
       Computational Accuracy of BRYNTRN (A Baryon Transport Code), NASA
       TP 3093, National Aeronautics and Space Administration, 1991.

[11]   J.W. Wilson, Analysis of the Theory of High-Energy Ion Transport, NASA TN
       D-8381, National Aeronautics and Space Administration, 1977.

[12] J.W. Wilson, Depth-Dose Relations for Heavy Ion Beams, Virginia J. Sci. 28 (1977), 136 – 138.

[13] J.W. Wilson, Heavy Ion Transport in the Straight Ahead Approximation, NASA TP 2178, National Aeronautics and Space Administration, 1983.

[14] J.W. Wilson, S.Y. Chun, F.F. Badavi, L.W. Townsend, and S.L. Lamkin, HZETRN: A Heavy Ion/Nucleon Transport Code for Space Radiations, NASA TP 3146, National Aeronautics and Space Administration, 1991.

[15] J.W. Wilson, F.F. Badavi, F.A. Cucinotta, J.L. Shinn, G.D. Badhwar, R. Silberberg, C.H. Tsao, L.W. Townsend, R.K. Tripathi, HZETRN: Description of a Free-Space Ion and Nucleon Transport and Shielding Computer Program, NASA TP 3495, National Aeronautics and Space Administration, 1995.

[16] J.H. Heinbockel, M.S. Clowdsley, J.W. Wilson, An Improved Neutron Transport Algorithm for Space Radiation, NASA TP 209865, National Aeronautics and Space Administration, 2000.

[17] L.I. Miroshnichenko, Radiation Hazard in Space, Kluwer Academic Publishers, Boston, MA, 2003.

[18] L.E. Etter, Glossary of Words and Phrases Used in Radiology, Nuclear Medicine and Ultrasound, Charles C Thomas, Springfield, IL, 1970.

[19] J.W. Wilson, F.F. Badavi, M.Y. Kim, M.S. Clowdsley, J.H. Heinbockel, F.A. Cucinotta, G.D. Badhwar, W. Atwell, and S.L. Houston, Natural and Induced Environment in Low Earth Orbit, NASA Tm – 2002-211668, National Aeronautics and Space Administration, 2002.

[20] E.R. Benton, E.V. Benton, A.L. Frank, Neutron Dosimetry in Low-Earth Orbit Using Passive Detectors, Radiat. Meas. 33 (2001), 255-263.

[21] J.H. Heinbockel, Introduction to Tensor Calculus and Contiuum Mechanics, Trafford Publishing, Canada, 2001.

[22] D. Griffiths, Introduction to Elementary Particles, John Wiley & Sons, New York, NY, 1987.

[23] J.R. Kissel, R.L. Ferry, Aluminum Structures, John Wiley & Sons, New York, NY, 2002.

[24] J. Stewart, Calculus: Early Transcendentals, Brooks/Cole Publishing Company, Pacific Grove, CA, 1999.

[25]   M.S. Clowdsley, A Numerical Solution of the Low Energy Neutron Boltzmann Equation, PhD Thesis, Old Dominion University, Norfolk, VA, 1999.

[26]   S. Harris, An Introduction to the Theory of the Boltzmann Equation, Dover Publications, Mineola, NY, 2004.

[27]   G. Feldman, A Forward-Backward Fluence Model for the Low Energy Neutron Boltzmann Equation, PhD Thesis, Old Dominion University, Norfolk, VA, 2003.

[28]   S.L. Lamkin, A Theory for High-Energy Nucleon Transport in One-Dimension, Masters Thesis, Old Dominion University, Norfolk, VA, 1991.

[29]   J.W. Wilson, S.L. Lamkin, Perturbation Theory for Charged-particle Transport in One Dimsion, Nuclear Science and Engineering 57 (1977), 292 - 299.

[30]   M.S. Clowdsley, J.W. Wilson, J.H. Heinbockel, R.K. Tripathi, R.C. Singleterry, J.L. Shinn, An Improved Elastic and Nonelastic Neutron Transport Algorithm for Space Radiation, NASA TP 209865, National Aeronautics and Space Administration, 2000.

[31]   J. Ranft, Lecture 22: The FLUKA and KASPRO Hadronic Cascade Codes, Computer Techniques in Radiation Transport and Dosimetry (1980), 339-371.

[32]   T.C. Slaba, J.H. Heinbockel, J.W. Wilson, S.R. Blattnig, and M.S. Clowdsley, A New Method for Calculating Low Energy Neutron Flux, Proceedings of the International Conference on Environmental Systems, Paper number 2006-01-2149, 2006.

[33]   R.L. Burden, J.D. Faires, Numerical Analysis, Brooks/Cole Publishing Company, Pacific Grove, CA, 2001.

[34]   J.L. Shinn, J.W. Wilson, M.A. Lone, P.Y. Wong, and R.C. Costen, Preliminary Estimates of Nucleon Fluxes in a Water Target Exposed to Solar-Flare Protons: BRYNTRN Versus Monte Carlo Code, NASA TM 4565, National Aeronautics and Space Administration, 1994.

[35]   H.G. Hughes, R.E. Prael, R.E. Little, MCNPX – The LAHET/MCNP code merger, LA-UR-97-4891, Los Alamos National Laboratory, 1997.

APPENDIX

DERIVATION OF THE BOLTZMANN TRANSPORT EQUATION

The Boltzmann transport equation for charged and neutral particles within a shielding material can be summarized as a continuity equation describing how the particles in volume element of six dimensional phase space change with time. There are several ways in which one could arrive at the equation; the derivation given here was drawn from reference [21].

Consider a type j particle with energy E at time t having position

$\mathbf{r} = x\,\hat{\mathbf{e}}_1 + y\,\hat{\mathbf{e}}_2 + z\,\hat{\mathbf{e}}_3$, velocity $\mathbf{v} = v_x\,\hat{\mathbf{e}}_1 + v_y\,\hat{\mathbf{e}}_2 + v_z\,\hat{\mathbf{e}}_3$ moving in the direction of

$\mathbf{\Omega} = \Omega_x\,\hat{\mathbf{e}}_1 + \Omega_y\,\hat{\mathbf{e}}_2 + \Omega_z\,\hat{\mathbf{e}}_3$ as shown in fig. 49.
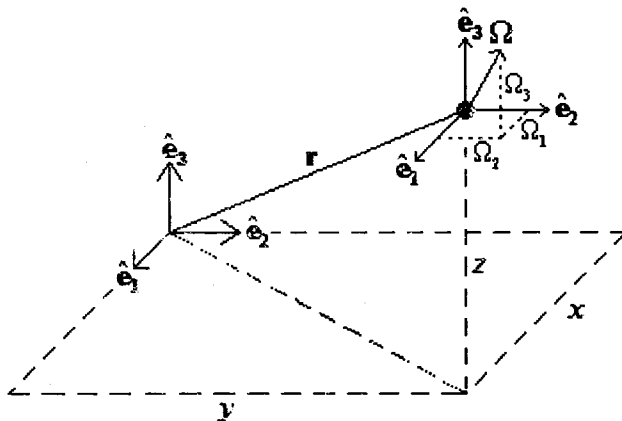

Fig. 49. Position vector and direction of propagation for particle with energy E at time t and velocity $\mathbf{v}$.

Let $d\tau = dx\,dy\,dz$ so that a volume element of phase space can be denoted as

$d\tau\,dE\,d\Omega$ where $d\Omega = \sin(\theta)\,d\theta\,d\psi$ is the solid angle about the direction Ω shown
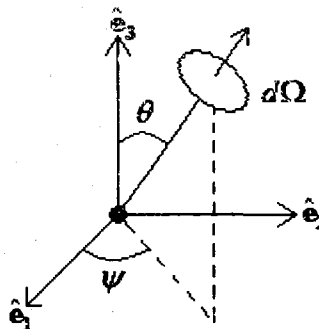
in fig. 50 below.

Fig. 50. Solid angle $d\Omega$ about the direction vector Ω.

Denote the number of type j particles per unit volume per unit energy in the solid

angle $d\Omega$ at time t by $N_j(\mathbf{r},E,\Omega,t)$; the quantity $N_j(\mathbf{r},E,\Omega,t)\,d\tau\,dE\,d\Omega$ represents

the number of particles in a volume element located at the position $\mathbf{r}$ with energy in

$(E,E+dE)$ having direction Ω in the solid angle $d\Omega$ at time t.

The Boltzmann transport equation represents the rate of change of particle

density in the volume element; this rate is written down by considering gains and

losses to the particle density. The only gains are due to external sources $g_j(\mathbf{r},E,\Omega,t)$

and particles scattered into the volume element. To see how particles may be scattered

into the volume element, consider two separate cases. First, suppose a type k

projectile particle enters into the volume element with energy $E' > E$. The projectile

will interact with the target atoms in the volume element and possibly produce type j particles with energy E. Let $\hat{\sigma}_{jk}(E, E', \mathbf{\Omega}, \mathbf{\Omega'})$ denote all those processes by which a type k particle with energy E' and direction $\mathbf{\Omega'}$ suffers a collision or interaction in which is produced a type j particle with energy E moving in the direction of $\mathbf{\Omega}$. The total number of type j particles produced in the volume element per second is

$$\sum_k \int_\Omega \int_E \hat{\sigma}_{jk}(E, E', \mathbf{\Omega}, \mathbf{\Omega'}) \hat{\phi}_k^*(\mathbf{r}, E', \mathbf{\Omega'}, t) \, d\tau \, dE \, d\Omega \, dE' \, d\Omega' \tag{A.1}$$

where $\hat{\phi}_k^*(\mathbf{r}, E', \mathbf{\Omega'}, t)$ is the flux of type k particles at position $\mathbf{r}$ with energy E' moving in the direction of $\mathbf{\Omega'}$ at time t in units of $[particles / cm^2 - sec - MeV - sr]$, and $\hat{\sigma}_{jk}(E, E', \mathbf{\Omega}, \mathbf{\Omega'})$ is referred to as the total macroscopic production cross-section. The particles that are lost from the volume element due to scattering and absorption processes are also expressed in terms of the flux and the quantity $\sigma_j(E)$ as

$$\sigma_j(E) \hat{\phi}_j^*(\mathbf{r}, E, \mathbf{\Omega}, t) \, d\tau \, dE \, d\Omega \tag{A.2}$$

where $\sigma_j(E)$ is the total macroscopic cross-section for a type j particle with energy E.

The rate of change of the number of type j particles in the element of phase space per unit time is now obtained by summing all gains and losses described above. This rate of change is

$$\frac{dN_j}{dt} d\tau \, dE \, d\Omega = \sum_k \int_\Omega \int_E \hat{\sigma}_{jk}(E, E', \mathbf{\Omega}, \mathbf{\Omega'}) \hat{\phi}_k^*(\mathbf{r}, E', \mathbf{\Omega'}, t) \, d\tau \, dE \, d\Omega \, dE' \, d\Omega'$$
$$-\sigma_j(E) \hat{\phi}_j^*(\mathbf{r}, E, \mathbf{\Omega}, t) \, d\tau \, dE \, d\Omega \tag{A.3}$$
$$+g_j(\mathbf{r}, E, \mathbf{\Omega}, t) \, d\tau \, dE \, d\Omega$$

The chain rule can be used to expand $\dfrac{dN_j}{dt}$ as

$$\frac{dN_j}{dt} = \frac{\partial N_j}{\partial t} + \frac{\partial N_j}{\partial x}\frac{\partial x}{\partial t} + \frac{\partial N_j}{\partial y}\frac{\partial y}{\partial t} + \frac{\partial N_j}{\partial z}\frac{\partial z}{\partial t}$$
$$+ \frac{\partial N_j}{\partial v_x}\frac{\partial v_x}{\partial t} + \frac{\partial N_j}{\partial v_y}\frac{\partial v_y}{\partial t} + \frac{\partial N_j}{\partial v_z}\frac{\partial v_z}{\partial t}$$

(A.4)

which can be re-written in the compact form

$$\frac{dN_j}{dt} = \frac{\partial N_j}{\partial t} + \mathbf{v}\cdot\nabla_r N_j + \frac{\mathbf{F}}{m}\cdot\nabla_v N_j$$

(A.5)

where $\mathbf{F}$ is any force acting on the particle and m is it's mass. The special case

$$\frac{dN_j}{dt} = 0 \quad (gains = losses) \text{ gives}$$

$$\frac{\partial N_j}{\partial t} + \mathbf{v}\cdot\nabla_r N_j + \frac{\mathbf{F}}{m}\cdot\nabla_v N_j = 0$$

(A.6)

which is known as the Liouville equation. Further, if the velocities of the particles are

constant, then

$$\hat{\phi}_j^*(\mathbf{r},E,\mathbf{\Omega},t) = \frac{1}{v}N_j(\mathbf{r},E,\mathbf{\Omega},t)$$

(A.7)

so that the Boltzmann equation is now written

$$\frac{1}{v}\frac{\partial}{\partial t}\hat{\phi}_j^* + \mathbf{\Omega}\cdot\nabla_r\hat{\phi}_j^* + \sigma_j(E)\hat{\phi}_j^*(\mathbf{r},E,\mathbf{\Omega},t) =$$

$$\sum_k \int_\Omega \int_E \hat{\sigma}_{jk}(E,E',\mathbf{\Omega},\mathbf{\Omega}')\hat{\phi}_k^*(\mathbf{r},E',\mathbf{\Omega}',t)dE'd\mathbf{\Omega}' \qquad (A.8)$$

$$+ g_j(\mathbf{r},E,\mathbf{\Omega},t)$$

The form of the Boltzmann equation in equation A.8 is further simplified in chapter II

so that a model equation for bi-directional neutron transport can be deduced.

VITA

Tony Charles Slaba

Department of Computational and Applied Mathematics

Old Dominion University

4700 Elkhorn Ave.

Norfolk, VA 23529

Education

Old Dominion University, PhD Computational and Applied Mathematics, May 2007.

Old Dominion University, B.S. Computational and Applied Mathematics, May 2003.

Publications

T.C. Slaba, J. Heinbockel, et.al., "A New Method for Calculating Low Energy Neutron Flux," Proceedings of the SAE International Conference on Environmental Systems, June 2006. Document Number 2006-01-2149.

T.C. Slaba, J. Heinbockel, et.al., "Comparison of Numerical Solution Techniques for Calculating Low Energy Neutrons," Proceedings of the SAE International Conference on Environmental Systems, July 2007.

Research Interests

- Integral Differential Equations

- Boltzmann Transport Equation

- Algorithm Development

- Scattering Theory